DOTTORATO DI RICERCA IN INGEGNERIA AEROSPAZIALE,
NAVALE E DELLA QUALITÀ
XXIV CICLO

UNIVERSITÀ DEGLI STUDI DI NAPOLI "FEDERICO II"

PhD dissertation

FLOW FIELD AND HEAT TRANSFER IN SWIRLING IMPINGING JETS

Andrea Ianiro

Contents

List of symbols

Symbol	Quantity
A_r	Circular area with radius r
Bi	Biot number $Bi=hs/k_f$
C_r	Recovery coefficient
C_1, C_2	First and the second universal radiation constants
c_p	Fluid specific heat
D^*	Sensitivity figure of merit of the infrared detector detectivity
D	Nozzle diameter
d	Vane pack hub diameter
E^b	Hemispherical emissive power
$f/\#$	Numerical aperture of the camera
$f(X,Y,Z)$	Object function of optical tomography
$G1$, $G2$	Grey intensities of the interrogation volumes corresponding to the first and the second image
H	Non-dimensional nozzle to plate distance $H=y_0/D$
h	Convective heat transfer coefficient
I^b	Energy flux per wavelength emitted by a black body in the hemisphere outside its surface.
I^b_{amb}	Black body radiation intensity corresponding to the (effective) temperature of the object surroundings T_{amb},
I^b_{atm}	Radiation intensity corresponding to a black body at the temperature of the atmosphere $T_{atm.}$.
I^b_{obj}	Radiation intensity corresponding to a black body at the object temperature
I'	Total radiation detected by the camera
I	Energy flux per wavelength emitted by a real body in the

	hemisphere outside its surface
$\underline{\underline{K}}$	Foil thermal conductivity tensor
k	Fluid thermal conductivity
k_f	Foil thermal conductivity
M_∞	Free stream Mach number
$\dot{m}$	Mass flow rate
N_{vox}	Number of voxels
Nu	Nusselt number $Nu=hD/k$
$\overline{Nu}$	Average Nu over a target area
Pr	Prandtl number $Pr=(c_p\mu)/k$
$p(x_i,y_i)$	i-th projection on the image plane
Q	Second invariant of $\underline{\nabla V}$

$$Q = \frac{1}{2}\left[\left(\frac{\partial U}{\partial X}\right)^2 + \left(\frac{\partial V}{\partial Y}\right)^2 + \left(\frac{\partial W}{\partial Z}\right)^2\right] - \frac{\partial U}{\partial Y}\frac{\partial V}{\partial X} - \frac{\partial U}{\partial Z}\frac{\partial W}{\partial X} - \frac{\partial V}{\partial Z}\frac{\partial W}{\partial Y}$$

q_c''	Convective heat flux
q_j''	Joule heat flux
q_k''	Tangential conduction heat flux
q_n''	Natural convection heat flux
q_r''	Radiation heat flux
R, B, F	Camera calibration constants
Re	Reynolds number: $Re = 4\dot{m}/(\pi\mu D)$
r	Nondimensional radial coordinate on the target plate
S	Swirl number: axial flux of swirl momentum divided by axial flux of axial momentum, times the equivalent nozzle radius.
St	Strouhal number $St=fD/V_j$
s	Foil thickness
T	Temperature
T_{amb},	Temperature of the object surroundings
$T_{atm.}$.	Temperature of the atmosphere
T_{aw}	Adiabatic wall temperature
T_{obj}	Object temperature
T_w	Wall temperature
T_∞	Free stream temperature

TKE	Turbulent kinetic energy $U'^2+ V'^2+ W'^2$
t	Normalized time (normalized with respect to D/V_j)
U	Non-dimensional velocity in the X direction: $U=u/V_j$
U'	Mean non-dimensional Reynolds stress along X
u	Velocity in the X direction
$\underline{V}$	Non-dimensional velocity vector
V	Non-dimensional velocity in the Y direction: $V=v/V_j$
V'	Mean non-dimensional Reynolds stress along Y
v	Velocity in the Y direction
V_j	Average jet velocity at the nozzle exit
V_{plate}	Velocity on the plate $V_{plate}=(U^2+W^2)^{0.5}$
W	Non-dimensional velocity in the Z direction: $W=w/V_j$
W'	Mean non-dimensional Reynolds stress along Z
w	Velocity in the Z direction
X	Non-dimensional abscissa in the foil plane $X=x/D$
x	Abscissa in the foil plane
Y	Non-dimensional coordinate normal to the plate $Y=y/D$
y	Coordinate normal to the plate
y_0	Coordinate of the impinged plane
Z	Non-dimensional ordinate in the foil plane $Z=z/D$
z	Ordinate in the foil plane
α_ρ	Absorptivity coefficient
β	Stefan–Boltzmann constant
γ	Iso-entropic exponent
δ	Boundary layer thickness
δ_T	Thermal boundary layer thickness
ε	Wall emissivity coefficient
η	Weighting function of the PIV cross-correlation
θ	Swirling angle
Λ	Linear dimension of the PIV interrogation volume
λ	Radiation wavelength
λ^*	Wavelength at which the black body emits its maximum spectral emissive power
μ	Air viscosity
μ_{G1}, μ_{G2}	Mean intensities of the interrogation volumes extracted from

	the first and the second image respectively
ρ_ρ	Reflectivity coefficient
σ_{Nu}	Standard deviation percentage of *Nu* over a target area
τ_ρ	Transmissivity coefficient
χ	Relaxation parameter of the MART algorithm
$\Psi_{i,j}$	Weighting element that determines the contribution of the j^{-th} voxel to the intensity recorded on the i^{-th} pixel
$\underline{\omega}$	Vorticity vector $\frac{1}{2}\underline{\nabla} \times \underline{V}$

Introduction

The high heat transfer rate obtainable with impinging jets is widely recognized and explained in scientific literature and the use of jets is very popular in many industrial applications like paper drying, glass tempering and turbine blades cooling. A huge quantity of data is available for single, rows and arrays of jets with also correlations for heat and mass transfer.

A major disadvantage of impinging isothermal and flame jets, however, is that the local heat flux can be highly non-uniform (Viskanta, 1993). For some applications, like electronic cooling or chemical vapour deposition, high values of heat and mass transfer with radial uniformity are requested. The swirling impinging jets, characterized by tangential velocity components that cause a spiral-shaped motion and the broadening of the jet, could be a possible solution to achieve both high heat transfer and radial uniformity.

The purpose of this work is to study the flow field and the heat transfer in swirling impinging jets. For the present study the swirling jets are obtained with helical inserts based on the concept of the cross swirling strips inside the nozzle and two experimental techniques are used: Tomographic Particle Image Velocimetry (Elsinga et al., 2006) for the three-dimensional three-components flow field measurements and IR thermography along with the "heated thin foil" heat transfer sensor (Carlomagno and Cardone, 2010) for the heat transfer measurements.

In chapter one the literature about free and impinging jets is reviewed in attempt to explain how the flow field influences the heat transfer distribution on the wall and to describe the state of the art in the field of swirling impinging jets and swirl flows. This literature review motivates the study of swirling impinging jets in order to understand both the fluid mechanics characteristics and the heat transfer performances. So far, has not yet been formulated a comprehensive framework where all the

results about vortex dynamics in swirl flows can be satisfactorily explained, and the modelling of rotating and swirling flows is still considered a perpetual challenge (Jakirlic et al. 2002). Most of the quantitative experimental studies on swirling flows have been limited to examining flow details using single-point measurement techniques, such as Laser Doppler Velocimetry (LDV), or planar techniques, such as PIV in particular. The inability to make instantaneous volumetric measurements often leads to ambiguities in the interpretation of the data, which necessitates various assumptions to link these reduced dimensional representations to the three-dimensional instantaneous structure of the flow. At the same time, while numerical simulation such as Direct Numerical Simulation (DNS) and Large Eddy Simulation (LES) in particular, has been instrumental in elucidating the three-dimensional dynamical features of swirling flows (see e.g. García-Villalba et al. 2006, Ranga Dinesh and Kirkpatrick 2009), they have to face with the difficulty of obtain reliable velocity profiles at the nozzle exit as boundary conditions (Ortega-Casanova et al. 2010). On the heat transfer side, almost all data related to swirling impinging jets reported in literature are presented as radial distribution even though, to assess the behavior of the flow field on the wall, two dimensional measurements are required. Furthermore, is not available in literature a quantitative analysis for the concept of heat transfer uniformity.

In chapter two, the basic working principles and the state of art of research about Tomographic PIV are described in order to understand the main parameters involved in the design of the experiments for the flow field measurements.

In chapter three, the basic working principles and the state of art of research on IR thermography for convective heat transfer measurements are described in order to understand the main parameters involved in the design of the experiments for the heat transfer measurements.

In chapter four, the flow field measurements are presented. A first study is performed by means of time resolved tomographic PIV on the three dimensional flow field of free swirling jets (at Reynolds number equal to 1,000) in order to analyze the main features of this complex flow. The development of the jets, the effect of swirl and the growth and interactions of coherent structures is discussed describing flow topology in swirling jets. Swirling impinging jets (at Reynolds number equal to 10,000) are then studied at low nozzle to plate distance analyzing both instantaneous measurements and flow statistics. This study allows to understand how the impinged plate influences the development of the

jets and the lifetime of its coherent structures; a special attention is put on the development of the jet in the “wall jet” region.

In chapter six, are presented experimental two-dimensional measurements of convective heat transfer between a flat plate and a swirling air jet impinging on it. This work is performed at a fixed Reynolds number (*Re* = 28,000) for different nozzle-to-plate distances and for different Swirl numbers. The heat transfer performances of swirling jets are also compared with those of a circular jet in order to account for both effects of the swirl and of the cross strips in the nozzle. Data are reported as Nusselt number surface maps, surface averaged Nusselt number and surface standard deviation percentage of the Nusselt number, in the attempt to quantify heat transfer rate and uniformity. In particular, this work represents the first effort to quantify non-uniformity in convective heat transfer coefficients in case of swirling, multichannel and circular jets. Moreover, the author proposes the use of the standard deviation percentage of the Nusselt number as a quantitative estimator for the heat transfer uniformity.

Chapter 1: Literature review

The high heat transfer rate obtainable with impinging jets is widely recognized and explained in scientific literature (e.g. Martin, 1977 and Jambunathan et al. 1992). A huge quantity of data is available for single, rows and arrays of jets also with correlations for heat and mass transfer (e.g. Viskanta,1993 and Meola, 2009).

Thus, jet impingement heat transfer is widely recognized as a high-performance technique for heating, cooling, or drying a surface. Direct impingement of turbulent jets onto a surface is often employed to achieve rapid heating or cooling in the glass industry (Lebedev and Sokolov, 1976) and in the reheating and heat treatment of metals (Klammer and Schupe, 1983). The impingement of flame jets on a load surface in a furnace can significantly increase heat transfer, reduce fuel consumption, and increase productivity (Viskanta, 1991).

In order to achieve a suitable plant design, from both an economic and a technical viewpoint, knowledge of the dependence of the heat and mass transfer rates on the external variables is required, thus interest in the topic from the standpoint of both empirical and theoretical applications continues unabated in recent years.

The mass flow rate, the diameter of the nozzles, their spacing and their distance from the product surface are the main variables, that can be chosen to solve a given heat or mass transfer problem. Probably, the impingement of unconfined axis-symmetric (circular) and slot (two-dimensional) jets on a flat surface is the topic most studied in the impingement heat transfer literature. However, a wide variety of other unconfined and confined configurations (single circular and slot, rows and arrays, obliquely inclined, and others) are studied. Owing to the fact that numerous studies have been conducted, the literature sources for the various configurations studied can be identified by reference to published reviews. For example, Jambunathan et al. (1992) review data

of impinging turbulent jets with nozzle exit Reynolds numbers in the range of 5,000–124,000: the geometry considered is that of a single circular jet impinging orthogonally onto a plane surface for nozzle-to-plate distances from 1.2 to 16 nozzle diameters and over a flow region up to six nozzle diameters from the stagnation point. Martin (1977) emphasizes the literature concerned with heat and mass transfer related to industrial heating and drying processes for which the nozzle diameters are large and the Reynolds numbers are well into the turbulent regime. Also Viskanta (1993) reviews heat transfer characteristics of single and multiple jets impinging on surfaces: the emphasis is on applications in the materials processing field of both isothermal and flame jets; areas needing research attention are also identified. On the other hand, Downs and James (1987) present a literature survey on jet impingement heat transfer and they focus on gas turbine component cooling. In such applications the nozzle diameters are quite small, but the Reynolds number can be quite large due to the high velocity of the jet. In the other limiting case of very small diameter, jet impingement heat transfer is relevant to local cooling of hot spots on circuit boards in electronic packaging (Fabbri et al. 2005). Given the physical sizes of the heat-dissipating components and the device density of modern electronic circuitry, the jet nozzles may be quite small (< 1 *mm*) and are therefore referred to as micro-jets.

While a lot of works study heat transfer performances of impinging jets, many other studies both experimental (Kataoka et al. 1987, O'Donovan and Murray 2007 a and b) and numerical (Hadziabdic and Hanjalic 2008) try to understand the features of the flow field of impinging jets and to explain the heat transfer performances from the physical standpoint. A recent review from Zuckerman and Lior (2006) is also focused on understanding the flow field of impinging jets with the goal of identifying preferred methods of predicting jet performance.

In this chapter the main literature results about the flow field in impinging jets and the relation between the flow field and the convective heat transfer distribution are described. On the basis of the analysis of the flow field and heat transfer performances of circular jet, swirling jets developed for increasing heat transfer uniformity are reviewed. The main features related to swirl flows are also described.

1.1 Free and impinging single jet flow field

The flow field of free jets is presented in textbooks (e.g., Rajaratnam, 1976), and also reviews of impinging jets are available (e.g., Gauntner et

al, 1970) so, here, only the basic concepts are introduced; in particular the flow of a submerged impinging jet passes through several distinct regions, as shown in Fig. 1.1.

The jet emerges from a nozzle or an opening with a velocity and temperature profile and with turbulence characteristics dependent on the upstream flow and on nozzle shape (Schetz and Fuhs, 1999). For a pipe-shaped nozzle the flow develops into the parabolic velocity profile common to pipe flow plus a moderate amount of turbulence developed upstream. In contrast, a flow delivered by the application of differential pressure across a thin, flat orifice will create an initial flow with a fairly flat velocity profile, less turbulence, and a downstream flow contraction (vena contracta). Typical jet nozzle designs use either a round jet with an axis-symmetric flow profile or a slot jet, a long, thin jet with a two-dimensional flow profile.

After it exits the nozzle, the emerging jet may pass through a region where it is sufficiently far from the impingement surface to behave as a free submerged jet. In the free jet region (Fig. 1.2), the velocity gradients

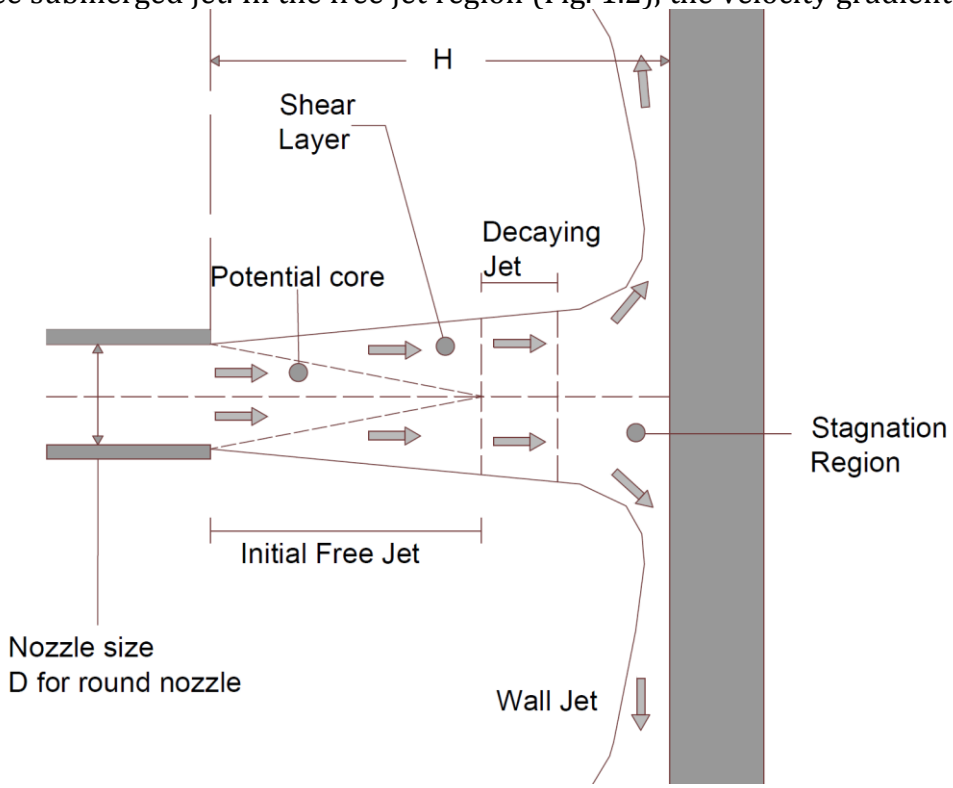

Fig. 1.1 The flow regions of an impinging jet

lead to a shear-driven interaction of the exiting jet with the ambient that produces entrainment of mass, momentum, and energy. The net effects include the development of a non-uniform radial velocity profile within the jet, the expansion of the jet, an increase of total mass flow rate, and the modification of the jet temperature. In the process, the jet loses energy and the velocity profile is widened in spatial extent and decreased in magnitude along the sides of the jet. The flow interior to the progressively widening shear layer remains unaffected by this momentum transfer and forms a core region (called potential core) with a higher total pressure, though it may experience a drop in velocity and a pressure decay resulting from velocity gradients present at the nozzle exit. Despite of that, it has to be remarked that a free jet region may not exist if the nozzle lies within a distance of two diameters ($2D$) from the target. In such cases, the nozzle is close enough to the elevated static pressure in the stagnation region for this pressure to influence the flow immediately at the nozzle exit. According to Viskanta (1993),at small separation distances, the velocity profile of the jet does not have sufficient room to develop and the arrival velocity is essentially uniform. Thus, impingement occurs within the potential core of the jet and the pressure distribution well agrees with the inviscid solution.

If the shear layer expands toward the centre of the jet before reaching the target, a region of core decay forms. For distinct identification purposes, the end of the core region may be defined as the axial position where the centreline flow dynamic pressure (proportional to speed squared) reaches 95% of its original value.

The length of the potential core is dependent on the turbulence intensity in the nozzle exit and the initial velocity profile. Livingood and Hrycak (1973) show that the potential core zone extends 6-7 diameters from the nozzle exit for axis-symmetric jets and 4.7-7.7 slot widths for slot jets. This decaying jet begins four to eight nozzle diameters or slot-widths downstream of the nozzle exit. In the decaying jet, the axial velocity component decreases and according to Reichardt (1943), a Gaussian velocity distribution best fit experimental measurements in this zone. Other investigations show that in the fully developed zone the jet broadens linearly and that the decay of the axial velocity is also linear. Martin (1977) provides a collection of equations for predicting the velocity in the free jet and decaying jet region.

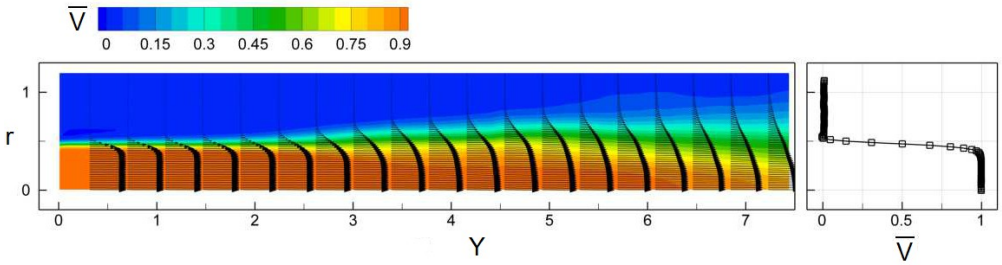

Fig. 1.2 The flow field of a free submerged jet, *Re* = 5000(from Violato and Scarano 2011)

As the flow approaches the wall, it loses axial velocity and turns in a region called stagnation region. The flow builds up a higher static pressure on and above the wall, transmitting the effect of the wall upstream. The non-uniform turning flow experiences high normal and shear stresses in the deceleration region, which greatly influence local transport properties. According to Schrader (1961) the stagnation region typically extends 1.2 nozzle diameters above the wall for round jets, and the thickness of the boundary layer in this zone is approximately constant (and reaches about one hundredth of the nozzle diameter).

After turning, the flow enters a wall jet region where the flow moves laterally outward parallel to the wall. Due to the finite breadth of the jet and the exchange of momentum with its quiescent surroundings, the accelerated stagnation flow finally must transform in an accelerated wall jet flow (Glauert, 1956). So the wall parallel velocity component, initially increasing from zero must reach a maximum at a given distance from the stagnation point. Due to the presence of a shear layer influenced by both the velocity gradient with respect to the stationary fluid at the wall (no-slip condition) and the velocity gradient with respect to the fluid outside the wall jet, the boundary layer thickness for the wall jet is defined as the height at which wall-parallel flow speed in the wall jet is maximum at a given radial position. The boundary layer within the wall jet begins in the stagnation region, where it has a typical thickness of no more than 1% of the jet diameter. As the wall jet progresses, it entrains flow and grows in thickness, and its average flow speed decreases as the location of highest flow speed shifts progressively farther from the wall; thus the maximum speed in the wall jet finally tends to zero in the fully developed wall jet proportionally with the distance from the centre of impingement r^{-1} for the axis-symmetric jet (proportionally with the distance from the line of impingement $X^{-0.5}$ in case of plane jet) according to Glauert (for a round jet, mass conservation results in additional deceleration as the jet

spreads radially outwards). Whereas the stabilizing effect of the acceleration keeps the boundary layer laminar in the stagnation zone, transition to turbulence generally occurs in the decelerating flow region immediately after the coordinate at which the flow reaches the maximum velocity.

An impinging jet is considered to be laminar up to a single jet Reynolds number of approximately 2500 (Polat et al. 1989). This value is commonly used, although there is no direct evidence confirming a transition Reynolds number for impinging jets; in fact, whether a laminar free jet is still laminar before impingement depends on many factors such as the Reynolds number *Re*, the original velocity profile, the separation distance, and whether the jet is confined or not. All these factors affect the mixing at the outer jet boundaries that transforms a laminar jet into a turbulent jet. More specifically, there are four characteristic regions for circular free jets according to the value of the Reynolds number:

1. The dissipated laminar jet, $Re < 300$
2. A fully laminar jet, $300 < Re < 1000$
3. A transitional or semi-turbulent jet, $1000 < Re < 3000$
4. A fully turbulent jet, $Re > 3000$

The turbulent kinetic energy, gives a measure of the intensity of the turbulent flow field. In addition to generation in the impinging jet flow field itself, turbulence in the flow field may also be generated upstream of the nozzle exit and convected into the flow. This often takes place due to the coolant flow distribution configuration, but can also be forced in order to increase the heat transfer coefficients, by inserting various screens, tabs, or other obstructions in the jet supply pipe upstream of the nozzle or at the nozzle exit (Violato et al. 2011). The downstream flow and heat transfer characteristics are sensitive to both the steady time-averaged nozzle velocity profile and fluctuations in the velocity over time. Knowledge of these turbulent fluctuations and the ability to model them, including associated length scales, are vital for understanding and comparing the behaviour and performance of impinging jets. In the initial jet region the primary source of turbulence is the shear flow on the edges of the jet. This shear layer may start as thin as a knife-edge on a sharp nozzle, but naturally grows in area along the axis of the jet. The shear layer generates flow instability, similar to the Kelvin–Helmholtz instability.

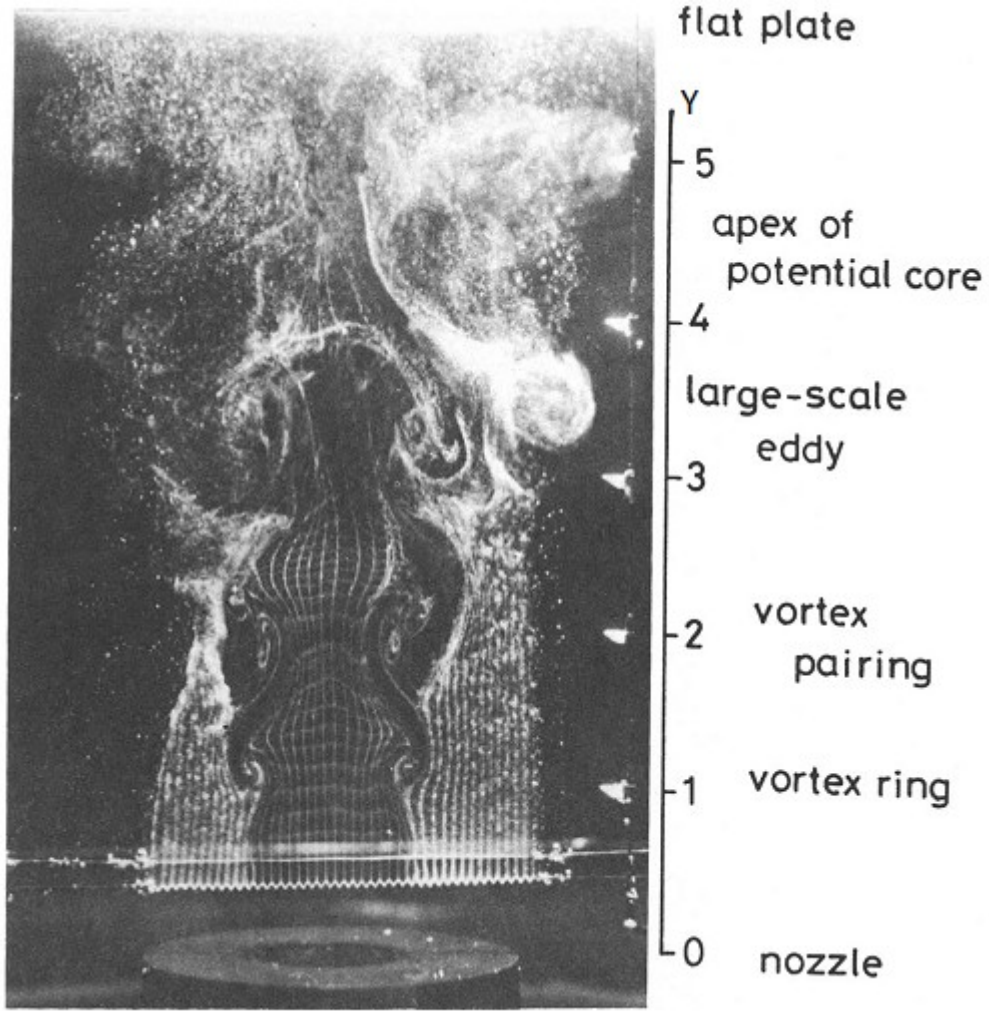

Fig. 1.3 Cross-sectional view of the free jet flow patterns visualized by the hydrogen bubble method, H = 6, Re = 4000 (from Kataoka et al., 1987)

Fig. 1.3 presents in the pattern of motion at the edges of the unstable free jet experimentally observed by Kataoka et al. (1987). If Reynolds number is high enough (e.g. $Re > 1000$), the destabilizing effects of shear forces may overcome the stabilizing effect of fluid viscosity/momentum diffusion. The position of the shear layer and its velocity profile may develop oscillations in space, seemingly wandering from side to side over time. Downstream the magnitude and the spatial extent of the oscillations grow to form large-scale vortices along the sides of the jet. Popiel and Trass (1991) suggest that a laminar boundary layer formed in elliptical or bell-shaped convergent nozzles is essential to the formation of a well-defined vortex structure. They give results for a jet issuing from

a nozzle that was designed to disrupt this laminar layer; the visualization shows a much less distinct vortex structure. This suggestion is supported by Lepicovsky (1989), who study the effect of nozzle exit boundary-layer thickness on the length of the potential core. This study suggests that a thin laminar boundary layer at the nozzle exit results in higher rates of jet mixing than a thick boundary layer. However, turbulence measurements made by Yokobori et al. (1979) at the nozzle exit suggest that the vortex structure can still be obtained when the boundary layer at the nozzle exit is turbulent.

The largest eddies have a length scale of the same order of magnitude as the jet diameter and persist until they either independently break up into smaller eddies or meet and interact with other downstream flow features (vortex pairing). The pressure field of the stagnation region further stretches and distorts the eddies, displacing them laterally until they arrive at the wall (see Fig. 1.4 from Violato et al. 2011).

Clearly, as shown already in the seventies by Hoogendorn (1977), the development of turbulence in the free jet is critical in influencing the arrival conditions of the flow on the plate. In the decaying jet region the shear layer extends throughout the centre of the jet and this shearing promotes flow turbulence, but on smaller scales. The flow in the decaying jet may form small eddies and turbulent pockets within the centre of the jet, eventually developing into a unstructured turbulent flow field with little or no coherent structures in the entire jet core. In the deceleration region, additional mechanisms take part in influencing flow field turbulence. The pressure gradients within the flow field cause the flow to turn, influencing the shear layer and turning and stretching large-scale structures thus increasing the turbulence; also the deceleration of the flow creates normal strains and stresses, which

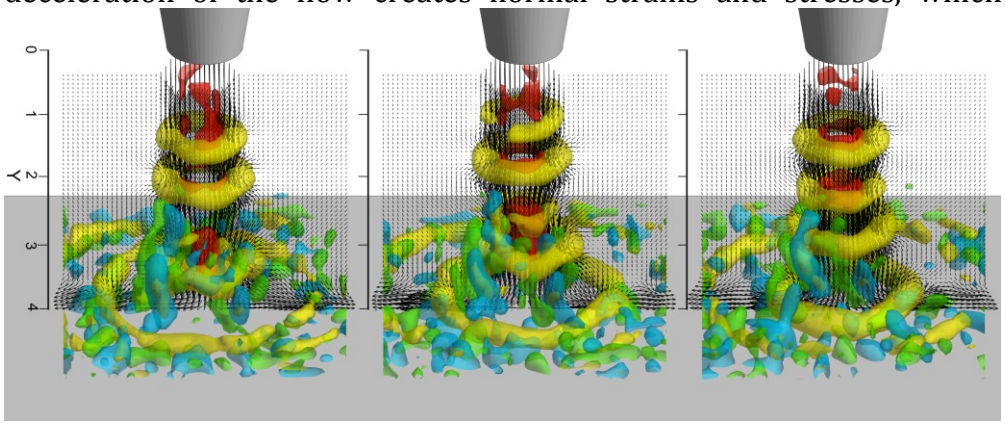

Fig. 1.4 Visualization of vortex dynamics in impinging jets with tomographic PIV (from Violato et al. 2011)

promote turbulence. The effects of the vortices in the deflection zone close to the stagnation point is detected by Kataoka et al. (1987) using a hot-wire anemometer. They identify a "surface-renewal" parameter that is proportional to the frequency and magnitude of these vortices, with a correlation obtained for z/D between 2 and 10. Then for transitional and turbulent jets, the flow approaching the wall has already a substantial turbulence level. This turbulent flow field may contain large fluctuations in the velocity component normal to the wall, a phenomenon distinctly different than those of wall-parallel shear flows (Cooper et al. 1993).

Large-scale turbulent flow structures in the free jet have a great effect upon transfer in the stagnation and the wall jet region. The vortices formed in the free jet-shear layer, categorized as primary vortices, may penetrate into the boundary layer and exchange fluids of differing kinetic energy and temperature (or concentration). The primary vortex dynamically scrubs away the boundary layer, as it travels against and along the wall. The turbulent flow field along the wall may also cause formation of additional vortices categorized as secondary vortices. Turbulent fluctuations in lateral/radial velocity and associated pressure gradient fluctuations can produce local flow reversals along the wall, initiating separation and the formation of the secondary vortices, as shown in Fig. 1.5 (Hadziabdic and Hanjalic, 2008).

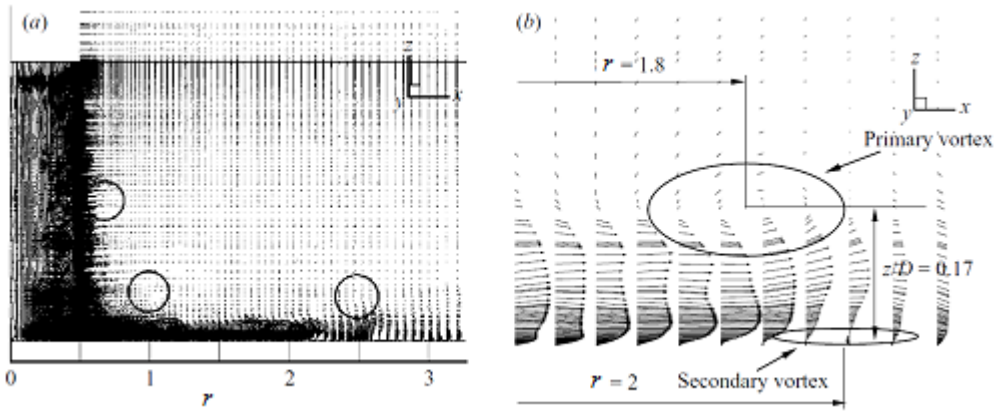

Fig. 1.5 Instantaneous velocity-vector field: (a) a full view with three vortical cores(encircled); (b) an enlargement in the wall-jet region around r/D=2 (from Hadziabdic and Hanjalic 2008)

1.2 Convective heat transfer in single impinging jets

Heat transfer between a solid wall and a fluid, e.g. a hot plate with a cold air jet, impinging on it is one of the main topics of this thesis. In a flowing fluid, energy is transferred not only through heat conduction but also by the macroscopic movement of the fluid. When we imagine an area located at a given position within the fluid, heat flows through this area by conduction due to the temperature gradient and, in addition, energy is transferred as enthalpy and kinetic energy of the fluid crossing the area. This is known as convective heat transfer that can be described as the superposition of thermal conduction and energy transfer by the flowing fluid (Eckert and Drake, 1972).

The fluid layer close to the wall has the greatest effect on the amount of heat transferred. It is known as the boundary layer and boundary layer theory founded by Prandtl (1904) is the area of fluid dynamics that is most important for heat and mass transfer. In the boundary layer the velocity component parallel to the wall changes, over a small distance, from almost the maximum value occurring in the core fluid to zero at the wall (Fig. 1.6). At the same time the temperature in the boundary layer also changes from T_∞ at some distance from the wall to that at the wall T_w.

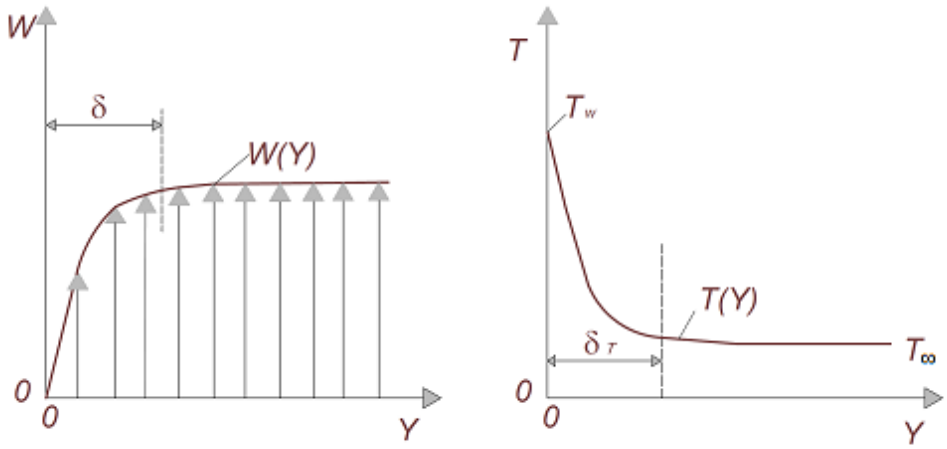

Fig. 1.6 Velocity *W* (left) and temperature *T* (right) profiles in a fluid as a function of distance from the wall *Y*. δ and δ_T represent the velocity and temperature boundary layer thicknesses

If the immediate neighbourhood of the wall ($Y \rightarrow 0$) is considered, here the fluid adheres to the wall, except in the case of very dilute gases. Fluid velocity on the wall is zero, and energy can only be transported by heat conduction, so the Fourier's law is valid and the convective heat flux can be defined as:

$$q_c''=-k(dT/dY)_{Y=0} \quad 1.1$$

where k, or to be more precise $k(T_w)$, is the thermal conductivity of the fluid at the wall temperature.

It is important, at this moment to define the adiabatic wall temperature T_{aw}; the adiabatic wall temperature is a reference temperature of the fluid at which the heat transfer between the fluid and the wall is zero. The reference temperature depends on the conditions of the fluid stream. E.g., for external low Mach number flows, the reference temperature practically coincides with that of the undisturbed stream. Instead, for compressible flows (Shapiro 1954) the equation is:

$$T_{aw} = T_\infty \left(1 + C_r \frac{\gamma - 1}{2} M_\infty^2 \right) \quad 1.2$$

where γ is the iso-entropic exponent, M_∞ is the Mach number in the external flow and C_r is the recovery coefficient. The recovery coefficient C_r is not a constant but depends, in particular, on the character of the flow on the surface, the flow regime, and the thermal properties of the medium. For some simple cases, its value can be estimated as follows: at the front stagnation point of bodies in the flow, C_r = 1; in a laminar boundary layer on a plane plate, $C_r \cong \sqrt{\mathrm{Pr}}$ for Prandtl numbers 0.5 < Pr <10; in a turbulent boundary layer on a plate, $C_r \cong \sqrt[3]{\mathrm{Pr}}$ for Prandtl numbers close to 1.

Adiabatic wall temperature T_{aw} is the temperature acquired by a wall in liquid or gas flow if the condition of thermal insulation is observed on it: $(\partial T/\partial Y)_{Y=0}$ = 0 or q_c''= 0. A distinction between the adiabatic wall temperature and a characteristic flow temperature may depend on the dissipative heat release in the boundary layer, on the existence in the flow of a different nature of internal heat sources and on the thermal effect of other bodies (walls). In this case, if there is heat transfer between the wall and the flow, i.e., at $q_c'' \neq 0$, the temperature field in the fluid can be represented as a superposition of the temperature field at

q_c'' = 0 on the natural field, which would be produced by the wall in the absence of disturbing factors, e.g. internal heat release or the effect of other walls. This superposition allows to represent the law of heat transfer between the flow and the wall as:

$$q_c'' = h\,(T_w - T_{aw}) \qquad 1.3$$

It means that if the fluid is hotter (colder) than the wall, i.e. $T_{aw} > T_w$ ($T_{aw} < T_w$), the fluid will be cooled (heated) as heat flows into the wall (into the fluid). with a new quantity, the local convective heat transfer coefficient, defined by

$$h = q_c''/(T_w - T_{aw}) \qquad 1.4$$

This definition replaces the unknown heat flux q_c'', with the heat transfer coefficient, h, which is also unknown. This is the reason why many researchers see the introduction of h as unnecessary and superfluous. Nevertheless the use of heat transfer coefficients seems to be reasonable, because when h is known both the basic questions in convective heat transfer can be easily answered; in fact, it is possible to know what is the heat flux q_c'' for a given temperature difference $T_w - T_{aw}$, and what difference in temperature $T_w - T_{aw}$ causes a given heat flux q_c'' between the wall and the fluid. It is still possible anyway to investigate the physical meaning of h: from Eq. 1.1 and Eq. 1.4, it follows for the heat transfer coefficient

$$h = -k(dT/dY)_W / (T_w - T_{aw}) \qquad 1.5$$

From this, it is clear that h is determined by the gradient of the temperature profile at the wall and the difference between the wall and fluid temperatures. Therefore, to calculate the heat transfer coefficient, knowledge of the temperature field in the fluid is required. This is, in turn, influenced by the velocity field within the fluid. So, in addition to the energy balances from thermodynamics, the equations of fluid motion from fluid mechanics provide the fundamental relationships in the theory of convective heat transfer.

A simple graphical illustration of h follows from Eq. 1.5. As shown in Fig. 1.7 the ratio k/h is the distance from the wall at which the tangent to the temperature profile crosses the $T = T_{aw}$ line. The length of k/h is of the magnitude of the (thermal) boundary layer thickness which is normally a bit larger than k/h. A thin boundary layer indicates good heat transfer while a thick layer leads to small values of h.

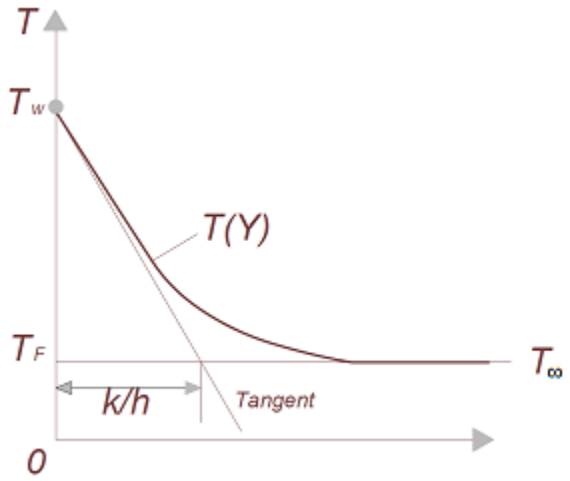

Fig. 1.7 Fluid temperature as a function of the distance from the wall and illustration of the ratio *k/h*

In this work all the parameters are always presented as non-dimensional and the convective heat transfer coefficient is evaluated in non-dimensional form with the Nusselt number,

$$Nu = h\,D/k \qquad 1.6$$

where the nozzle diameter D is used as reference length. The selection of Nusselt number to measure the heat transfer describes the physics in terms of fluid properties, making it independent on the target characteristics.

The non-dimensional Sherwood number defines the rate of mass transfer in a similar fashion as Nusselt number and, in general, with sufficiently low mass concentration of the species of interest, the spatial distribution of concentration will form patterns similar to those of the temperature pattern. In general, based on the Chilton-Colburn analogy (Chilton and Colburn, 1934) it is possible to relate heat and mass transfer rates and compare those literature results.

The non-dimensional parameters selected to describe the single circular impinging jet heat transfer problem include the fluid properties such as Prandtl number Pr (the ratio of fluid thermal diffusivity to viscosity, fairly constant), plus the following:

r : non-dimensional radial position from the centre of the jet;

Y : non-dimensional vertical position measured from the wall,

H: non-dimensional nozzle to plate distance;

TKE : non-dimensional turbulence kinetic energy;

Re : Reynolds number;

M_∞ : Mach number (the flow speed divided by speed of sound in the fluid), based on nozzle exit average velocity (of smaller importance at low speeds, i.e. M<0.3);

The fluid properties are conventionally evaluated using the flow at the nozzle exit as a reference location. Characteristics at the position provide the average flow speed, fluid temperature, viscosity, and length scale *D*.

An analytical solution for heat transfer at a stagnation point in a laminar flow (Sibulkin, 1952) shows that $Nu \propto V_j^{1/2}$ suggesting that the Nusselt number should remain roughly constant in the core region and reduce downstream of the core.

Indeed the turbulence intensity of the jet is a very influential factor for impingement heat transfer performances. The axial variations of velocity and turbulence for slot jets issuing into an unconfined environment are investigated by Gardon and Akfirat (1965). Their results show that the turbulence intensity in a free jet could reach 30 percent of nozzle exit velocity at approximately eight nozzle diameters downstream of the nozzle. The axial distance from the nozzle at which the maximum turbulence intensity occurs appears to coincide with that of the maximum stagnation point heat transfer. Measurements using circular nozzles also give similar results; e.g., Schlunder and Gnielinski (1967) find both the maximum turbulence and the maximum stagnation point heat transfer occurring at H = 7.5. Gardon and Akfirat suggest that the increasing level of turbulence causes the heat transfer rate at the stagnation point to increase even beyond the end of the potential core where the jet centreline velocity is falling. The increase in heat transfer rate ceases when the increase in turbulence does not compensate for the fall in the jet velocity.

The radial variation of heat transfer coefficients measured by Gardon and Cobonpue (1962) are given in Fig. 1.8. These curves show that local maxima in the heat transfer rate at the lower values of nozzle-to-plate spacing (H < 6) are out from the centre of the plate. For impinging circular jets at small Y the heat transfer coefficient is seen to increase between the stagnation point and approximately r = 0.5. A second maximum is produced by circular jets at approximately r = 2.

The peak at r = 0.5 has been explained by the change in radial velocity, with displacement from the stagnation point. As said in the previous paragraph, the radial velocity accelerates rapidly in the deflection region,

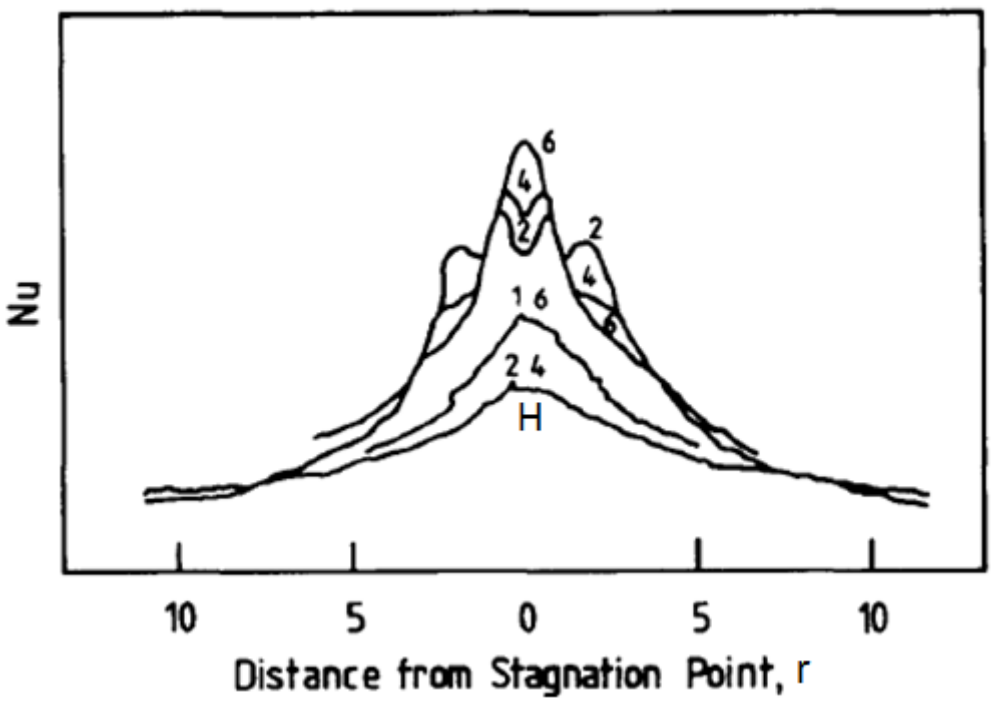

Fig. 1.8 Radial variation of heat transfer coefficient between a plate and an impinging jet. (Data from Gardon and Cobonpue 1962)

but at greater radii the spreading of the jet causes the radial velocity to decrease. Gardon and Akfirat (1965) suggest that the increase in heat transfer coefficient within the range $1 < r < 2$ can be explained by a transition from laminar to turbulent boundary-layer flow but velocity measurements (Cooper et al. 1993) in the boundary layer of an impinging jet for $H = 2$ show the presence of turbulence at the stagnation point.. At greater radial distances from the stagnation point a fall in the heat transfer rate occurs because of the fall in flow velocity in the radial direction. This mechanism will not apply to impinging jets that are fully developed or to impinging jets at large nozzle-to-plate spacings, resulting in turbulent boundary-layer flow at the stagnation point.

By smoke-wire visualizations of a low nozzle-to plate distance impingement, Popiel and Trass (1991) show the shedding and pairing of the ring vortices and the process of interaction with the plate. When the vortex approaches the plate, it stretches and increases its diameter. Based on convective heat transfer measurements by infrared

thermography (IR), Meola et al. (1996) say that, for low nozzle-to-plate distances, vortex rings cause the unsteady separation of the flow and the reattachment at a downstream location depending on the strength of the vortex. The point of reattachment coincides with the second peak of heat transfer distribution. In a more recent work Narayanan et al. (2004) address the maximum Nu to high outer wall-jet region turbulence, rather than to high turbulence only in the near-wall portion of the wall jet. Their specific conclusion was that the outer region turbulence caused an unsteadiness in the thermal boundary layer outside of the stagnation region; moreover the work by Hadziabdic and Hanjalic (2008) shows as the local minimum in heat transfer before r= 2 is due to an unsteady flow separation.

Flow visualization photographs obtained by Yokobori et al. (1979) also show these toroidal vortices being convected to the impingement plate. These vortices undergo pairing, and for $Y > 4$ the large-scale vortex structure appears to break down into small-scale random turbulence that penetrates to the jet axis. Radial movement of the stagnation point of the order of one nozzle diameter was also reported. However, a potential core exists for $Y < 4$ where the vortices do not penetrate. The penetration of the vortices to the geometric stagnation point and the radial movement of the stagnation point help to break down any distinct flow regions. This may explain why the secondary maxima in the radial distribution of heat transfer coefficient become indistinct and the profiles begin to assume a bell shape for nozzle-to-plate spacings greater than $H = 4$.

1.3 Free and impinging swirling jets

A major disadvantage of impinging isothermal and flame jets, however, is that the local heat flux can be highly non-uniform (Viskanta, 1993). For some applications such as electronic cooling or chemical vapour deposition, both high values and high radial uniformity of heat and mass transfer are required and the swirling impinging jet could be a possible solution to achieve both high heat transfer and radial uniformity. Swirling flows are frequently found in nature as well as in a wide variety of industrial applications. In the atmosphere, numerous phenomena of meteorological relevance are associated to swirl flows, such as cyclones, lee vortices, mesocyclones, and tornadoes. In engineering applications, swirling jets are frequently used in combustors: in gas turbine combustors swirling jets generate a reverse flow regions near the jet nozzle with consequent flame stabilization; turbulent mixers,

agricultural spraying machines, whirlpools and cyclone separators also take advantage of the high spreading rate in swirling jets with consequent rapid mixing of the jet fluid with its surrounding. The flow around delta wings or at the tip of aircraft wings also produce vigorous vortices that result in a swirling flow field (Lowson, 1964).

As the flow visualizations by Huang and El Genk (1998) show, swirling impinging jets are characterized by tangential velocity components that cause a spiral-shaped motion and the broadening of both the impinged area and the wall jet area (Fig. 1.9); this aspect is also coupled, especially near the stagnation point, with an axial flux weakening. The flow field of the swirling impinging jet can be divided in 6 characteristic sections: free jet, impinged area, spiral flow mixing region, flow separation region and internal flow mixing region The swirl causes the flow to open radially; the spiral effect and the high air velocity on the outer surface of the free jet seem to generate more entrainment than that observed in conventional jets. In the central region, toroidal recirculation zones are generated in the case of high swirl as PIV (Particle Image Velocimetry) measurements by Alekseenko et al. (2007) show. The impinged area (stagnation region) is significantly larger in the swirling jet compared to the conventional jet, while the spiral flow mixing and the flow separation regions essentially coincide with respectively the wall jet and the flow separation regions in the circular impinging jet; the entrainment region is similar to that of the circular jet, but seems to produce a more marked effect.

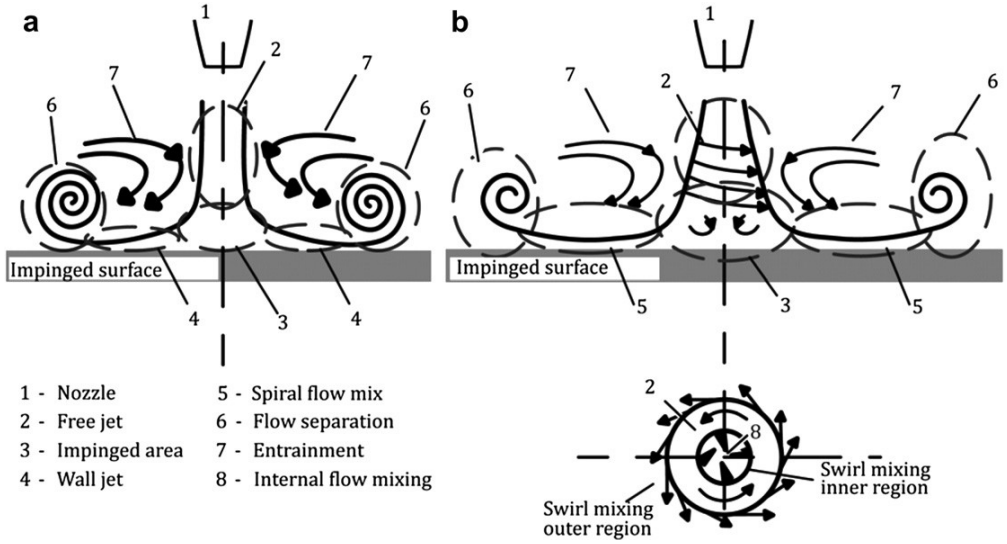

Fig. 1.9 Flow topological structures of: (a) circular impinging jet, (b)swirling impinging jet (from Ianiro and Cardone, 2011)

Generally, it is possible to obtain a swirling flow either by mixing two air flows or by using an insert inside the nozzle. The first study on a swirling impinging jet is due to Ward and Mahmood (1982). The swirling jet designed by Ward and Mahmood, based on the concept of mixing an axial air flow with a tangential one, is characterized by a radial distribution of the local convective heat transfer, which, compared to the circular jet, is slightly more uniform and with a significantly lower heat transfer rate. An improved swirling nozzle, based on a cylindrical plug with four narrow channels, is proposed by Huang and El Genk (1998). Such swirling nozzle is characterized by improved radial uniformity and increased rate of the surface average heat transfer. Also Lee et al. (2002) analyze the heat transfer distribution related to swirling impinging jets, based on the concept of an insert inside the jet nozzle; in this work it is assessed the heat transfer uniformity provided by the swirl and it is demonstrated the strong dependence of the heat transfer distribution on the degree of swirl. The degree of swirl is usually accounted for through the swirl number S, which is a dimensionless quantity representing the ratio between the axial flux of swirl momentum and the axial flux of axial momentum times equivalent nozzle radius; generally $S < 0.4$ corresponds to a low degree of swirl while $S > 0.6$ corresponds to a high degree of swirl. In literature (e.g., Chigier and Chervinsky 1967, Gupta et al. 1984, Billant et al. 1998) there are many commonly used definitions of the swirl number, that depends on the swirl generator used and on many simplifying assumptions. In a recent work Toh, et al. (2010) well analyze the effect of approximations in the various commonly used swirl number definitions. Lee et al. (2002) show that the highest heat transfer occurs for the lower swirl number studied (S equal to 0.2) and for the lower nozzle-to-plate distance(equal to 2 diameters). For small nozzle-to-plate distance, the average heat transfer values provided by the swirling jets are larger than those achieved with non-swirling flows (without the insert) for all swirl numbers. Instead, for large nozzle-to-plate distance (equal to 10 diameters) the effect of heat transfer enhancement has been rarely seen. Lee et al. (2002) find that a better uniform heating is reached at the highest swirl number studied that is $S = 0.77$, but this conclusion is not supported by a quantitative analysis. The study by Wen and Jang (2003) compares, at a fixed swirling angle, jet nozzles with longitudinal and cross swirling strips, showing that a jet nozzle with cross swirling strips achieves better heat transfer performances than standard jets. Yuan et al. (2006), using a longitudinal swirling strip nozzle, investigate the effect of swirl on the heat transfer from a flat surface impinged by a CO_2 jet. They do not mention the swirl

number used for the experiments (a swirl number equal to 0.2 can be estimated from their data) but come to the conclusion that the swirl improves significantly both heat transfer radial uniformity and rate. Also in this case, the effect on uniformity is not quantified; moreover, by analyzing their data, the heat transfer enhancement is not so evident. The experiments of Ichimiya and Tsukamoto (2006 and 2010) on the heat transfer for swirling impinging jets, performed at very short nozzle-to-plate distances (less than one diameter) both in turbulent (2006) and in laminar (2010) regimes, show that in both cases the local heat transfer is enhanced by the flow mixing; in particular, the maximum heat transfer rate is achieved at a given swirl number. Recently, Yang et al. (2010) analyze impinging circular jet flow field, wall pressure and heat transfer characteristics with and without induced swirling motion (at swirl number equal to 0.92). Their PIV and wall pressure data confirm the classical observations for the conventional circular impinging jet. In the presence of swirl, at short and intermediate nozzle-to-plate distances, the swirling jet causes less uniform distribution of wall pressure and heat transfer on the impingement plate than the conventional circular jet; conversely, for large nozzle-to-plate distances, a more uniform distribution of both wall pressure and heat transfer is provided by the swirling impinging jet.

As stated in before, swirling jets result from the application of azimuthal momentum to the axial flow. The azimuthal velocity component is imparted to the flow with a swirl generator. The swirl generator may be based on several principles: Harvey (1962) proposed swirl vanes, Chigier and Chervinsky (1967) adopted an axial- tangential fluid entry, Billant et al. (1998) put in rotation a long tube where a the flow is fully developed , Rose (1962) investigated a system where the flow passes through a rotating, perforated plate.

An extensive discussion of swirl flows is documented in the book by Gupta et al. (1984). Topical reviews are given by Lilley (1977) on swirl flows in combustion, by Lucca-Negro and O'Doherty (2001) on the vortex breakdown phenomenon and by Syred (2006) about the behaviour of the precessing vortex core (PVC). From the studies in literature it emerges that the swirling motion affects the large-scale flow organization and the mean flow field properties. In general, in the case of inert jets the degree of swirl imparted to the flow strongly influences the jet growth and entrainment rates as well as the decay process. The effect of a low degree of swirl is to increase the width of a free or confined jet flow: jet growth, entrainment, and decay are enhanced progressively as the degree of swirl is increased. In fact Park and Shin (1993) analyze

"shlieren" visualizations and perform quantitative measurements of the jet growth and entrainment rates associated to the swirl and confirmed a substantial increase of these properties. At high swirl, a pressure gradient develops strongly both in the radial and axial directions near the nozzle exit, resulting in axial recirculation zone. This phenomenon, first observed on delta wing vortices by Lambourne and Bryer (1961), is called vortex breakdown (see fig. Fig. 1.10) and is best described according to Harvey (1965) as giving the impression that an imaginary body of revolution has been placed on the axis of jet (the axis of the vortex responsible of the swirl), around which the fluid is obliged to flow.

In the case of reacting flows the degree of swirl governs the critical aspect of flame stability and affects flame size and shape as well as the resulting combustion rate. Tangirala et al. (1987) show that the effect of increasing the swirl is to improve the mixing and flame stability. Chen et al. (1990) investigate the use of swirl for controlling the length and the mixing in the flame. According to Huang and Yang (2005), increasing the degree of swirl, the turbulence intensity tends to increase as well as the flame speed; this allows to reduce the flame size without reducing the rate of heat released.

The unsteady flow organization of swirling jets is characterized by the presence of an axial shear layer and of a Rankine-like vortex (the central vortex core due to the swirl) and an azimuthal component of the shear. This deals with shear-induced instabilities of Kelvin-Helmholtz type similar to those encountered in non-swirling flows and with the centrifugal instability of the Rankine vortex when the circulation decreases outwards (Loiseleux et al. 1998). However, few early works

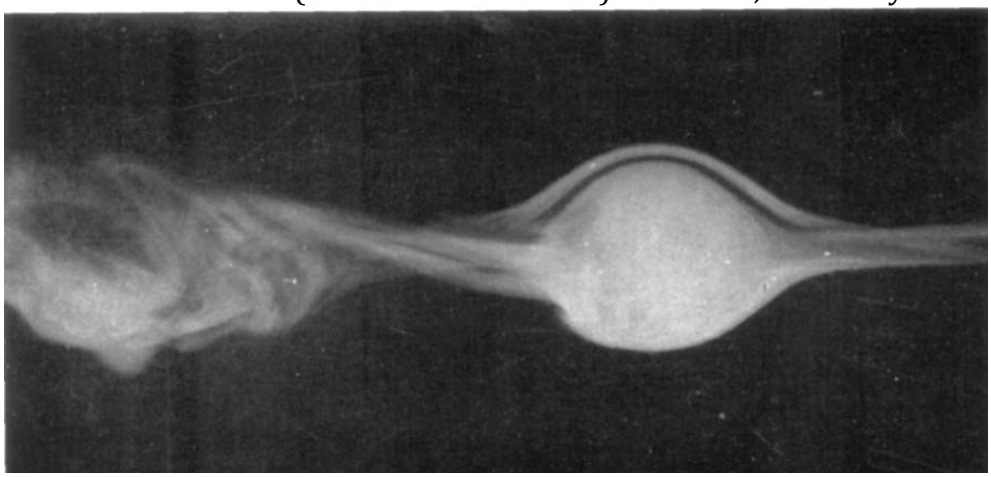

Fig. 1.10 A visualization of the vortex breakdown (from Harvey, 1965)

identify pronounced flow instabilities in swirled jets. Chanaud (1965) first report about three dimensional time-dependent coherent structures. In a subsequent work Syred & Beér (1974) hypothesize that the flow field may not be axis-symmetric and that after the vortex breakdown phenomenon, the axial flow region becomes unstable and begins precessing around the axis of symmetry. Actually this hypothesis is confirmed by the laser-doppler anemometry analysis conducted by Yazdabadi et al. (1994) on a high swirl cyclone dust separator: they conclude that the reverse flow region displaces the central vortex core to create the precessing vortex core (PVC). The reverse flow zone seems to provide feedback for the PVC that precess around the jet and, at the same time, accelerates the flow. The laser doppler and particle image velocimetry experiments by Martinelli et al. (2007), moreover demonstrate that the amplitude of the periodic fluctuation of the PVC, is dependent on both *Re* and *S* while the characteristic size of the precession is almost independent on *Re*.

Yazdabadi et al. (1994) analyze also the presence of helical engulfment vortices that are also produced on the outside of the flow and serve as the initial entrainment mechanism for external flow. From the flow visualizations by Panda and McLaughlin (1994) it is possible to see that the rolling up of the axial shear layer around the jet into weak, irregular, large-scale organized structures, if compared to a non-swirling jet, is characterized by a considerably smaller overall growth of the instability waves and vortex pairing is suppressed. McIlwain & Pollard (2002) investigate with large eddy simulations the near fields of turbulent round free jets with swirl numbers of S = 0.0 and 0.24. Ring vortex structures, aligned with the plane normal to the flow, form downstream of the jet shear layer and collide with stream-wise braid structures. The resulting interaction causes the rings to break apart into smaller, less organized turbulence structures. The results suggest that the increased entrainment observed in swirling flows is due to the action of the braids rather than to the rings. Liang & Maxworthy (2005) investigate centrifugally unstable swirling jets at Re = 1,000 with flow visualization and digital Particle Image Velocimetry in a very outstanding paper. Four regimes of swirl number were covered: non-swirling jets with S =0, weakly swirling jets in the range, $0<S<S_{c1}$, strongly swirling jets before vortex breakdown with $S_{c1} < S < S_{c2}$, and stable vortex breakdown for $S > S_{c2}$, where S_{c1} =0.6 and S_{c2} =0.88. Kelvin–Helmholtz instabilities in the axial shear layer dominate non-swirling and weakly swirling jets. After the introduction of rotation, the combined axial and azimuthal shear layers become unstable to a modified form of Kelvin-Helmoltz instability.

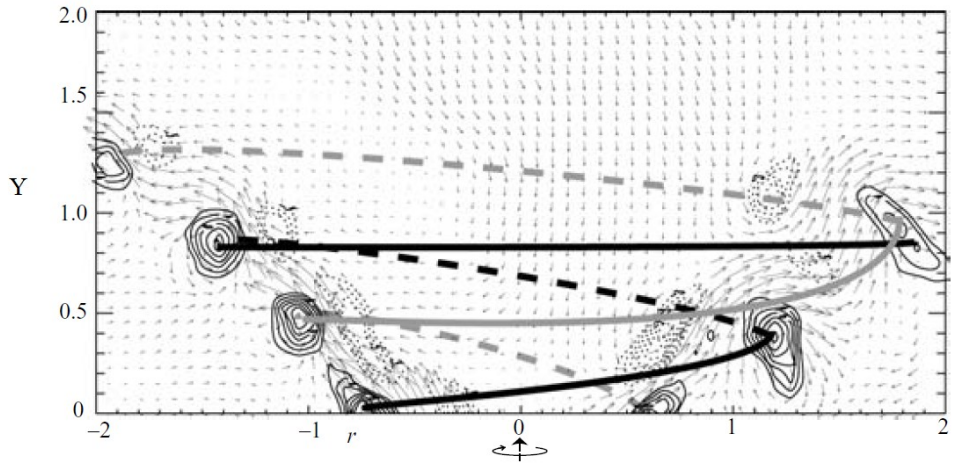

Fig. 1.11 Helical vortices visualized by Liang and Maxworthy (2005)

For weak swirl, tilted vortex rings evolve downstream. For strongly swirling jets, vorticity in the azimuthal shear layer, formed by the azimuthal or swirl velocity, grows and becomes comparable with vorticity in the axial shear layer. The flow loses its axis-symmetry and strong helical waves (see Fig. 1.11)replace vortex rings as the dominant vortex structure before vortex breakdown. The definition of a critical value and the definition of the helical waves is in agreement with previous studies (Billant et al., 1998). The visualizations with laser induced fluorescence and the quantitative measurements with Laser Doppler Anemometry done by Billant et al. (1998) find also an hysteretic behavior related to the stability of the vortex breakdown.

Indeed, according to the inviscid three-dimensional vortex dynamics simulations by Martin and Meiburg (1996) there is a nonlinear interaction and competition between a centrifugal instability and Kelvin–Helmholtz instabilities feeding on both the components of the base flow vorticity. Under axis-symmetric flow conditions, the swirl leads to the emergence of counter-rotating vortex rings. Also the work of Hu et al. (2001), is focused on the interaction between the primary vortex ring and the stream-wise vortex core. The direct numerical simulations done by Hu et al. (2001) depict a secondary vortex structure with opposite azimuthal vorticity near the vortex core. Then a vortex pair consisting of the primary and secondary vortices forms and travels radially away from the symmetry axis, causing a rapid increase of the thickness of mixing layer. The streamwise vortex layer developed in the early stage of evolution due to azimuthal instability breakdowns into small vortices under the joint stretch of the axial and azimuthal shear. Those vortex

structures are identified also by Cala et al. (2006) with a Laser Doppler Anemometry experiment coupled with phase-averaging analysis on the unsteady precessing flow in a model vortex burner. Three precessing spiral vortex structures are identified: a primary vortex that corresponds to the precessing vortex core, an inner secondary vortex, and outer secondary vortex that probably correspond to the vortex structures identified by Hu et al. (2001). In their conditions the PVC is the primary and most powerful structure as it includes the primary vorticity generated by the swirler; the inner secondary vortex and the outer secondary vortex are considered as secondary vortical structures. The jet breakdown zone is the conjunction of a pair of co-rotating co-winding spiral vortices, PVC and inner secondary vortex.

Chapter 2: Tomographic Particle Image Velocimetry

The instantaneous measurement of the 3D velocity fields is of great interest to fluid mechanics research as it allows to reveal the complete topology of unsteady coherent flow structures. Moreover, 3D measurements are relevant for those situations where the flow does not exhibit specific symmetry planes or axes and several planar measurements are required for a sufficient characterization. In particular this applies to flow turbulence, which is intrinsically 3D and its full description therefore requires the application of measurement techniques that are able to capture instantaneously its 3D structure, the complete stress tensor and the vorticity vector. The advent of PIV and its developments (stereo-PIV, Arroyo and Greated 1991; dual-plane stereo-PIV, Kähler and Kompenhans 2000) show the capability of the PIV technique to quantitatively visualize complex flows. Several different methods are proposed to achieve a 3D version of the technique (3D PTV, Maas et al. 1993; scanning light sheet, Brücker 1995; holography, Hinsch 2002) but recently the most assessed three-dimensional three-components flow measurement technique is Tomographic Particle Image Velocimetry (Elsinga et al. 2006), used in the present study. Recordings of particle images from an illuminated volume taken from several viewing directions simultaneously are used to reconstruct the 3D light intensity distribution. Provided that two subsequent exposures of the particle images are obtained, the measurement technique returns the instantaneous velocity field within the measurement volume by means of 3D particle pattern reconstruction and cross-correlation.

2.1 Working principle of tomographic PIV

The working principle of tomographic PIV is schematically represented in Fig. 2.1. Tracer particles immersed in the flow are illuminated by a pulsed light source within a 3D region of space. The scattered light pattern is recorded simultaneously from several viewing directions using CCD cameras as done in stereo-PIV with two cameras, applying the Scheimpflug condition between the image plane, lens plane and the mid-object-plane. The particles within the entire volume need to be imaged in focus, by setting a proper $f/\#$. The 3D particle distribution (the object) is reconstructed as a 3D light intensity distribution from its projections on the CCD arrays. The reconstruction is an inverse problem and its solution is not straightforward since it is in general underdetermined: a single set of projections can result from many different 3D objects. Determining the most likely 3D distribution is the topic of tomography (Herman and Lent 1976), which is addressed in the following paragraph. The particle displacement (hence velocity) within a chosen interrogation volume is then obtained by the 3D cross-correlation of the reconstructed particle distribution at the two exposures. The cross-correlation algorithm is based on the cross correlation analysis with the iterative multigrid window deformation technique (WIDIM, Scarano and Riethmuller 2000) extended to 3D. The relation between image (projection) coordinates and the physical space (the reconstruction volume) is established by a calibration procedure common to stereo PIV. Each camera records images of a calibration target at several positions in depth throughout the volume. The calibration procedure returns the viewing directions and field of view. The tomographic reconstruction relies on accurate triangulation of the views from the different cameras.

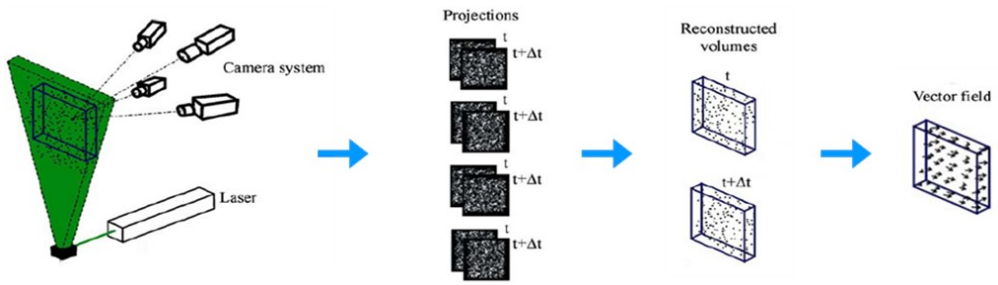

Fig. 2.1 Principle of tomographic-PIV

The requirement for a correct reconstruction of a particle tracer from its images sets the accuracy for the calibration to a fraction of the particle image size. Therefore, a technique for the a-posteriori correction for the system misalignment can significantly improve the accuracy of reconstruction (Wieneke 2008). The mapping from physical space to the image coordinate system can be performed by means of camera models created in photogrammetry and now well assessed in the experimental fluid mechanics community (Willert 2006).

2.1.1 Tomographic reconstruction algorithm

The novel aspect introduced with tomographic-PIV is the reconstruction of the 3D particle distribution by optical tomography. By considering the properties of the measurement system, it is possible to select a-priori the reconstruction method expected to perform adequately for the given problem. First the particle distribution is discretely sampled on pixels from a small number of viewing directions (typically 3 to 6 CCD cameras) and secondly it involves high spatial frequencies. In these conditions algebraic reconstruction methods are more appropriate with respect to analytical reconstruction methods, such as Fourier and back-projection methods (Verhoeven 1993). For this reason, only the former class of methods is considered for further evaluation

The distribution of the light scattered by the tracer particles, imaged instantaneously by multiple CCD arrays or cameras from different viewing directions, is a function of three spatial coordinates. The problem of tomographic reconstruction can be formulated as follows: given a finite set of projections of an object function $f(X,Y,Z)$, determinate the best estimate of it.

A wide variety of algorithms has been developed; currently the most adopted techniques in medical and astronomical imaging involve convolution and Fourier transform. The main drawback is that these techniques require a large amount of uniformly spaced projections; this optimal condition is not achievable in the case of Tomo-PIV, in which the observed object is unsteady (also in case of steady velocity field), and the number of optical access to the facility is usually limited.

Anyway, the algebraic reconstruction techniques (Herman e Lent 1976) appear to be well suited for the reconstruction of diffraction limited particle images, involving high spatial frequencies. The algebraic methods imply the discretization of the control volume as a 3D array of cubic voxels. A cubic voxel element is a compact support function, centred in the physical space point of coordinates (X,Y,Z), with a uniform

non-zero value $f(X,Y,Z)$ inside and zero elsewhere. The imaging process is modelled as a set of linear equations, derived by weighted discrete integration of the voxel intensity along each pixel's line of sight, determining the values of the projections:

$$p(x_i, y_i) = \sum_{j=1}^{N_{vox}} \Psi_{i,j} \cdot f(X_j, Y_j, Z_j) \qquad 2.1$$

where N_{vox} is the number of voxels adopted for the discretization, and $p(x_i,y_i)$ is the i-th projection. The weighting element $\Psi_{i,j}$ determines the contribution of the j-th voxel to the intensity recorded on the i-th pixel, and is a function of the distance between the line of sight and the centre of the voxel itself. Of course, the values of the weighting elements range between 0 and 1.

Several approaches are adopted in literature for the computation of the elements of the weighting matrix; e.g., a nearest neighbour criterion involves a unitary contribution if the voxel is intercepted by the line of sight, and zero elsewhere. Anyway, this approach lacks in accuracy, determining discretization artefacts. The correct way is to estimate the weighting elements with a voxel/line of sight interception as done by Elsinga et al (2006), i.e. the contribution of each voxel is determined as the intersecting volume between the line of sight (represented as an equivalent cylinder, with cross sectional area equal to that of the pixel) and the voxel, modelled as a an equivalent sphere. The intersecting volume is then normalized with the volume of the voxel, and it depends only on the resolution ratio (i.e. the diameters of the cylinder and of the sphere) and the distance between the line of sight and the centre of the voxel (Lamarche and Leroy, 1990).

The linear system (Eq. 2.1) is largely undetermined, i.e. a wide set of different solutions could be found. The huge dimensions of the system of equations prevent the solution by means of the classical optimization method, and several iterative algorithms are developed. Anyway, each of them solves the system under a different optimization criterion; an analysis of the reconstruction algorithms show that MART provides better performances with a smaller number of iterations (Atkinson and Soria 2007), and for this reason it is widely used for Tomo-PIV. Anyway, the reconstruction could be affected by artefacts, commonly defined ghost particles (Maas et al 1993), due to unresolved ambiguities on the position of the particles along the depth direction at the intersections of the lines of sight.

Starting from a suitable initial guess for the volume distribution $f^0(X,Y,Z)$, MART updates the object function as follows:

$$f^{k+1}\left(X_j,Y_j,Z_j\right)=f^k\left(X_j,Y_j,Z_j\right)\cdot\left(\frac{p\left(x_i,y_i\right)}{\sum_{j=1}^{N_{vox}}\Psi_{i,j}f^k\left(X_j,Y_j,Z_j\right)}\right)^{\chi\Psi_{i,j}} \qquad 2.2$$

where k is the iteration number, and χ is the relaxation parameter, chosen to be less than one in order to satisfy the stability criterion of the technique (Herman e Lent 1976). One iteration implies an external loop on the pixel values, and an internal loop with correction of each voxel by a factor based on the ratio between the recorded pixel intensity and the projection of the voxel intensity values along the line of sight. MART converges to the maximum entropy solution, i.e. the most probable solution based on the recorded values.

2.1.2 Volume correlation

The well-assessed PIV interrogation algorithms are based on the estimation of the velocity field by using cross-correlation (Willert and Gharib 1991, Keane and Adrian 1992).

In Tomographic PIV it is possible to suppose cubic interrogation volumes, without any loss of generality:

$$\phi_{l,m,n}=\frac{\sum_{i,j,k}^{\Lambda}\eta_{i,j,k}^2\left(G1_{i,j,k}-\mu_{G1}\right)\left(G2_{i-l,j-m,k-n}-\mu_{G2}\right)}{\sqrt{\sum_{i,j,k}^{\Lambda}\eta_{i,j,k}^2\left(G1_{i,j,k}-\mu_{G1}\right)^2\cdot\sum_{i,j,k}^{\Lambda}\eta_{i,j,k}^2\left(G2_{i-l,j-m,k-n}-\mu_{G2}\right)^2}} \qquad 2.3$$

where *G1* and *G2* are the grey intensities of the interrogation volumes extracted from the first and the second one respectively, μ_{G1} and μ_{G2} are their mean intensities, Λ is the linear dimension of the interrogation volume, and η is a weighting function.

In general all the main results obtained for image correlation can be applied also to volume correlations. When η is constant (i.e. a top hat window), Eq.2.3 reduces to a standard normalized cross-correlation. By considering the denominator constant and the grey intensities periodic, it can be quickly evaluated with the aid of FFT (Raffel et al. 1998). Weighting factors can be used to reduce the bias error caused by the imposed periodicity (Westerweel 1993, Raffel et al. 1998). The multistep

algorithms based on iterative discrete windows offset (Soria 1996, Westerweel et al 1997, Scarano and Riethmuller 1999) or image deformation methods (Scarano 2002) are of common use, relying on the estimation of a predictor displacement field on a coarse grid with interrogation windows dimension chosen in agreement with the one-quarter rule (Keane and Adrian, 1992), and corrector displacement computation on a finer grid.

2.1.3 The bias errors caused by the ghost particles

The measured flow statistics evaluated with tomographic PIV experiments and compared against other data appear to agree to within approximately 0.3 pixel particle displacement (Elsinga 2008) showing that the method can be very accurate.

Although the reported accuracy of the Tomographic PIV technique is hopeful, very little is known about possible velocity bias errors that may appear when the experimental conditions are changed. Here, a distinction needs to be made between the errors introduced in the imaging and cross-correlation steps of the experimental procedure, and the errors coming from the tomographic reconstruction. The first ones are in common with planar PIV and have already been documented (for an overview see Raffel et al. 1998), while the latter are object of recent investigations (Elsinga et al 2011).

When a ghost particle is formed from the same set of actual particles in both reconstructed volumes used in the cross-correlation analysis, bias errors are introduced in Tomographic-PIV velocity measurements. The displacement of the resulting ghost particle pair is approximately the average displacement of the set of associated actual particles.

Elsinga et al. (2011) show that the bias error does not significantly affect the measured flow topology as deduced in an evaluation of the local velocity gradients. Instead, it leads to a systematic underestimation of the measured particle displacement gradient magnitude. This phenomenon is alleviated when the difference between particles displacement along the volume depth is increased beyond a particle image diameter, or when the reconstruction quality is increased or when the accuracy of the tomographic reconstruction is improved.

2.2 Recent improvements in Tomographic PIV

The research community in tomographic PIV is currently working on two principal improvements: the reduction of the computational cost and the improvement of the measurement accuracy.

2.2.1 Reduction of computational cost

The relevant computational cost hampers the spread of Tomographic PIV as a common measurement tool and it is widely recognized that the tomographic reconstruction is the main bottleneck in Tomo-PIV applications: Hain et al. (2008) quote a processing time of 30 minutes on a eight cores computer for each volume with a size of 1430 x 1389 x 217 voxels using 4 MART iterations, while the adoption of higher resolution cameras (11 Mpixels) is strongly limited by a computational cost of 34 hours on a dual-core computer for the reconstruction of a volume with a size of 3512 x 2562 x 599 voxels. On the other hand, solely the storage of the reconstructed distributions requires about 1.7 GB and 21.6 GB, for the aforementioned applications respectively, with single precision floating point data. Taking into consideration the need of storing a weighting matrix to perform the reconstruction, whose number of elements is of the order of magnitude of at least 16 times the number of voxels for a 4 cameras system, it is evident that significant improvements are required.

Several efforts aimed to reduce both the computational cost of the reconstruction and the memory storage while retaining the same accuracy are present in literature. Most of the suggested solutions are based on the observation that the distributions to be reconstructed are very sparse. In fact, according to Keane and Adrian (1992), 10 particles in each interrogation volume are sufficient to guarantee a valid detection probability in PIV processing above 95% (though the absence of out of plane motion, affecting the planar PIV, can induce to slightly stretch the requirement for 3D PIV, enabling an improvement in terms of spatial resolution). If a cube of 32 x 32 x 32 voxels is considered, and proper *f/#* and resolution ratio are set to obtain a diameter of the particles of about 3 voxels, less than 1% of the voxels is characterized by a non-zero intensity value. Anyhow, as observed by Atkinson and Soria (2009), ambiguities in the reconstruction process and limited viewing angles determine the presence of noise and spurious voxel intensities, increasing the percentage of voxels with non zero intensity to approximately 5%.

Besides, the adoption of an iterative reconstruction technique implies a certain dependence of the first guess on the rate of convergence. A uniform first guess is commonly assumed (Elsinga et al., 2006), but several alternative solutions have been proposed, mainly enjoying the possibility of identifying locations with zero intensity in advance. Worth and Nickels (2008) propose a multiplicative first guess to estimate the initial intensity field. The multiplicative first guess is mainly based on back-projection of the recorded images throughout the volume, with a suitable threshold; the obtained fields are then multiplied in order to identify the locations with zero-intensity (or below a certain threshold), whose values will be no longer updated during the process. Anyway, an efficient application of multiplicative first guess coupled with MART requires the storage of at least one weighting element per camera and for each voxel; if sufficient computational resources are not available, the weighting elements have to be calculated every time they are needed, increasing considerably the processing time of multiplicative first guess, while the MART algorithm is less affected by this issue. A smart alternative solution has been given by Atkinson and Soria (2009), based on straightforward projection of the voxels on the image planes to determine whether their intensity is zero or not; the approach has been named MLOS (Multiplicative Line Of Sight). Non-zero projections on each camera are multiplied to obtain a suitable first guess, successively refined by means of a Simultaneous Multiplicative Algebraic Reconstruction Technique (SMART, Mishra et al., 1999). As a matter of fact, MLOS is a simplified and faster but less accurate iteration of SMART. The adoption of 40 MLOS-SMART iterations enables the acceleration of the reconstruction process of 3.8 times for a seeding density of 0.05 particles per pixel in a two-dimensional simulation for a 3 cameras setup, achieving the same accuracy of the standard method based on 5 MART iterations. However, this advantage quickly collapses by increasing the seeding density. Furthermore, both multiplicative first guess and multiplicative line of sight do not provide attenuation of the intensity of the ghost particles. As common in iterative processes, a non accurate first guess could determine a slower convergence; obviously, it's a key task to reduce as much as possible the number of iterations necessary to obtain an acceptable quality of the reconstruction, in order to speed up the whole Tomo-PIV process.

In order to solve this problem Discetti and Astarita (2011a) propose a multi-resolution (MR) reconstruction approach, consisting in the initial reduction of the dimension of the reconstruction problem by means of a binning-like compression of the images, maintaining, at the same time, a

resolution ratio equal to one between voxels and pixels, i.e. the reconstruction is carried out on a coarser grid in the first iterations. The combination of the multi-resolution approach with MLOS performs the reconstruction noticeably faster than the standard method based on 5 MART iterations; a remarkable reduction in the memory needed to store the weighting matrix is also obtained. Furthermore, with the same total number of iterations, a slight improvement in accuracy is observed.

Most of the attention is aimed to the decrease of the computation effort only of the tomographic reconstruction. A natural extension of the multi-resolution technique can be employed to obtain a noticeable reduction of the computational cost to estimate the predictor displacement field (according to Discetti and Astarita (2011b) the speed-up is approximately equal to the cube of the binning factor, with a certain overhead to calculate the binned distributions).

2.2.2 Improvement of measurement accuracy

According to the simulations by Elsinga et al. (2006), it is assessed that a quality factor (i.e. the correlation factor between the exact and the reconstructed distributions) higher than 0.75 is required to obtain reliable measurements of the velocity field by 3D cross-correlation. This requirement limits the spatial resolution of the technique since, with a 4 camera system, a maximum seeding density of 0.05 particles per pixel is needed to obtain a satisfactory reconstruction.

Novara et al. (2009) introduced a Motion Tracking Enhanced (MTE) algorithm to build a first guess distribution for the MART corrective procedure. The method is based on an iterative procedure in which a first guess distribution, obtained by straightforward application of MART, is subsequently refined by the computation of pseudo-simultaneous objects from the recording views at different times. MTE is particularly effective in presence of relatively strong velocity gradient along the depth direction, since ghost particles generated by a set of true particles reoccur in both the exposures, and move coherently with the true ones, only if the displacements differ of a small quantity (less than one particle diameter), as observed by Elsinga et al. (2011). The algorithm noticeably increases the allowed maximum seeding density, but it is computationally much more intensive than the simple application of MART, since it requires in addition 3D cross-correlation between the exposures to identify a predictor field, and to reconstruct the pseudo-simultaneous objects.

An improvement of the rate of convergence can be obtained also developing algorithms devoted to the reduction of the intensity of the ghost particles, in addition to that performed by MART. According to Discetti and Astarita (2011c), a filtering of the distribution after each MART iteration is suggested; the filtering windows are chosen in agreement with the observation that the ghost particles are often elongated along the depth of the volume, since they occur due to ambiguity of the solution in that direction.

There is a broad literature about techniques for improvement of image correlation; few works have been published documenting the use of volume correlation improvement techniques: In the work by Violato and Scarano (2011), time-resolved velocity vector fields are obtained by averaging the cross-correlation map over three subsequent object-pairs. Such an approach is an extension of the method proposed by Meinhart et al. (2000) that can be applied for unsteady velocity fields sampled with rate higher than that strictly needed for temporally resolving the flow. The main advantage is the reduction in precision error without compromising the temporal resolution.

The sole attempt reported for the analysis of three-dimensional data with adaptive volume correlation is the work from Novara et al. (2011): they propose an adaptive criterion based on the use of ellipsoidal interrogation volumes The adaptive criterion is based on the analysis of the local velocity gradient tensor and allows to stretch and align the interrogation volumes along the direction where the velocity variation is minimum, reducing the averaging effect of cross-correlation along the direction with maximum velocity variation, maintaining constant the interrogation volume size and therefore the number of particles inside of it.

Chapter 3: Infrared thermography for convective heat transfer measurements

Measuring heat fluxes in thermo-fluid-dynamics requires both a thermal sensor (with its related thermo-physical model) and temperature transducers. In standard techniques, where temperature is measured by thermocouples, resistance temperature detectors (RTDs) etc., each transducer yields either the heat flux at a single point, or the space-averaged one; hence, in terms of spatial resolution, the sensor itself has to be considered as zero-dimensional. This limitation makes measurements particularly troublesome whenever the temperature, and/or heat flux, fields exhibit high spatial variations. Instead, the infrared (IR) camera constitutes a truly two-dimensional transducer, allowing for accurate measurements of surface temperature maps even in the presence of relatively high spatial gradients. Accordingly, the heat flux sensor also becomes two-dimensional, as long as the necessary corrections are applied.

When compared to standard techniques, the use of the infrared camera as a temperature transducer in convective heat transfer measurements appears advantageous from several points of view. In fact, since IR camera is fully two-dimensional (up to 1 Mpixels), besides producing a whole temperature field, it permits an easier evaluation of errors due to radiation and tangential conduction; furthermore, it is non-intrusive (e.g., allowing conduction removal through thermocouple or RTD wires), it has high sensitivity (down to 20 mK) and low response time (down to 20 μs). As such, IR thermography can be effectively employed to measure convective heat fluxes with both steady and transient techniques.

The first IR cameras were developed in the 1960s as offshoots of military programmes but without accuracy features, not mandatory for the existing needs. The 1970s energy crisis brought government support in Sweden and so the first radiometric thermal imagers were developed by

AGA and Bofors, both Swedish companies. These cameras used a single detector, the image two-dimensionality being achieved by rotating, or oscillating, mirrors and/or refractive elements (such as prisms) which scanned the field of view (FOV) in both vertical and horizontal directions; in fact, they were also called infrared scanning radiometers.

The detector of these radiometers was the photon one, where the release of electrons is directly associated with photon absorption, its main features being a quite short response time and limited spectral response. Such detector requires cooling, well below ambient temperature to allow for rapid scanning, high sensitivity and low noise. In fact, the sensor was often located in the wall of a Dewar vessel filled with liquid nitrogen ($77K$). Subsequent scanning radiometers used various types of cooled photon detectors with lower time constants allowing frame rates of 15-30Hz. All real time commercial cameras used cooled photon single detectors with optomechanical scanning well into the 1980s, when (staring) infrared Focal Plane Array (FPA) detectors, having quite adequate time constants to achieve 30-60Hz frame rates, were introduced. By using these staring arrays, the infrared camera, long restricted to a point sensing instrument, became an effective two-dimensional transducer. IR cameras based on non-cooled FPA thermal detectors (such as microbolometers) emerged in the mid 1990s and led to the development and diffusion of thermal imagers requiring no cooling.

The earliest attempts to measure heat transfer coefficients arose in the hypersonic regime and were performed by using scanners operating in the middle IR band ($3 \div 6 \mu m$) of the infrared spectrum, at the time called short wave IR band. In particular, the AGA Thermovision 680SWB camera was employed by Thomann and Frisk (1967) to measure the heat flux distribution on the surface of an elastomeric paraboloid in a hypersonic wind tunnel at Mach number equal to 7. The thin-film sensor (described in the third paragraph of this chapter) was used to determine convective heat transfer coefficients, which showed good agreement with data already obtained with other techniques, and was encouraging in view of using IR systems for heat flux measurements. Once the method was shown to work, efforts were mainly oriented towards comprehension of potential errors sources which could affect measurement accuracy and especially to developing devices which could ease IR camera use. Compton (1972), at NASA Ames, realized that the bottleneck of IR thermography was data acquisition, storage and processing. The solution was devised in the automation of data

processing and this concept finally brought to the systems currently in use.

Apart from heat flux evaluation, the characterization of flow field behaviour, with location of boundary layer transition to turbulence and of flow separation and reattachment zones, constituted a subject of great interest to aerodynamicists and efforts were devoted to acquire information on IR camera capability to deal with these phenomena. The boundary layer transition over a flat plate was examined by Peake et al. (1977), who detected the different adiabatic wall temperatures that occur amongst laminar and turbulent flows.

A first analysis of heat transfer measurements by IR thermography and a review of some of their applications were presented by Carlomagno and de Luca (1989). Gartenberg and Roberts (1992a) reported an extensive retrospective on aerodynamic research with infrared cameras.

In this chapter, the basic principles of radiation necessary to perform IR thermography are briefly recalled from the user point of view, the infrared camera with its main features and the most commonly used heat flux sensors are revised, then the heated thin foil heat transfer sensor, used in this thesis, is described in detail.

3.1 Basic principles of radiation heat transfer

Heat transfer by radiation (Siegel and Howell, 1992) is an energy transport mechanism that occurs in the form of electromagnetic waves. Via this heat transfer mode, energy can also travel in vacuum and may be partially absorbed and reflected by a body, or even pass through it. By denoting with α_r the radiation fraction being absorbed by the body, with ρ_r the fraction being reflected by it and with τ_r the fraction being transmitted (which passes through), energy conservation requires:

$$\alpha_r + \rho_r + \tau_r = 1 \qquad 3.1$$

where: α_r, ρ_r and τ_r are respectively called absorptivity, reflectivity and transmissivity coefficients of the body under consideration and may depend on both radiation wavelength (spectral) and propagation direction (directional).

Radiation is emitted by all bodies at an absolute temperature $T > 0$ and, for non-transparent bodies ($\tau_r = 0$), it origins from their surface only. The body which emits the greatest amount of energy at a given temperature is called black body.

The law that prescribes the energy flux (energy rate per unit body area) per wavelength (spectral hemispherical emissive power) $I^b(\lambda)$ $[W/m^3]$, which is emitted by a black body in the hemisphere outside its surface, is the Planck's law of radiation:

$$I^b(\lambda) = \frac{C_1}{\lambda^5 \left(e^{C_2/\lambda T} - 1\right)} \qquad 3.2$$

where: λ is the radiation wavelength (m), T the absolute black body temperature (K) and C_1 and C_2 the first and the second universal radiation constants, respectively equal to 3.7418 x 10^{-16} Wm^2 and 1.4388 x $10^{-2}$$m$-$K$. Eq. 3.2 represented in Fig. 3.1, shows that I^b leads to zero for both $\lambda \to 0$ and $\lambda \to \infty$. It has to be noted that, for a black body, the radiation intensity (per unit solid angle) based on the body area projected normally to the direction of emission is independent of the latter.

The electromagnetic spectrum is roughly divided into a number of wavelength intervals called bands. The infrared spectral band, of interest within the present context, is generally sub-divided into four smaller bands with arbitrarily chosen boundaries: near infrared ($0.75 \div 3\mu m$), middle infrared ($3 \div 6\mu m$), far or long infrared ($6 \div 15\mu m$) and extreme infrared ($15 \div 1000\mu m$). Most currently used IR camera detectors are

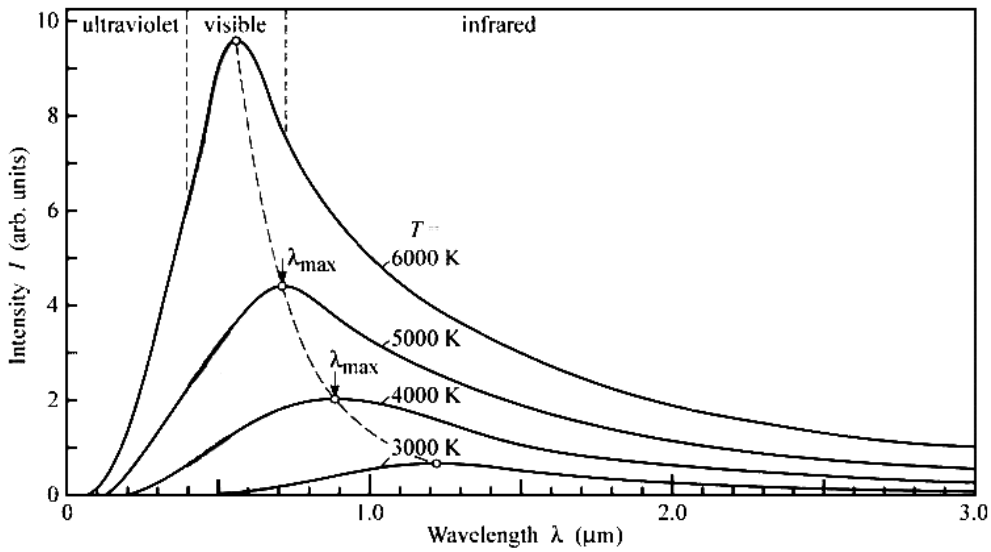

Fig. 3.1 Black-body radiation curves. Note the different regions of the electromagnetic spectrum

sensitive in the middle (MWIR) and the long (LWIR) spectral bands, but the band between ~5 and ~7.5μm is seldom used because of its rather high atmospheric absorption. Detectors are also available in the near infrared (NIR), sometimes called short wavelength (SWIR), and in the extreme infrared bands, but they are not generally used for thermo-fluid-dynamic applications. By deriving and integrating with respect to λ, Planck's law leads, respectively, to the following two other laws:

Wien's displacement law: the wavelength λ^* at which the black body emits its maximum spectral emissive power is a function of the absolute black body temperature according to:

$$\lambda^* T = 2897.8\ \mu m\text{-}K \qquad 3.3$$

i.e., the maximum value of I^b moves toward shorter wavelengths as the body temperature increases. E.g., at liquid nitrogen temperature ($77K$) $\lambda^* \approx 38\mu m$, at room temperature $\lambda^* \approx 10\mu m$, while the sun (at about $6000K$) emits yellow light peaking around $0.5\mu m$ in the visible light spectrum. This explains why IR cameras mainly operate in MWIR and LWIR bands.

Stefan-Boltzmann's law: The total (over all wavelengths) hemispherical emissive power E^b (W/m^2) also depends on the absolute black body temperature alone, according to:

$$E^b = \beta T^4 \qquad 3.4$$

where β is the Stefan-Boltzmann's constant, which is equal to 5.6704 x 10^{-8} W/m^2K^4. However, since infrared camera detectors capture only a limited band of the whole electromagnetic spectrum, while making measurements with IR thermography, Planck's law (Eq. 3.2), rather than Stefan-Boltzmann's law (Eq. 3.4), has to be applied.

Real objects almost never comply with the above-described laws even if they may approach the black body behaviour in certain spectral bands and conditions. A real object generally emits only a fraction $I(\lambda)$ of the radiation emitted by the black body $I^b(\lambda)$ at the same temperature and wavelength. For the sake of ease, $I(\lambda)$ is always referred to the spectral hemispherical emissive power. By introducing the spectral emissivity coefficient, defined as:

$$\varepsilon(\lambda) = I(\lambda)/I^b(\lambda) \qquad 3.5$$

Eq. 3.2 can be rewritten for real bodies by simply multiplying its second term by $\varepsilon(\lambda)$:

$$I(\lambda) = \varepsilon(\lambda)\frac{C_1}{\lambda^5\left(e^{C_2/\lambda T}-1\right)} \qquad 3.6$$

Bodies having their emissivity independent of λ are called gray bodies. Kirchhoff's law states that the spectral emissivity coefficient is equal to the spectral absorptivity coefficient $\alpha_r(\lambda)$, that is the absorbed fraction of the radiation of wavelength λ. Therefore, for non-transparent bodies, such as those generally used in infrared thermography, Eq. 3.1 becomes:

$$\varepsilon(\lambda) + \rho_r(\lambda) = 1 \qquad 3.7$$

Therefore, materials with low emissivity ε (such as metallic ones) not only emit less energy, but also reflect a large amount of the radiation coming from the ambient and impinging on them. Whenever possible, they should not be employed in IR thermography or, if they must be necessarily used and transient heat transfer is not involved, the viewed body should be covered with a thin layer of thermally black paint (such as white dull enamel).

3.2 Infrared cameras

3.2.1 Camera hardware

The core of the IR camera system is the radiation detector. Detector technologies are mainly separated into two classes: thermal detectors, that are sensitive to the incident energy flux, and quantum detectors, whose sensitivity depends on photon absorption.

A currently common type of thermal detector is the uncooled microbolometer, made of metal compound or semiconductor material. The microbolometer typically has a lower cost and broadband IR spectral response, but is less sensitive and quite slower (response time in the milliseconds domain) than quantum detectors. The latter ones are made from materials such as InSb, HgCdTe (MCT), and layered GaAs/AlGaAs for QWIP (Quantum Well Infrared Photon) detector. Quantum detectors have a low response time (microseconds domain) and higher sensitivity than thermal ones, but strong cooling is still required. In actual cameras, miniature Stirling coolers easily achieve temperatures around $70K$.

In Fig. 3.2, the spectral responses of some of the most sensitive, largely used, cooled and uncooled infrared detectors and their relative detectivity are indicated. The response curves are shown in terms of D^* (detectivity star) for a specific exposure time, as a function of the spectral wavelength. D^* is the sensitivity figure of merit of the infrared detector detectivity, so that higher D^*s indicate better performance.

Modern quantum detectors and QWIP tend to approach the ideal (top curves) detector behaviour.

Nowadays, non-cooled microbolometers are typically employed in both MWIR and LWIR spectral bands. Instead, because of their respectively higher *D*s* (see Fig. 3.2), quantum detectors usually utilize InSb in MWIR band and HgCdTe, or QWIP, in LWIR band.

To carry out IR thermography, the choice of the most appropriate working spectral band (MWIR, or LWIR) depends on several factors often linked to object surface nature and to atmospheric absorption. Cameras in LWIR band, because of their band, thanks to low atmospheric absorption (except for very high water vapour content) and high thermal contrast, generally allow for high accuracy measurements; in particular, they are able to take data also in the presence of air plasma that typically does not emit in 8-12μm band (Cardone 2007). However, frequently

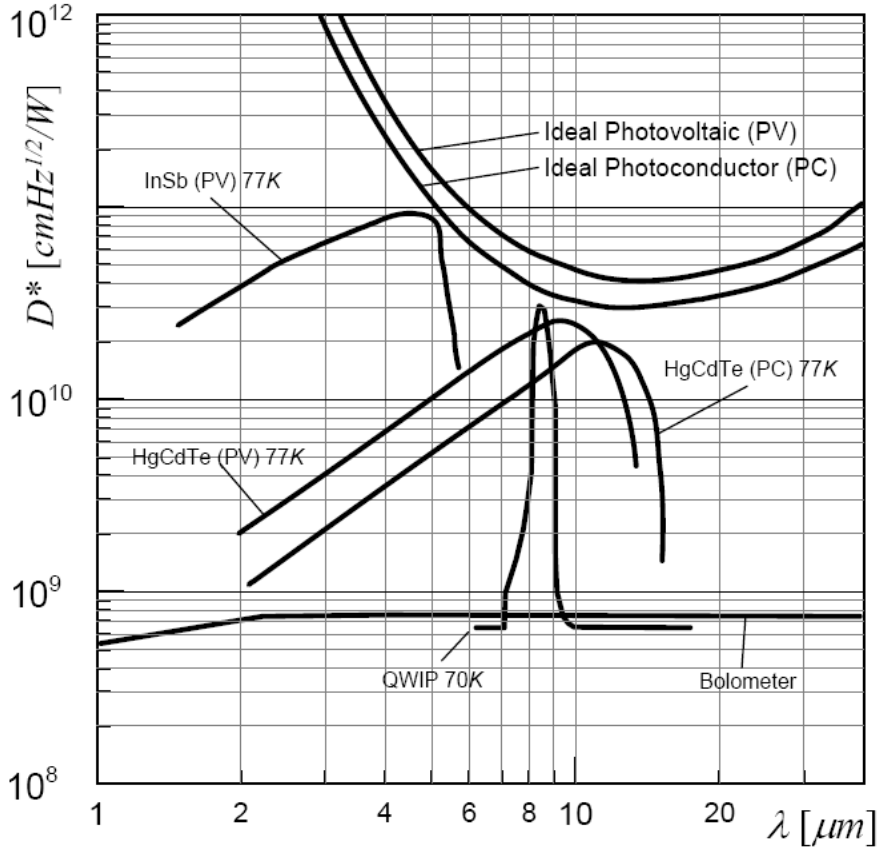

Fig. 3.2 Spectral responses of infrared detectors and relative detectivity *D
(from Ianiro and Cardone 2010)

MWIR cameras are preferred because of their lower cost detectors and optics, higher detectivity D^* for quantum detectors and since some surfaces have a higher emissivity coefficient in the middle infrared band. It has to be noted that, for temperatures higher than about $10\,°C$, temperature sensitivity is generally better for MWIR than for LWIR quantum detectors. When high sensitivity and very short response time are not required, the best and most cost-effective actual choice is a camera with non-cooled microbolometers.

The standard instantaneous output of each thermal image is generally constituted by a matrix of data from 10^5 up to 10^6 elements. Therefore, as already stated, a digital data processing is mandatory, altough easy to perform since practically all cameras have a digital output. The temperature range usually measured spans from -20 up to $+1500\,°C$, but it can be further extended to higher values by filtering the oncoming radiation. Typically, MWIR cameras use silicon optics, while the LWIR ones use germanium optics. Most of the available IR cameras offer also telescopes, expander lenses and supplementary close-up microscope lenses, i.e., the possibility of changing their optics, in order to adapt working distances to the scene one is looking at.

3.2.1 Camera performance

The performance of an infrared camera is conventionally evaluated in terms of thermal sensitivity, scan speed, image resolution and intensity resolution. Thermal sensitivity is generally defined in terms of (mean) noise equivalent temperature difference (NETD), which is the time standard deviation averaged over all pixels of a blackbody scene and is expressed in terms of *mK*. Some modern FPA systems are able to detect temperature differences of less than $20\,mK$ at ambient temperature.

The scan speed represents the rate at which a complete image (frame) is updated and is expressed in terms of frame rate (*Hz*). FPA systems of the last generation are characterized by high standard frame rates (often greater than $100\,Hz$) and, by the reduction of the number of acquired pixels (i.e., by windowing the frame) and their integration time (i.e., detector sensitivity), frame rates can currently go up to several ten thousands of *Hz*.

The image resolution, that is the capability of a system to measure surface temperature of small objects, is usually defined as instantaneous field of view (IFOV), which is expressed in terms of *mrad*; theoretically, IFOV is the ratio of detector pixel width over lens focal length. However, this is only an ideal design parameter and does not fully describe the

performance of the actual system. In fact, when a lens of reduced total field of view (FOV) is used, IFOV decreases, but the number of IFOVs in the frame remains the same. Then, the number of IFOVs (pixels) that describes the complete FOV gives a better description of the image resolution. Modern systems are able to produce images composed of up to several hundreds of thousands of pixels at standard frame rates. More rigorously, the spatial resolution of the IR camera may be defined in terms of the Modulation Transfer Function *(MTF_{IR}),* which is the mathematical description of the detected signal modulation (also due to the pixel finiteness) as a function of the spatial frequency (De Luca and Cardone 1991).

The intensity resolution, or dynamic range, is expressed in terms of number of digital intensity levels the thermal image is composed of. The latest generation of cameras provides typically 14-bit A/D conversion, which allows measuring small temperature differences even in the presence of a large temperature range in the viewed scene.

3.2.2 Camera calibration

The energy actually detected by an IR system depends not only on the emissivity coefficient of the surface under measurement, but also on environmental conditions. In fact, the total radiation I' detected by the camera can be written as:

$$I' = \tau_r \, \varepsilon I^b{}_{obj} + \tau_r (1-\varepsilon) I^b{}_{amb} + (1-\tau_r) I^b{}_{atm}, \qquad 3.8$$

where: τ_r is the transmissivity of the atmosphere between the surface and the camera, $I^b{}_{obj}$ is the radiation intensity corresponding to a black body at the object temperature T_{obj} , $I^b{}_{amb}$ is the black body radiation intensity corresponding to the (effective) temperature of the object surroundings T_{amb}, called the reflected ambient (or background) temperature and $I^b{}_{atm}$ is the radiation intensity corresponding to a black body at the temperature of the atmosphere $T_{atm.}$. In Eq. 3.8, the term $\tau_r \varepsilon \, I^b{}_{obj}$ is the emission from the surface captured by the radiometer, τ_r $(1-\varepsilon)$ $I^b{}_{amb}$ is the reflected emission from ambient sources, and $(1-\varepsilon)$ is the surface reflectivity (T_{amb} is assumed constant for all emitting surfaces of the half sphere seen from the object surface). The term $(1-\tau_r)$ $I^b{}_{atm}$ is the emission from the atmosphere, with $(1-\tau_r)$ being the atmosphere emissivity. For the sake of simplicity in the Eq. 3.8, the dependence from T and wavelength is not indicated.

Generally, the transmissivity of the atmosphere τ_r is assumed to be equal to unity, which simplifies Eq. 3.8. Thus, by using Eq. 3.2 and E.q. 3.8, a

semi-empirical adaptation of the Planck's law with the parameters *R*, *B*, and *F* can be found. The typical calibration function of an IR camera can be put in the form:

$$U_D = \varepsilon \frac{R}{e^{B/T_{obj}} - F} + (1-\varepsilon)\frac{R}{e^{B/T_{amb}} - F}, \qquad 3.9$$

where: U_D is the detected signal, *R* is a function of integration time and wavelength, *B* is a function of wavelength alone, and *F* is a positive value very close to 1. If the object used for calibration is a black body, the calibration constants *R*, *B* and *F,* besides taking into account the sensed wavelength band and the radiation constants, consider only emission and absorption from atmosphere.

A simpler way to perform the calibration, which does not take in account T_{amb} variations, is the *in situ* calibration proposed by Sargent et al. (1998), which practically neglects the second term of the second member of Eq. 3.9.

Needless to say that, if a window exists in the optical path between test section and IR camera (as may happen in wind tunnel measurements), the constants of Eq. 3.9 depend also on the transmissivity through such a window.

3.3 Heat flux sensors

The equation for convective heat flux *q''* (energy rate per unit area, W/m^2) between a fluid and a surface at a given temperature is reported in Eq. 1.3 ($q_c'' = h\,(T_w - T_{aw})$).

The present main interest is to measure either q_c'', or *h*. Heat-flux sensors of interest herein generally consist of plane slabs, with a known thermal behaviour, whose temperature has to be measured at predefined points. The energy conservation equation applied to the proper sensor model yields to the relationship by which measured temperatures are correlated to heat flux. In practice, the slab can also be curved, its curvature in such a case can be ignored only as long as the layer affected by the exchanged heat flux is small compared to the slab local curvature radius. The sensor is often supposed ideal, which means that its material thermo-physical properties are independent of temperature. The slab surface the flow is going over is called front surface, while the opposite one, back surface.

The simplest model of a sensor is the one-dimensional one, where the heat flux to be measured is supposed to be normal to the sensing element surface, i.e. the temperature gradient components parallel to the

slab surfaces are assumed to be negligible. The heat flux sensors mainly used with IR thermography are:

"Heated-thin-foil**":** this sensor consists of a thermally thin metallic foil, or a printed circuit board, steadily and uniformly heated by Joule effect. Foil heating can be accomplished also in a different way, e.g., by a known steady radiation input to foil. Measuring sensor surface temperature and performing an energy balance allows computing heat flux. In this sensor, due to foil thermal thinness, either one of its surfaces can be generally viewed by IR camera. An extension to foils not thermally thin can be also performed.

"Thin-film": classically, a very thin resistance thermometer (film) measures the surface temperature of a thermally thick slab to which is bonded. Heat flux is inferred from the theory of heat conduction in a semi-infinite solid. The surface film must be very thin so as to have negligible heat capacity and thermal resistance as compared to the layer affected by the exchanged heat flux. When using this sensor with IR thermography, the film does not exist and the heat-exchanging surface must be necessarily viewed by camera. As such, fluids at least partially transparent ($\tau_r \neq 0$) in the used IR band must be employed.

"Wall calorimeter", or "thin-skin": the slab is made thermally thin (so that its temperature can be assumed to be constant across its thickness) and is used as a simple calorimeter. Heat flux is computed from the time rate of the slab temperature change, usually measured by a thermocouple. In the use of this sensor with IR thermography, the skin can be made really thin, because there are no thermocouples, and either one of the slab surfaces can be generally viewed by the infrared camera.

A detailed analysis of the heat flux sensors that can be used with IR thermography can be found in Carlomagno and de Luca L. (1989) and Astarita el al. (2006).

Recently, heat flux sensors, based on a numerical solution of Fourier's law (typically described by an inverse heat transfer model) and surface temperature measurements, have been developed, e.g., to take into account temperature dependence of thermophysical properties and/or to have slabs with high curvature, but, for the sake of brevity, they are not described herein.

"Thin-film" and "wall calorimeter" sensors belong to the class of transient techniques, while "heated-thin-foil" sensor represents a steady technique. Transient techniques generally regard passive heating due to some existing temperature difference between sensor surface and flow, while heated-thin-foil involves active heating.

When using IR thermography, transient techniques should be mainly applied to experimentally analyze the constant convective heat transfer coefficient boundary condition, while the heated-thin-foil steady technique is functional to the constant heat flux one. A constant temperature boundary condition can be implemented with transient techniques, large temperature differences between sensor and flow and relatively short measuring times.

3.4 Heated thin foil heat flux sensor

By locally applying an energy balance (as sketched in Fig. 3.3) to a foil heated by Joule effect (by passing electric current through it) and cooled by air flowing on it in steady state conditions (for which the net heat flux is zero) the following relationship is obtained:

$$h = \frac{q''_j - q''_r - q''_k - q''_n}{T_w - T_{aw}} \qquad 3.10$$

with q''_j the Joule heat flux, q''_r the radiation heat flux, q''_n the natural convection heat flux on the rear foil surface, q''_k the tangential conduction heat flux, T_w the wall temperature and T_{aw} the adiabatic wall temperature.

The surface temperature distribution is measured by viewing the rear face of the foil (i.e. the side opposite to jet impingement). In fact, since the Biot number ($Bi=hs/k_f$ where s and k_f are thickness and thermal conductivity of the foil, respectively) is small with respect to unity, the temperature can be considered as practically uniform across the foil thickness. Each test run consists of two parts: first, with electric current off, Taw is measured and the so-called "*cold image*" is recorded; then,

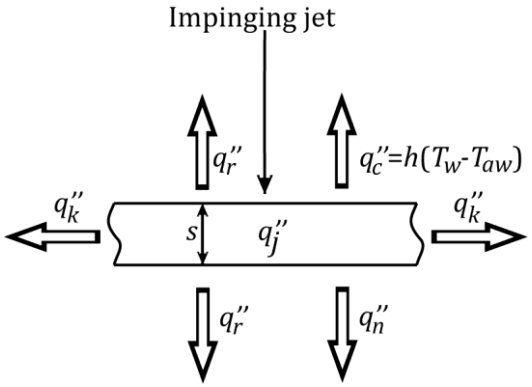

Fig. 3.3 Sketch of the local energy balance

electric current on, T_w is measured and the "*hot image*" is recorded.
According to Eq. 3.4 the net rate of radiation heat loss is estimated as:

$$q_r'' = \varepsilon\beta\left(T_w^4 - T_{amb}^4\right) \qquad 3.11$$

A little more complex is the procedure to compute thermal losses for tangential conduction. In particular, considering the foil plane with axes X and Z, thermal losses for tangential conduction can be expressed following Astarita and Cardone (2000):

$$q_k'' = q_k''(X,Z) = -\underline{\nabla}\cdot[s(X,Z)\underline{\underline{K}}(X,Z)\cdot\underline{\nabla}T(X,Z)] \qquad 3.12$$

Where $\underline{\underline{K}}$ is the local foil thermal conductivity tensor and s is the sensor thickness. For a metallic foil sensor, it is possible to write :

$$q_k'' = k_f s\cdot\nabla^2 T \qquad 3.13$$

As suggested by Carlomagno and Cardone (2010), thermal images are filtered before evaluating the Laplacian operator of the surface temperature in order to reduce the effect of the measurement noise.

Chapter 4: Flow field in free and impinging swirling jets

Flow field measurements performed in a water tank with tomographic PIV are presented in this chapter. A description of the experimental setup and of the swirling nozzles, obtained with helical inserts based on the concept of the cross swirling strips, is followed by the analysis of the flow fields.

Free swirling jets are investigated at Reynolds number equal to 1,000 in order to analyze the main coherent structures and their dynamics. First, averaged flow fields are quickly presented, then the vortex topology is described and vortex dynamics (vortex pairing and vortex breakdown) are discussed.

Swirling impinging jets are investigated at Reynolds number equal to 10,000 and nozzle to plate distance $H = 2$. The analysis is more focused on the consequences of the flow field on the heat transfer distribution, thus the coherent structures are discussed with a look at turbulence organization and turbulent kinetic energy on the impinged wall.

4.1 Experimental setup and procedure

4.1.1 Experimental facility

Flow field measurements presented herein are performed in the water jet facility at the Aerodynamics Laboratories of TU Delft in the Aerospace Engineering Department. The experimental apparatus for the present study is shown as an assembly sketch in Fig. 4.1. It consists of a vertical swirling jet (with a nozzle diameter of 19.7 *mm*) emerging from the bottom wall of the facility, a large stationary test tank; for the impinging jets experiments, the water tank is modified by introducing a square

Plexiglas target plate (with dimensions of 300x300 mm^2) as impingement plate at a distance of two diameters from the nozzle exit.

The test tank is designed as an octagonal water tank (600mm of diameter and 800mm of height) made of Plexiglas allowing full optical access for illumination and tomographic imaging and neutrally buoyant polyamide particles of 56 μm of diameter are employed as seeding particles. The water is recycled to maintain clarity and to save particles; in fact the water exiting the test tank is collected in a large reservoir and then pumped to another reservoir, which is suspended above the nozzle assembly and is used as starting point of the supply line, to filter oscillations of the flow rate and provide a constant-head inflow. The flow rate is controlled by several valves underneath the test tank and measured by means of a flow meter (a rotameter) located on the supply line before the nozzle. Before the experiments, the water is stored for at least one day in order to reach a uniform temperature.

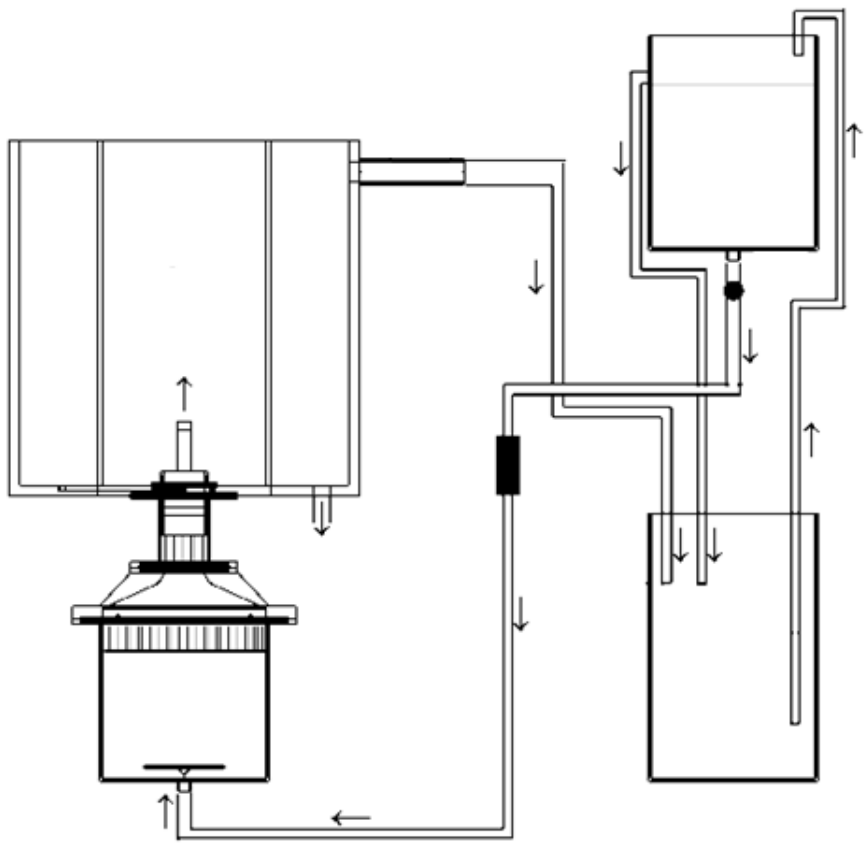

Fig. 4.1 Schematic of the experimental apparatus

For the impingement experiments the water is provided directly by the pump, taking the water from a hole in the bottom of the tank and sending it back in the supply line; the flow field was not affected by oscillations caused by the pump.

The basic nozzle subsystem is shown more in detail in figure Fig. 4.2. The swirling flow is obtained by passing the water in a cylindrical nozzle with four swirl vanes as swirl generator. The swirl vanes are obtained by means of a cross helical insert and several helical inserts with different pitch are used in order to produce different swirl number values.

The swirling jet nozzle ends in a sharp exit nozzle as a truncated tube even if many works in literature use contracting nozzles to produce laminar and uniform jets. In fact, experiments in literature show also that the fully developed swirling jets coming from contracting nozzles, (see e.g. Billant et al. 1998), have a central overshoot in the axial velocity within the vortex core; under these circumstances the inflow conditions are hard to control since it certainly affects the swirl number at which vortex breakdown is generated.

The two regulating parameters for the experiments performed in this work are the Reynolds number and the Swirl number. The water flow provides a stabilized supply in a range of exit flow rate corresponding to Reynolds numbers ($Re = 4\dot{m}/(\pi\mu D)$) between 500 and 15,000. The free jets experiments are performed at Reynolds number equal to 1,000 and the impinging jets experiments are performed in turbulent conditions at Reynolds number equal to about 10,000.

Swirl number is related to the swirl vane angle θ and, according to Gupta et al. (1984) is expressed as:

$$S = \frac{2}{3}\left[\frac{1-(d/D)^3}{1-(d/D)^2}\right]\tan\theta \qquad 4.1$$

where d is the vane pack hub diameter and θ is the swirling angle as shown in Fig. 4.2. In the present work, experimental campaigns are performed in order to analyze a non swirling jet, weak swirling jets (S = 0.2 and S = 0.4), the condition of transition between weak and strong swirl at S = 0.6 and a strong swirling jet (at S = 0.8).

4.1.1 Measured quantities

In the two investigations presented in this chapter, all the measured quantities are presented as non-dimensional. The reference velocity is the average exit velocity and the reference length is the nozzle diameter.

Both instantaneous and averaged flow fields are presented and discussed: Time-resolved Tomo PIV allows describing the evolution of the instantaneous flow field and of the vortex topology. Instantaneous velocity fields are shown and compared, observing the lifetime of the vortical structures visualized by means of the Q criterion (Jeong and Hussain 1995). On the basis of these quantitative vortex visualizations an attempt to define a general vortex topology is done.

The averaged flow fields (related to all the considered swirling conditions) are compared in order to analyze the global effect of swirl (e.g. analyzing the presence of the recirculation zone and the entrainment). In the case of the turbulent swirling impinging jets, the core of the discussion is the analysis of the development of the flow field in the wall jet and in the impingement region: here a lot of information is obtained also from the observation of flow statistics such as turbulent kinetic energy.

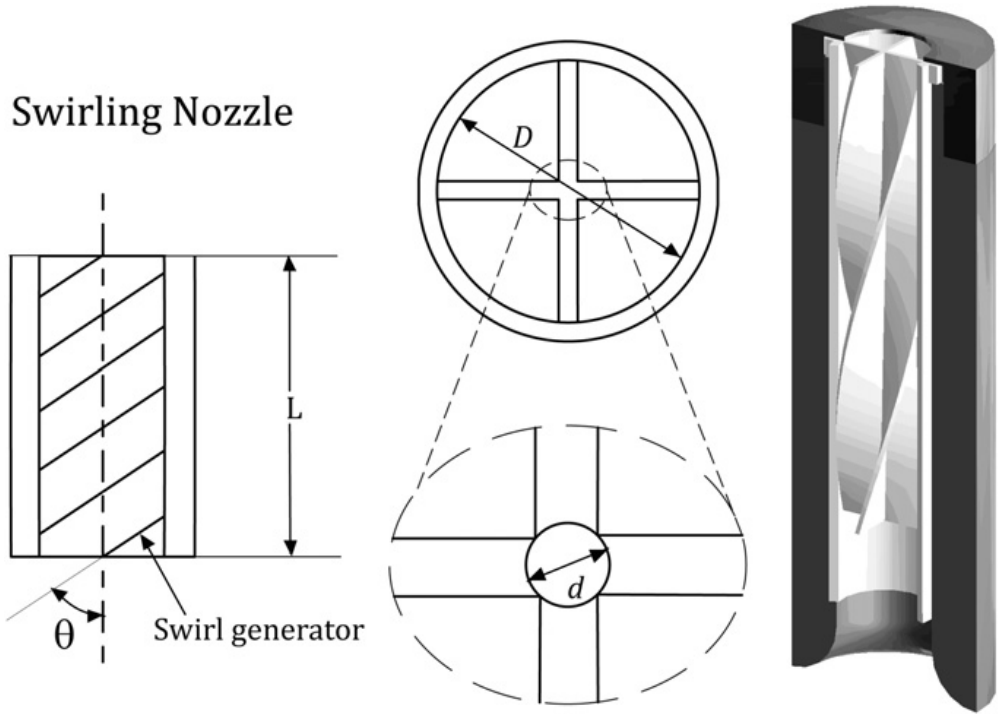

Fig. 4.2 Sketch of the swirling nozzle

4.1.2 Instrumentations and settings for the free jet experiments

The illumination is provided by a solid-state diode-pumped Nd:YLF laser. The laser beam (that has a diameter of 6 *mm*) is expanded with a diverging lens to a diameter of 8 *cm* and then is focused with a converging lens (located on the top of the tank) in order to have a conical illumination in the investigated volume; the diameter of the laser beam at the height of the nozzle is about 45 *mm* (Fig. 4.3a). The light scattered by the particles is recorded by a tomographic system composed of three CMOS cameras arranged along different azimuthal directions in a horizontal plane and forming a maximum angle of 90 degrees. Nikon objectives of 105 *mm* focal length are set with a numerical aperture f/#=22 to allow focused imaging of the illuminated particles. For the chosen illumination and imaging configuration the maximum particle image density (approximately 0.04 particles/pixel at the jet axis) is obtained only on the line of sight intersecting the jet axis and decreases towards the edges.

Table 4.1 Details of the experimental setup for free jets

Seeding material	Polyamide particles - diameter 56 μm
Concentration	0.48 $particles/mm^3$
Illumination	Quantronix Darwin-Duo Nd-YLF laser (2x 25 *mJ* @ 1000 *Hz*)
Recording device	3 Imager pro HS 4M cameras (2016 x 2016 pixels@ 1.3 *kHz*) 11 μm pixel pitch
Recording method	Continous mode/single exposure
Optical arrangement	Nikon lenses: focal length=105*mm*; f/#=22;
Field of view: (minimum)	2Dx5Dx2D
Acquisition frequency	100 *Hz*
Pulse separation	0.01 *s*
Rrecorded images	500

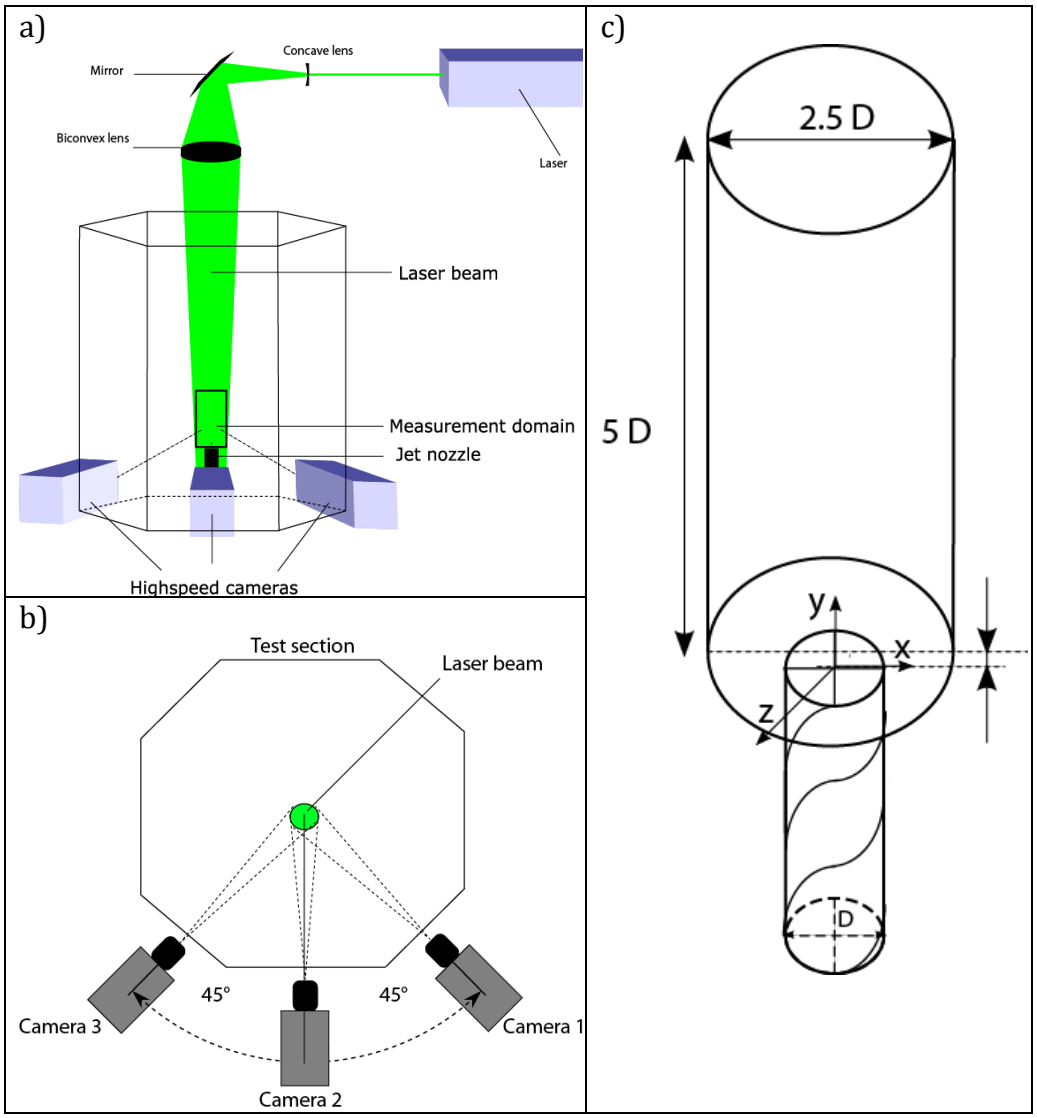

Fig. 4.3 Free jets tomographic PIV experiments: a) schematic of the system and b) detail of the illumination and recording system; c) measurement-domain.

The details of the experimental set up are summarized in Table 4.1. The choice of a conical domain of illumination results in the enhancement of the accuracy of the particle field, as the particle image density does not change with the angle of sight and decreases moving from the axis to the periphery of the jet. Moreover, the tomographic imaging system does not suffer from any increase in the intersection of lines-of-sight with the observation angle (Fig. 4.3b).

Sequences of images of tracer particles are recorded at 100 *Hz* resulting in high temporal resolution (imaged particle displacement of

approximately 10 pixel along the jet axis). The field of view has a digital resolution of 365 pixels/D and the measurement domain is on the nozzle exit and extends for 98 mm in the axial direction and 45 mm in the radial one (Fig. 4.3c). . It results that volumes of approximately 43x43x86 mm^3 are discretized with 800x800x1600 voxels applying a pixel to voxel ratio of 1. The resulting voxel pitch is 62.5 μm. The accuracy of the reconstructed object is improved by applying image pre-processing with sliding minimum subtraction over windows of 31x31 pixels. Three-dimensional particle field motion is computed using Volume Deformation Iterative Multigrid (VODIM) technique (the three-dimensional approach corresponding to the approach proposed for two-dimensional images by Scarano & Riethmuller, 2000) with a final interrogation volume of 51x51x51 voxels (0.14x0.14x0.14 D^3) with an overlap between adjacent interrogation boxes of 75%, leading to a vector pitch of 0.035 D. Velocity vector fields are obtained by averaging the cross-correlation map over three subsequent object-pairs (Violato and Scarano 2011), corresponding totally to a recording time of 0.03 seconds. Noisy fluctuations of the velocity vectors are reduced by applying a space-time regression, a second-order polynomial least-square fit over a kernel of 5 points in time and 5^3 points in space (Scarano & Poelma 2009) corresponding to a time length of 0.04 s and a volumetric domain of 0.14x0.14x0.14 D^3.

4.1.1 Instrumentations and settings for the impinging jet experiments

The illumination is provided by a solid-state diode-pumped Nd:YLF laser. The laser beam is expanded with two cylindrical lenses to obtain an illuminated volume with a thickness of 1.2 D and an area of 5x5 D^2 on the plate surface. The light scattered by the particles is recorded by a tomographic system composed of three CMOS cameras arranged on the top of the water tank and forming angles of 60 degrees, observing the illuminated region through the impinged plate. Nikon objectives of 105 mm focal length are set with a numerical aperture f/# = 22 to allow focused imaging of the illuminated particles. For the chosen illumination and imaging configuration the particle image density is approximately 0.045 $particles/pixel$. The details of the experimental set up are summarized in Table 4.2.

Sequences of images of tracer particles are recorded at 500 Hz resulting in high temporal resolution (imaged particle displacement of approximately 25 pixels along the jet axis and 5 pixels in the wall jet

region). The field of view has a digital resolution of 17.9 pixels/*mm* and the measurement domain is on the nozzle exit and extends for 80x80 mm^2 on the impinged wall and 24 *mm* in the axial direction (Fig. 4.4b). The accuracy of the reconstructed object is improved applying image pre-processing with sliding minimum subtraction over windows of 31x31 pixels.

Three-dimensional particle field motion is computed by Volume Deformation Iterative Multigrid (VODIM) technique (the three-dimensional approach corresponding to the approach proposed for two-dimensional images by Scarano & Riethmuller 2000) with a final interrogation volume of 48x48x48 voxels with an overlap between adjacent interrogation boxes of 75%, leading to a vector pitch of 0.0339 *D*. Noisy fluctuations of the velocity vectors are reduced by applying a space-time regression, a second-order polynomial least-square fit over a kernel of 5 points in time and 5^3 points in space (Scarano & Poelma 2009) corresponding to a time length of 0.008 s and a volumetric domain of 2.67x2.67x2.67 mm^3.

Table 4.2 Details of the experimental setup for impinging jets

Seeding material	polyamide particles - diameter 56 μm
Concentration	0.48 $particles/mm^3$
Illumination	Quantronix Darwin-Duo Nd-YLF laser (2x 25 mJ @ 1000 *Hz*)
Recording device	3 Imager pro HS 4Mpixels cameras (2016 x 2016 pixels@ 1.3 kHz) 11 μm pixel pitch
Recording method	continous mode/single exposure
Optical arrangement	Nikon lenses: focal length = 105*mm*; $f^{\#}$ = 22;
Field of view: (minimum)	4x4x1.2 D^3
Acquisition frequency	500 *Hz*
Pulse separation	0.002 *s*
Recorded images	500

a)

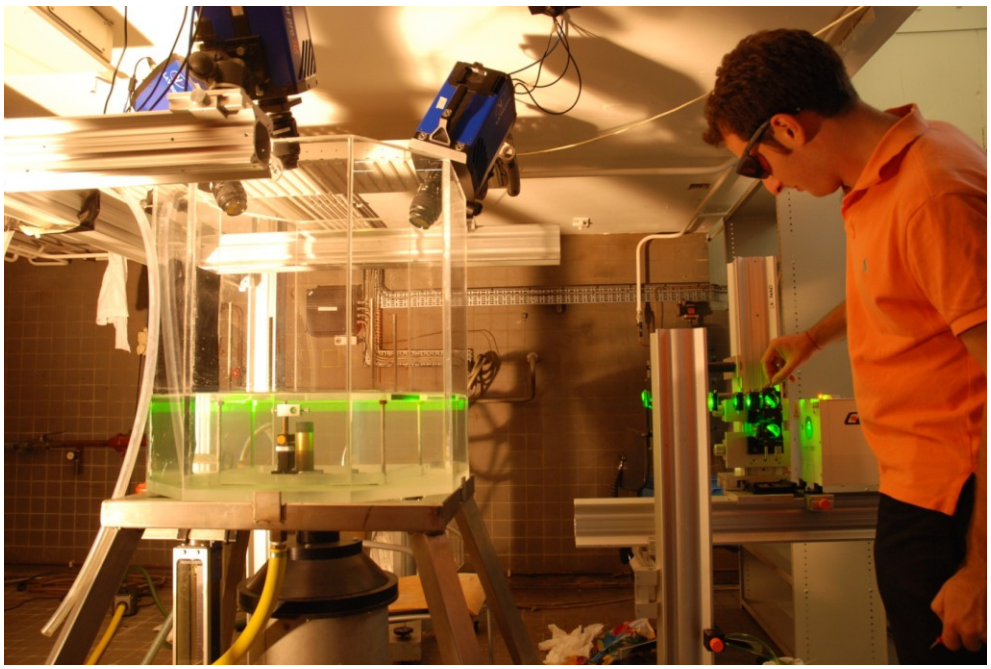

b)

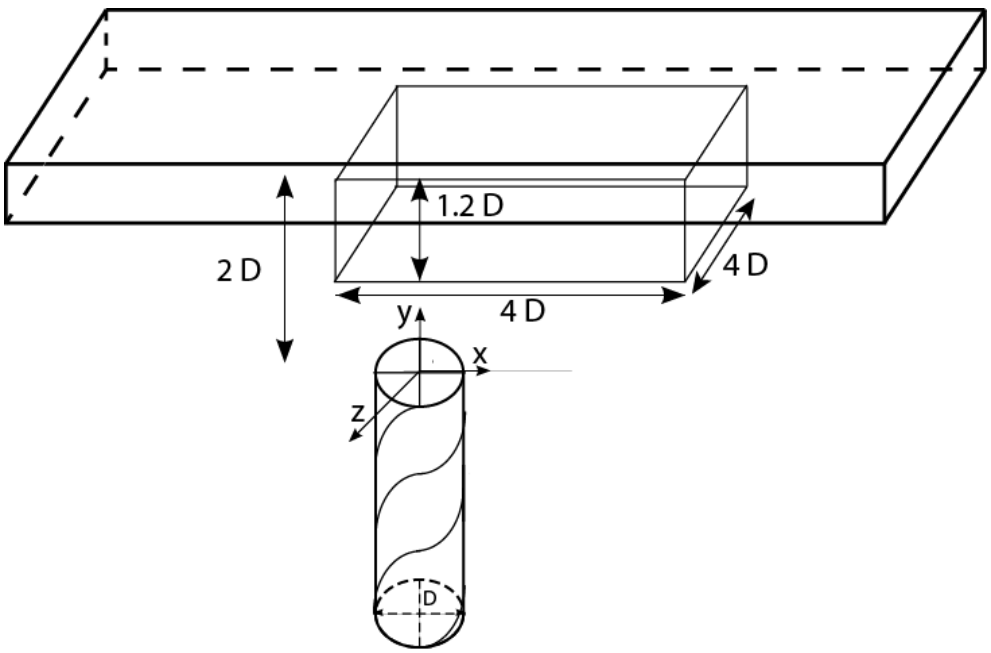

Fig. 4.4 Impinging jets tomographic PIV experiments: a) image of the system and b) measurement-domain

4.1.2 Uncertainty analysis

The measurement precision of three-dimensional three-component measurements can be performed by a-posteriori techniques based on physical criteria. The mass conservation principle can be used to ascertain the consistency of the measured velocity field as also proposed by Zhang, Tao & Katz. (1997). Although the flow divergence is not commonly a property of interest when dealing with incompressible vortex-dominated flows, its simple formulation makes it a suitable quantity to estimate the measurement errors on the spatial derivatives of the flow. For incompressible flows the velocity divergence must be zero everywhere:

$$\underline{\nabla} \cdot \underline{V} = \frac{\partial U}{\partial X} + \frac{\partial V}{\partial Y} + \frac{\partial W}{\partial Z} = 0 \qquad 4.2$$

The numerical evaluation of the divergence from experimental data, however, may be different from zero due to errors introduced by numerical truncation generated by the spatial discretization. Nevertheless the large overlap factor between neighbouring interrogation boxes ensures that truncation errors are negligible compared to the effect of the finite size of the interrogation. The evaluation of the standard deviation of $\underline{\nabla} \cdot \underline{V}$ over the entire measurement domain and during the whole observation time yields a statistical estimate of the tomographic PIV measurement error. The value of the standard deviation of $\underline{\nabla} \cdot \underline{V}$ can be considered as an upper bound for the error associated with the measurement of components of the velocity gradient tensor. This is because the measurement of the trace of the velocity gradient tensor (i.e. the velocity divergence) is usually less accurate than the non-diagonal terms. Normalizing the error by the typical values measured for the vorticity, a relative error of 3% is obtained.

4.2 Free swirling jets results

4.2.1 Baseline information and average flow field

In Fig. 4.5, are presented the averaged flow fields for all the studied swirling jet configurations: the jets are visualized with iso-surfaces of V = 0.5 and velocity contours with vector arrows in the planes near the nozzle exit (at a distance of 0.1 diameters from the nozzle), at 1.5 diameters and at 3 diameters from the nozzle exit. Due to the high computational cost of tomographic reconstruction and volume

correlation and since the principal scope of this experimental campaign is the study of vortex dynamics, the averaging process is done on time resolved fields over only 190 filtered flow fields. This amount of images corresponds to only 6 periods of precession of the vortex core (which is the slowest phenomenon in the flow field); despite of that these averaged fields allow to well visualize and qualitatively illustrate all the most relevant aspects of the average flow field.

As expected, it is evident that the flow field is not axis-symmetric because in all the cases actually four jets are issued from the nozzle due to the presence of the helical swirl generator composed by four channels. The four jests develop in stream-wise direction and two shear layers are present: one in the centre between the four jets and one in the external part of the jet. The development of these shear layers is crucially influenced, of course, by the swirl number.

If the plane at the nozzle exit is considered the four jets exhibit an axial velocity distribution that is critically changed by the swirl: at $S = 0$ the maximum axial velocity is in the centre of each of the four channels with a Poiseuille distribution; the four jets behave as jets issuing from a pipe. Differently from what found by Vaniershot and Van den Bulck (2008), the concentric central tube of the jet (the centre of the insert) does not seem to act as a bluff body to the flow, creating a central recirculation zone behind it; in their experiment the insert is much larger thus generating a stronger effect downstream.

When the swirl is introduced, the maximum axial velocity at the exit is not any longer in the centre of each of the four channels. The maximum of axial velocity is displaced outwards, the velocity distribution does not have a Poiseuille shape and the maximum of velocity is moved downstream if the swirl motion in the XZ plane is considered. The swirling jets broaden downstream and if a plane XZ is considered the swirling jets have a swastika shape up to a distance of three diameters from the nozzle.

When the swirl in sufficiently high, the recirculation zone in the centre of the jet develops. It is firstly seen at $S = 0.6$ at $Y \approx 1.2$; then the recirculation region moves upstream, up to the nozzle exit, in the jet at $S = 0.8$.

In agreement with Park and Shin (1993) the effect of swirl on the spreading angle of the jet is quite noticeable and the swirl has substantial influence on the entrainment rate. If the plane at a distance of 1.5 diameters from the nozzle is considered, it is evident that the jet (identified with the iso-surface of $V = 0.5$) is broadened way more with

increasing the swirl number and that the maximum axial velocity is way lower due to a higher entrainment.

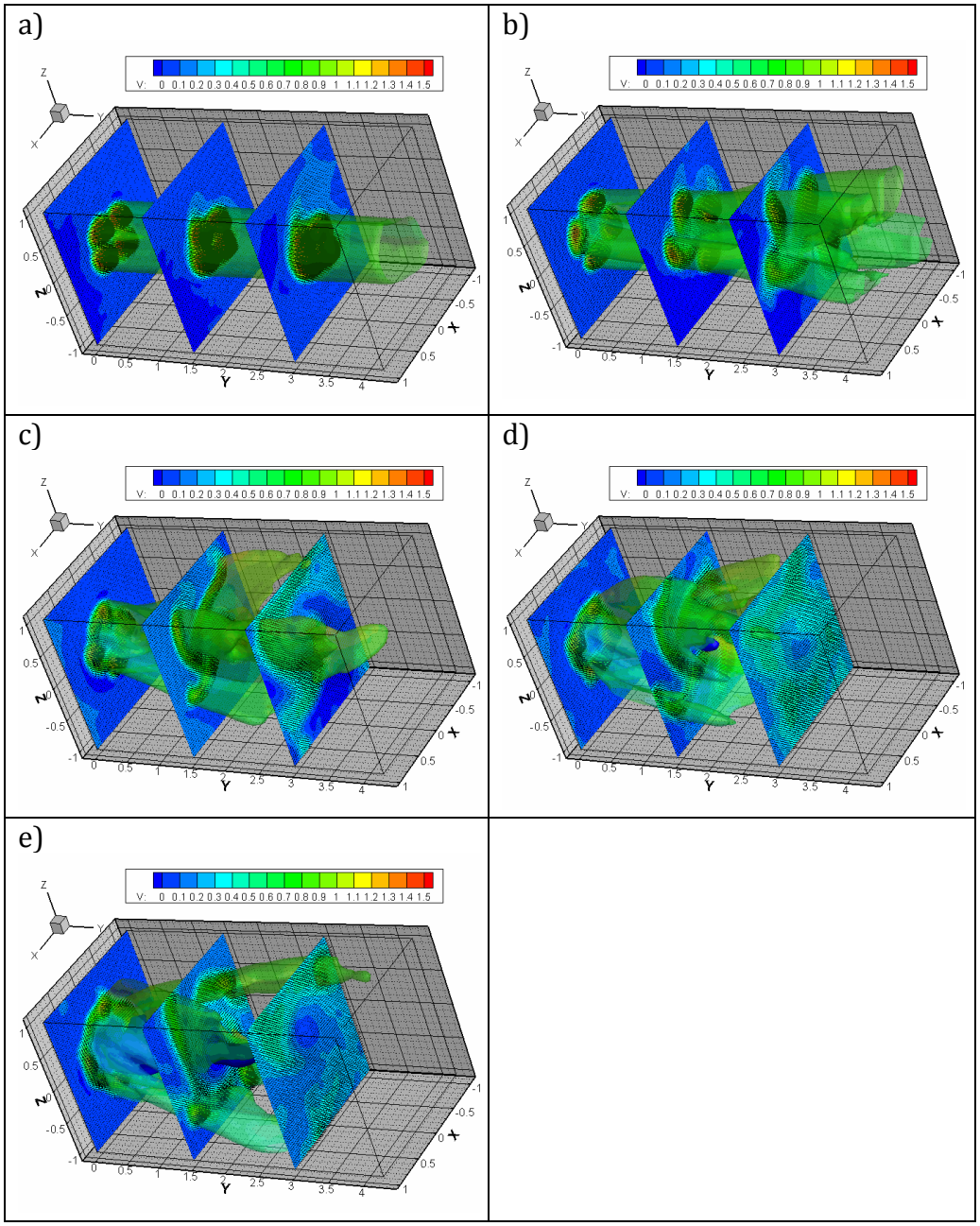

Fig. 4.5 Averaged flow fields (In transflucent Isosurface of *V* = 0.5 – In blue Isosurface of *V* = -0.1 – Contour of *V* and vector arrows on the planes at *Y* = 0.1, *Y* = 1.5 and *Y* = 3): a) *S* = 0; b) *S* = 0.2; c) *S* = 0.4; d) *S* = 0.6; e) *S* = 0.8;

4.2.2 Vortex topology

In the following, some instantaneous flow fields are presented: contours of axial velocity with vector arrows are presented at $Y = 0.1$, $Y = 1.5$ and $Y = 3$, the iso-surface of $V = 0.5$ is shown in translucent and the iso-surface of $Q = 1.5$ is shown in blue for vortex identification. The jet with S=0, presented in Fig. 4.6, is characterized by a weak broadening; in the shear layer Kelvin-Helmholtz instabilities are produced but they do not amplify and no vortices are visualized (unlike what shown for circular jet in similar conditions, e.g. Danaila et al. 1997). This phenomenon can be explained considering the multichannel jet as the ensemble of four distinct jets; the characteristic length for the axial shear layer is half the diameter and the effective Reynolds number for the single jet can be considered being 500.

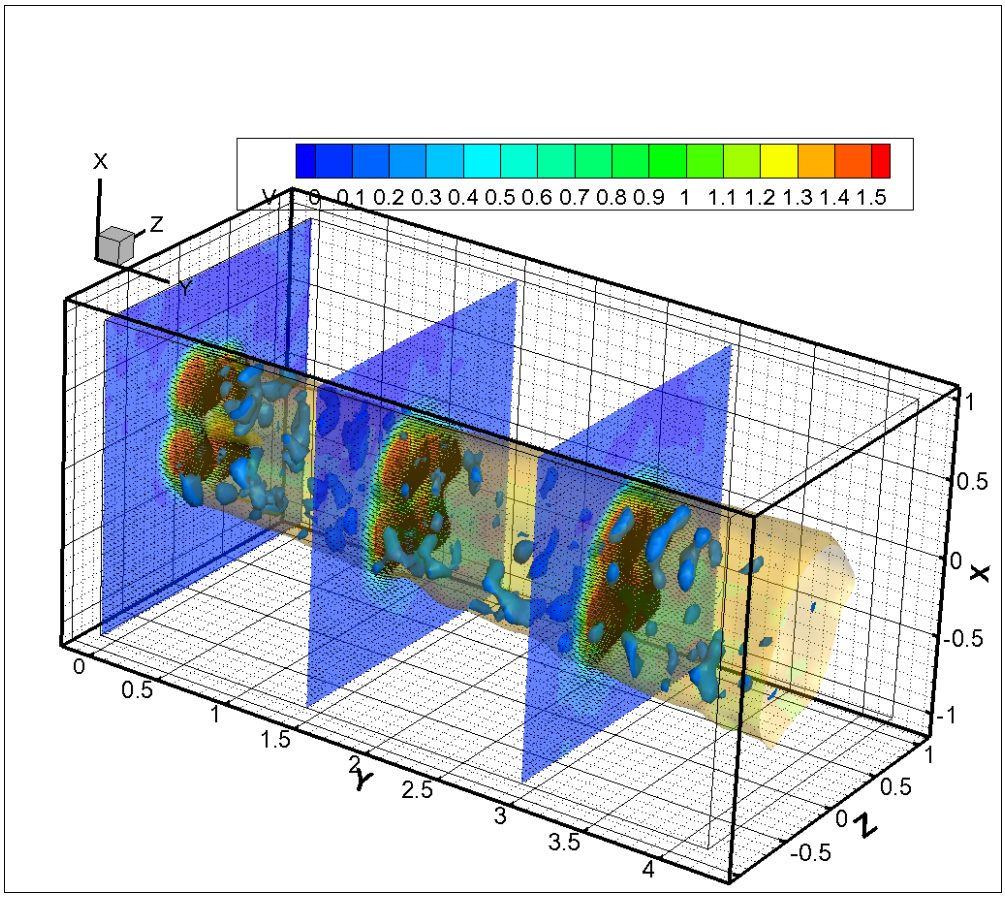

Fig. 4.6 S=0, instantaneous flow fields: contours of axial velocity with vector arrows at $Y = 0.1$, $Y = 1.5$ and $Y = 3$, iso-surface of $V = 0.5$ in translucent and iso-sorface of Q= 1.5 in blue.

In Fig. 4.7 the instantaneous flow field of the jet with S=0.2 is presented: the introduction of swirl has a destabilizing effect of the axial shear layer and rib-like vortices of Kelvin Helmholtz type develop. The main coherent structures are the rib-like vortices while the vortex associated to the swirl is very weak. The presence of rib-like vortices instead of the helical vortices is clearly due to the presence of the insert as well as the helical coherent structures described by Liang and Maxworthy (2005) in their work on swirling jets at Re = 1,000 are due to the swirling device used. In this experiment there is an external shear layer and another shear layer between the four jets issuing from the nozzle; this deals with a more complex vortex topology. The rib-like vortices start developing after the nozzle exit, then undergo pairing near Y = 3 where the vortex size appears to be bigger and it is possible to see the development of azimuthal instabilities similar to Widnall vortices (Widnall et al. 1974).

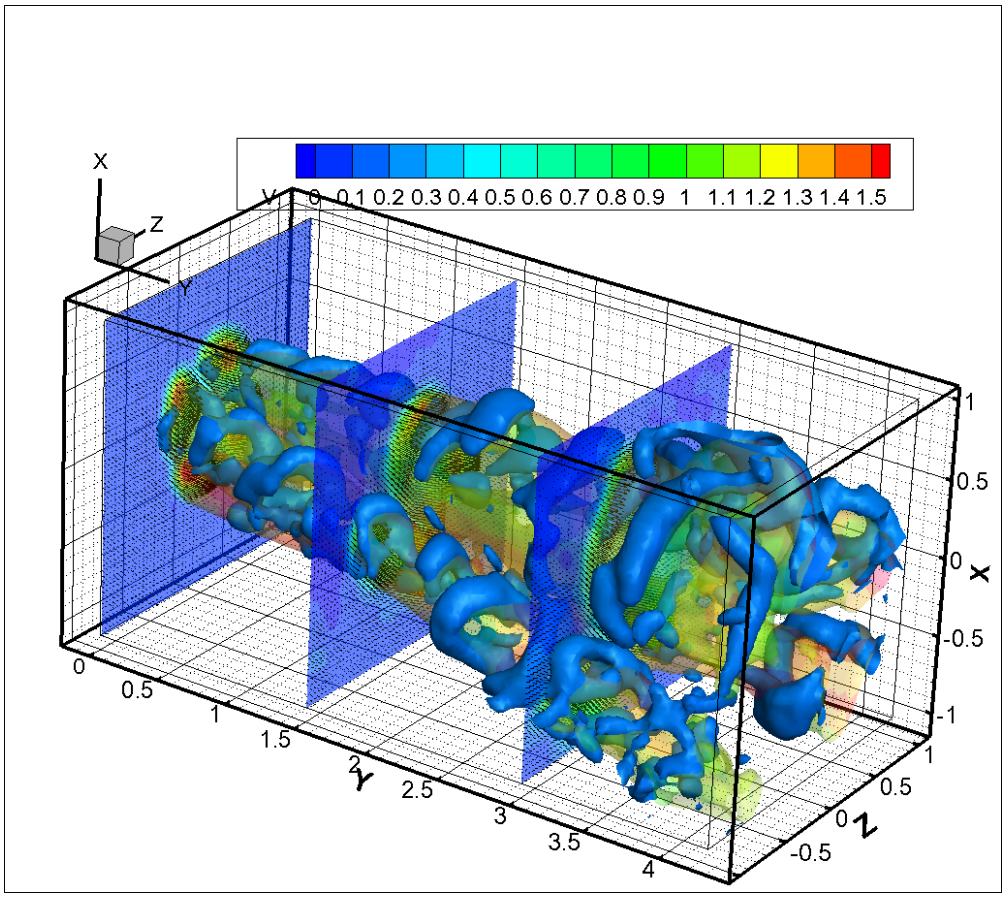

Fig. 4.7 S=0.2, instantaneous flow fields: contours of axial velocity with vector arrows at Y = 0.1, Y = 1.5 and Y = 3, iso-surface of V = 0.5 in translucent and iso-sorface of Q= 1.5 in blue.

The case with S = 0.4 is presented in Fig. 4.8. The central vortex core is now evident in the centre of the jet and it has the same importance of the big Kelvin-Helmholtz structures present in the shear layer. This visualization shows the presence of inner and outer vortices in agreement with Cala et al. (2006); indeed from the inspection of the data it appears clear as those vortices are (inner and outer together) the same helical vortex that surrounds the jet. As shown from the averaged flow field, the shape of the XZ section of the jet is that of a swastika and this causes the helical vortices to have their rib-like shape

In this case, in agreement with literature (Panda and McLaughlin, 1994), the vortex pairing is suppressed contrary to what seen at lower swirl axial shear layer in this case. As a consequence the stream-wise oriented vortices that develop after vortex pairing are also suppressed.

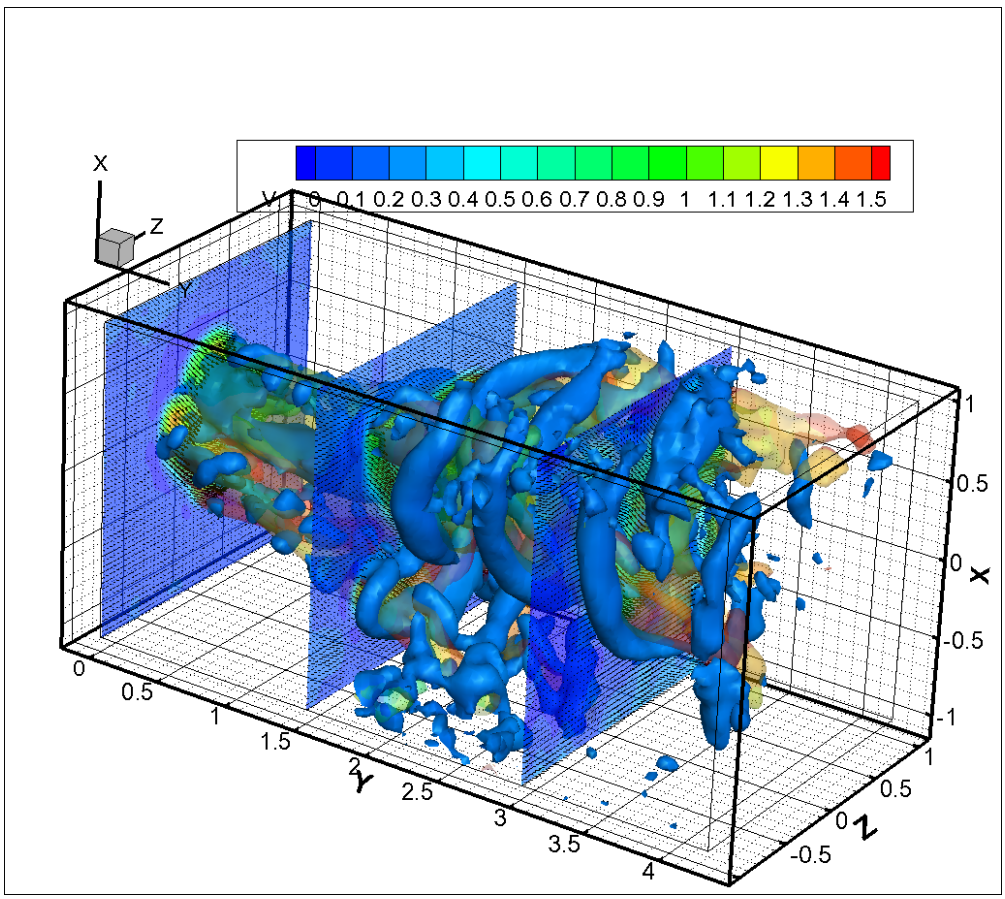

Fig. 4.8 S=0.4, instantaneous flow fields: contours of axial velocity with vector arrows at Y = 0.1, Y = 1.5 and Y = 3, iso-surface of V = 0.5 in translucent and iso-surface of Q= 1.5 in blue.

The case with S = 0.6 is presented in Fig. 4.9. Here the vortex topology is very complex thus, for the sake of clarity, only the iso-surfaces of Q = 1.5 are visualized together with an iso-surface of V = -0.1 in attempt to show the region of vortex breakdown. Helical vortices develop at the exit of the jet. Near Y = 1 the central vortex core break into two main vortices that surround the recirculation zone. Indeed, the central vortex core, after the breakdown, precesses around the recirculation region and probably interacts with the vortices generated in the external shear layer. It is not possible to investigate the behavior of the rib-like vortices after Y = 3 because at this distance from the nozzle exit, the outer part of the jet is outside of the measurement domain; despite of that it appears that the topology of vortices in the shear layer is analogous to that seen at S = 0.4; the vortex pairing is suppressed and also stream-wise vortices are not present.

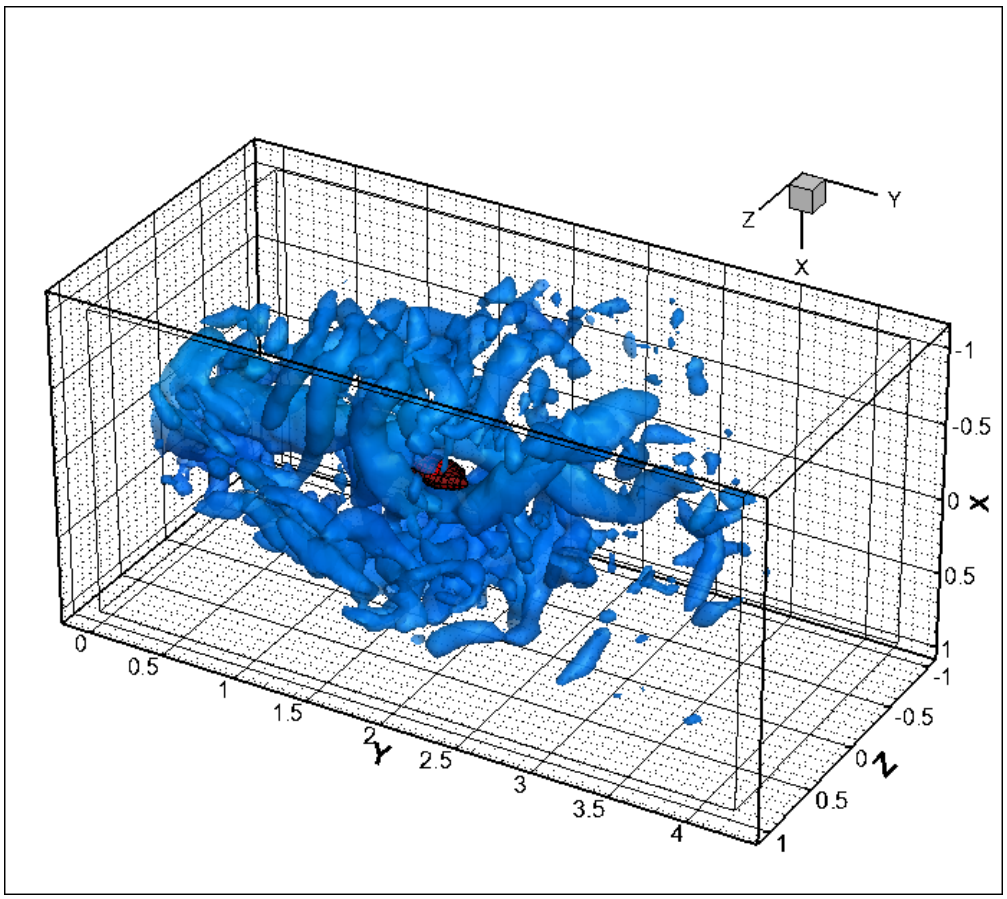

Fig. 4.9 S=0.6, instantaneous flow fields: iso-surface of V = -0.1 in red and iso-sorface of Q= 1.5 in blue.

At S=0.8 (see Fig. 4.10) the phenomenon of vortex breakdown dominates the flow field: the recirculation region starts at the nozzle exit and ends at a distance of about 2.5 diameters from the nozzle exit. The broken vortex core surrounds the recirculation region and touches the vortices generated in the outer shear layer. As in the case with S = 0.6, it is not possible to investigate the behaviour of the rib-like vortices after Y = 3 because at this distance from the nozzle exit, the outer part of the jet is outside of the measurement domain; despite of that it appears that the topology of vortices in the shear layer is analogous to that seen at S = 0.4; the vortex pairing is suppressed and also stream-wise vortices are not present.

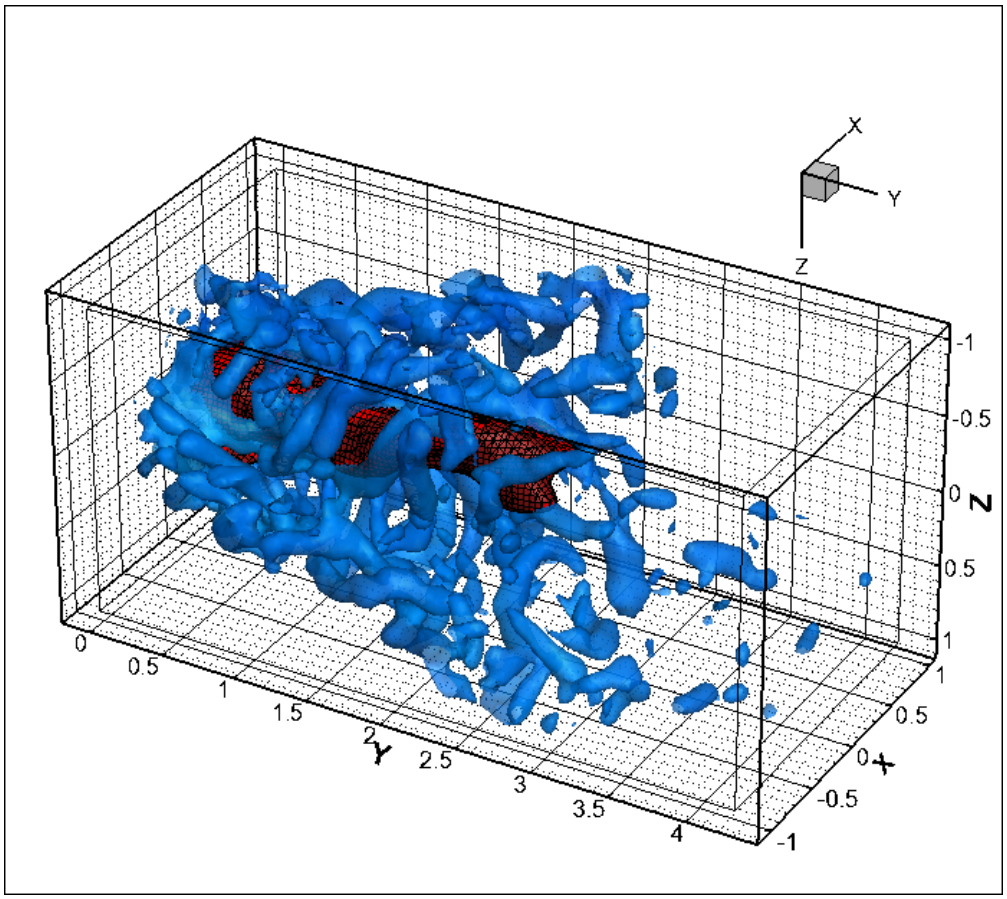

Fig. 4.10 S=0.8, instantaneous flow fields: iso-surface of V = -0.1 in red and iso-sorface of Q= 1.5 in blue.

4.2.3 Vortex pairing at low swirl

The formation of vortex ring structures in the near region of circular jets is well known from several studies conducted over a wide range of Reynolds number from 10^3 to 10^5 (Bradshaw et al., 1963; Crow and Champagne, 1971; Winant and Browand, 1974; Yule, 1978). In the present experiment, the shedding of rib-like helical vortices is observed to occur immediately at the nozzle exit at Strouhal number $St=fD/V_j$ of 1.72, where f is the shedding frequency, V_j is the jet exit velocity and D is nozzle diameter. Actually the vortices displayed in the present experiments are not circular but helical vortices that surround the jet and near the jet exit they appear to be spaced of 0.45 nozzle diameters. They work as ring vortices in circular jet: the core induces an outward flow at its leading edge and inward at the trailing one, which increases as the vortex grows and is convected downstream.

In the range between 2.5 and 3.5 diameters, the vortices undergo pairing (Crow and Champagne, 1971; Winant and Browand, 1974) with a Strouhal number of St=0,86 a half of that of shedding.

In circular jet the pairing mechanism is well assessed and clear: the flow induced by the preceding vortex produces axial and inward accelerations in the jet core between the vortex and the following one. As a result, the pursuing vortex is stretched along the axis increasing in convective velocity and decreasing in diameter. Contrarily, due to the outward motion induced by the follower, the preceding one stretches positively while widening in diameter and its convection speed decreases. As a consequence of the convective velocity difference, the distance between the two vortices gradually reduces and the pursuing vortex pairs with the preceding one.

In the current experiment the strength of the vortices is not azimuthally isotropous thus pairing happens in a different way with respect to a circular jet. Fig. 4.11 illustrates a temporal sequence of the flow field with snapshots separated by a normalized time step equal to 1. The iso-surfaces of normalized Q = 1.5 identifies vortices which are labelled with “1”, “2”, “3”, “4” and “5”. The iso-surfaces of Q are flooded by non-dimensional vortex stretching. The vortex stretching corresponds to projection in the vortex direction of the term of the vorticity equation $(\underline{\omega}\cdot\underline{\nabla})\underline{V}$ (see e.g. Majda & Bertozzi 2002) that describes the stretching or tilting of vorticity due to the velocity gradients.

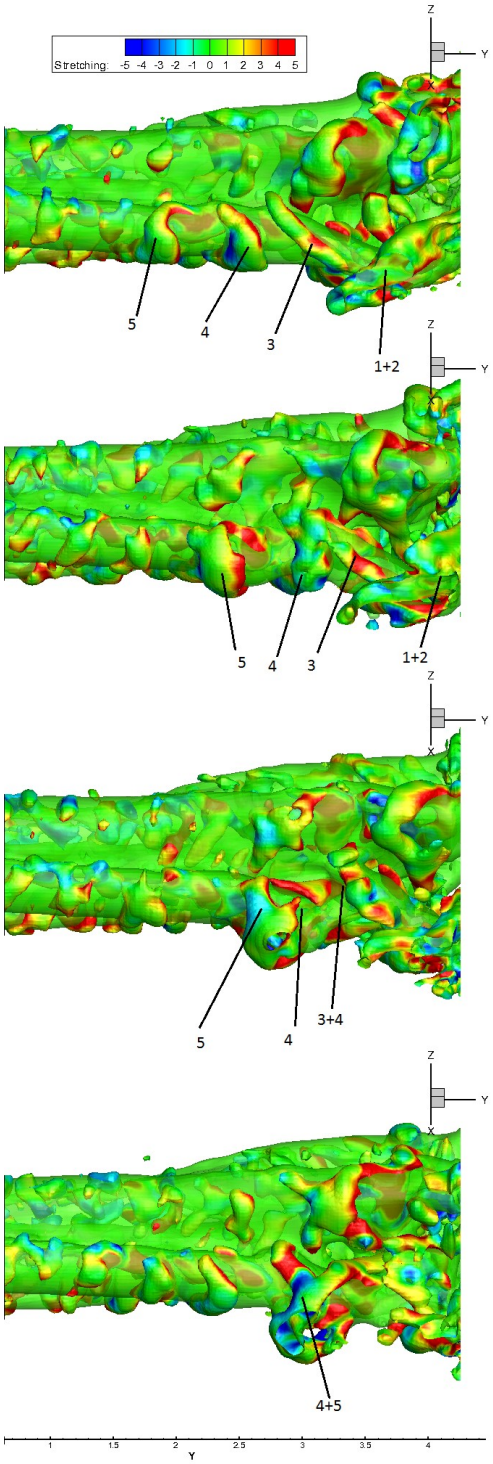

Fig. 4.11 Vortex pairing in the S = 0.2 jet. In translucent, iso-surface of V = 0.5; contoured by vortex stretching: vortex visualization with iso-surface of Q=1.5.

As shown in Fig. 4.11, the preceding vortex is subject to positive stretching (in red) and the following to negative stretching (in blue). The vortices undergo pairing alternatively in the inner and in the outer part of the jet: e.g. the vortex “4” undergo pairing in the inner part of the jet with the vortex “3” and then in the outer part of the jet with the vortex “5”. This cause a different mechanism of formation and growth of azimuthal instabilities compared to the case of circular jets(Widnall et al. 1974; Yule, 1978; Liepmann Gharib 1992): Widnall vortices are not present in the swirling jet flow field and the stream-wise structures visualized are the helical vortices tilted in the stream-wise direction during the pairing.

4.2.4 Vortex breakdown and precessing vortex core

As already stated, in the present experiments the breakdown and the precession of the jet vortex core are found at S = 0.6 and S =0.8. In Fig. 4.12 a time sequence of flow fields separated by a normalized time step equal to 1.3 are shown presenting iso-sourfaces of Q= 3.5 in blue, vector arrows at Z = 0 and, in red, evidenced with a black grid surrounding it, also the recirculation zone identified with an iso-surface of V = -0.1. The current experiment allows addressing the importance of the interaction between the vortex core and the vortices in the axial shear layer in the phenomena of vortex breakdown and precessing vortex core. Near Y = 1 the vortex core breaks in two helical vortices and the recirculation zone develops in the centre of the two vortices obtained from the breakdown of the vortex core.

The two vortices generated by the breakdown of the vortex core surround the recirculation region forming, each of them, a helix around it. Due to the breakdown of the vortex core and due to the formation of the recirculation region on the jet axis, the two helical vortices are placed outwards from the centre of the jet; thus they interact with the rib-like vortices generated in the shear layer. The position of these two vortices is unsteady because they do a precession around the recirculation region.

In particular, the helix seems to follow the convection of the rib-like vortices in the shear layer, thus causing the precession of the vortex core. The mechanism reminds a corkscrew: the helix is convected downstream and the vortex core is in rotation on its axis.

The dynamics of the rib-like vortices are influenced by the precessing vortex core as well as they influence it. The velocity field generated by the PVC contrasts the effect of the velocity fields generated by the rib-

like vortices. The acceleration and the diameter reduction of the follower vortex as well as the deceleration and the diameter increment of the preceding vortex (typical of the pairing mechanism) disappear and the pairing mechanism is suppressed.

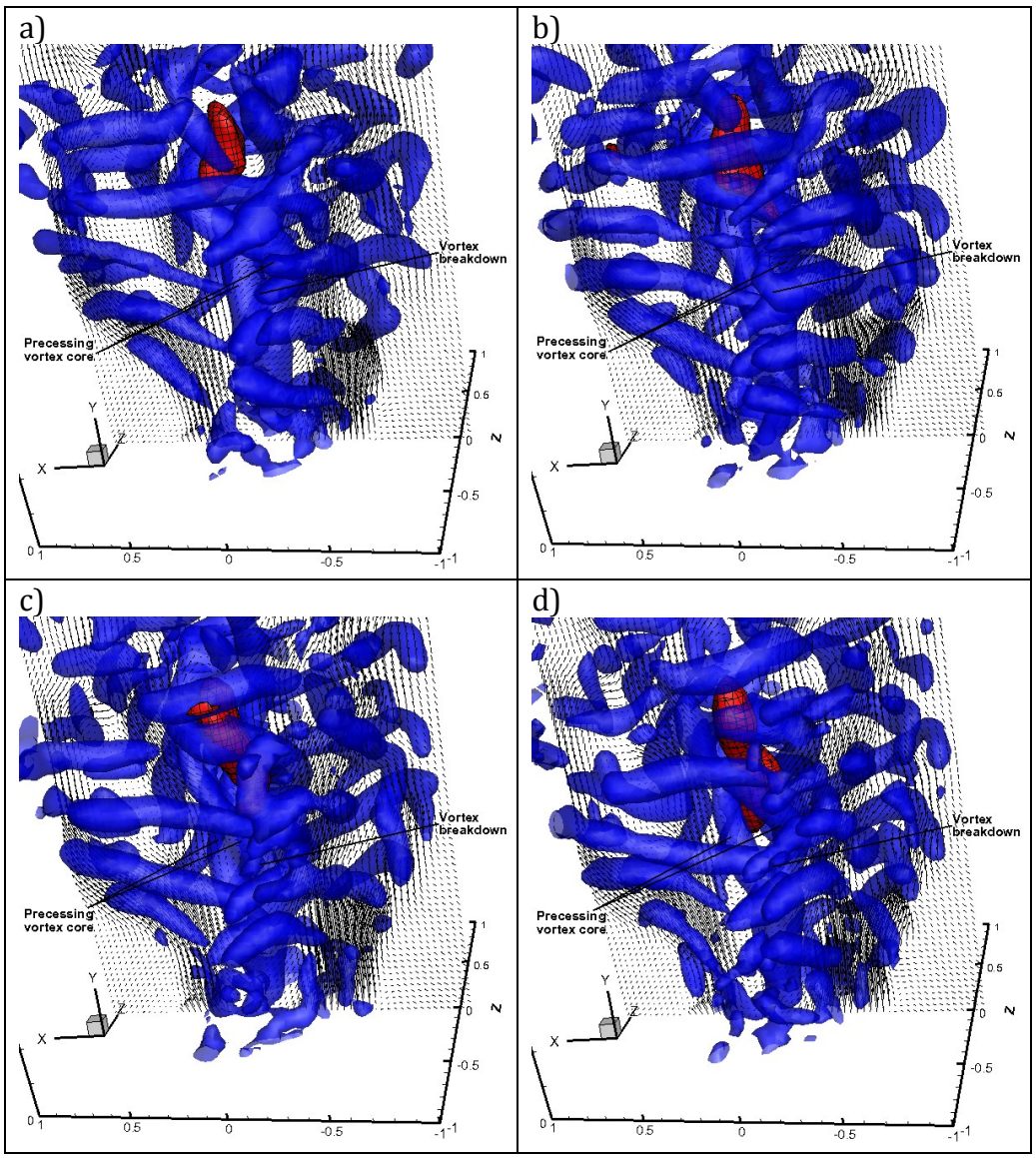

Fig. 4.12 Vortex breakdown and precessing vortex core in the S = 0.6 jet

4.3 Swirling impinging jets results

4.3.1 Circular impinging jet

As already said in the introduction, the flow field in the circular jet is characterized by the presence of the ring vortices. This is clear from the quantitative visualization of the flow field in Fig. 4.13 where are presented the contour of axial velocity on the plane at X= 0, the contour of velocity on the plate at 0.04 diameters from the plate, the iso-sourface of Q = 1 plotted in translucent and some streamlines allowing to analyze vortices behaviour and lifetime.

The streamlines of flow coming from the environment and joining the jet evidence the role of the ring vortices in entraining flow from the ambient and accelerating the fluid on the wall in a pulsatile motion.

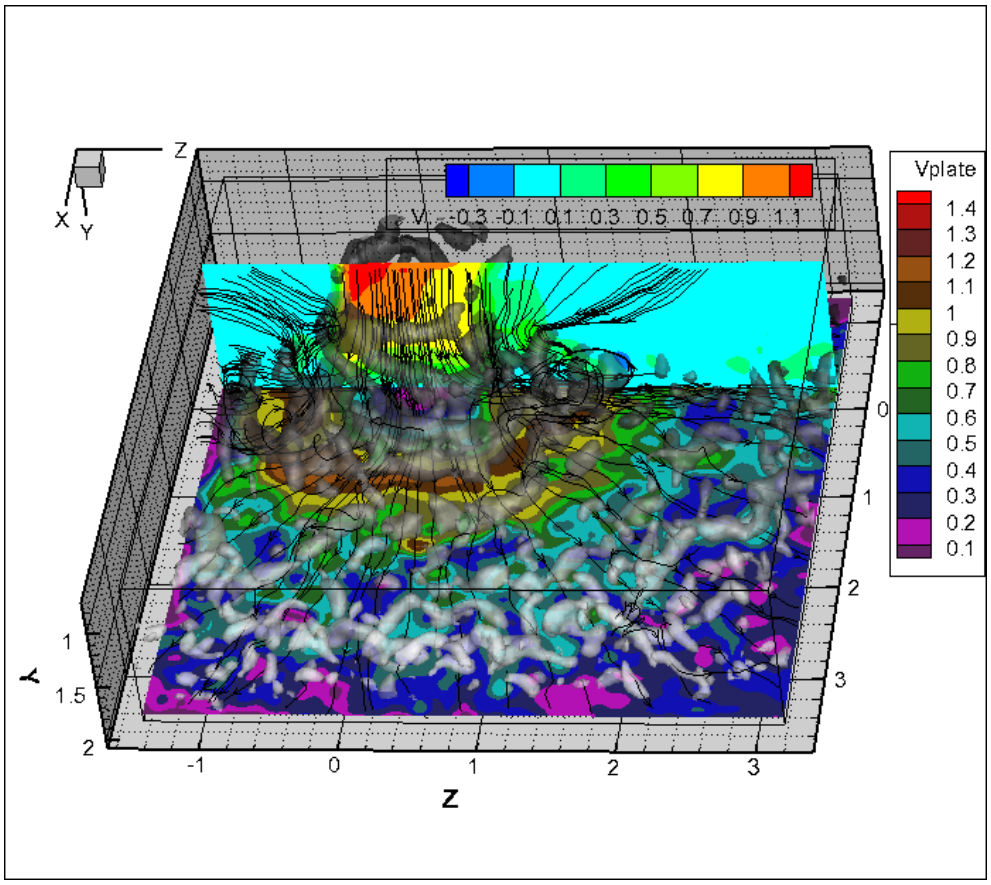

Fig. 4.13 Instantaneous flow field in a circular impinging jet: contour of axial velocity on the plane at X= 0, contour of velocity on the plate at 0.04 diameters from the plate, iso-sourface of Q = 1 in translucent and streamlines

Ring vortices are shedded with a Strouhal number equal to 0.79 then are convected towards the wall. Once arrived on the wall ring vortices stretch until they break in smaller coherent structures at a distance of about 1.5 diameters from the centre of impingement. Compared to the free jets, the pairing mechanism is not seen: when a vortex approaches the wall, its convection speed decreases and the vortex is stretched on the plate; at the same time the following vortex arrives very close to the preceding one but is not accelerated enough to allow the pairing. There is a kind of interaction between the ring vortices but it is not characterized by azimuthal symmetry. The flow field, in fact, is characterized also by the formation of azimuthal instabilities (seen also by Meola et al. 1995): the flow field generated by those vortices is presented in Fig. 4.14 with a plane at Y = 1.3 on which is plotted a contour of axial velocity with in-plane velocity vectors. The Widnall vortices develop in couples in the jet shear layer, and are able to entrain a huge quantity of external fluid in the jet. From the present visualization these azimuthal vortices seem to play a very important role also in the downstream flow field: in particular in the development of the turbulent boundary layer in the wall jet region.

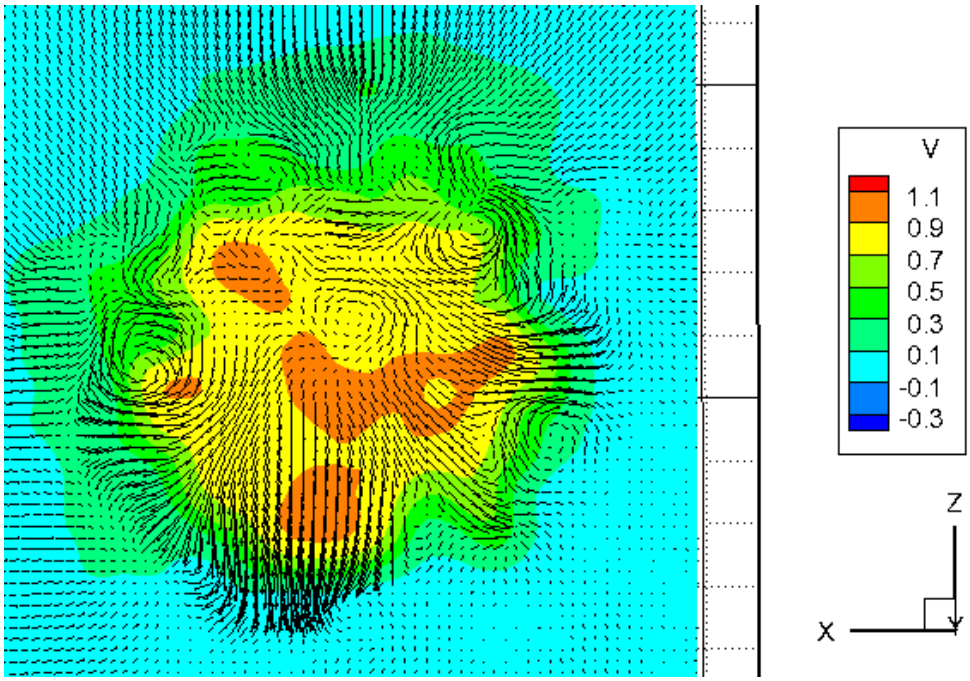

Fig. 4.14 Azimuthal vortices in a circular impinging jet

In fact as shown in Fig. 4.15 the vortical structure composed by the Kelvin-Helmholtz vortices and the Widnall vortices, break up and form hairpin-like vortices typical of a turbulent boundary layer when the wall jet region develops (about two diameters away from the centre of the impingement region).

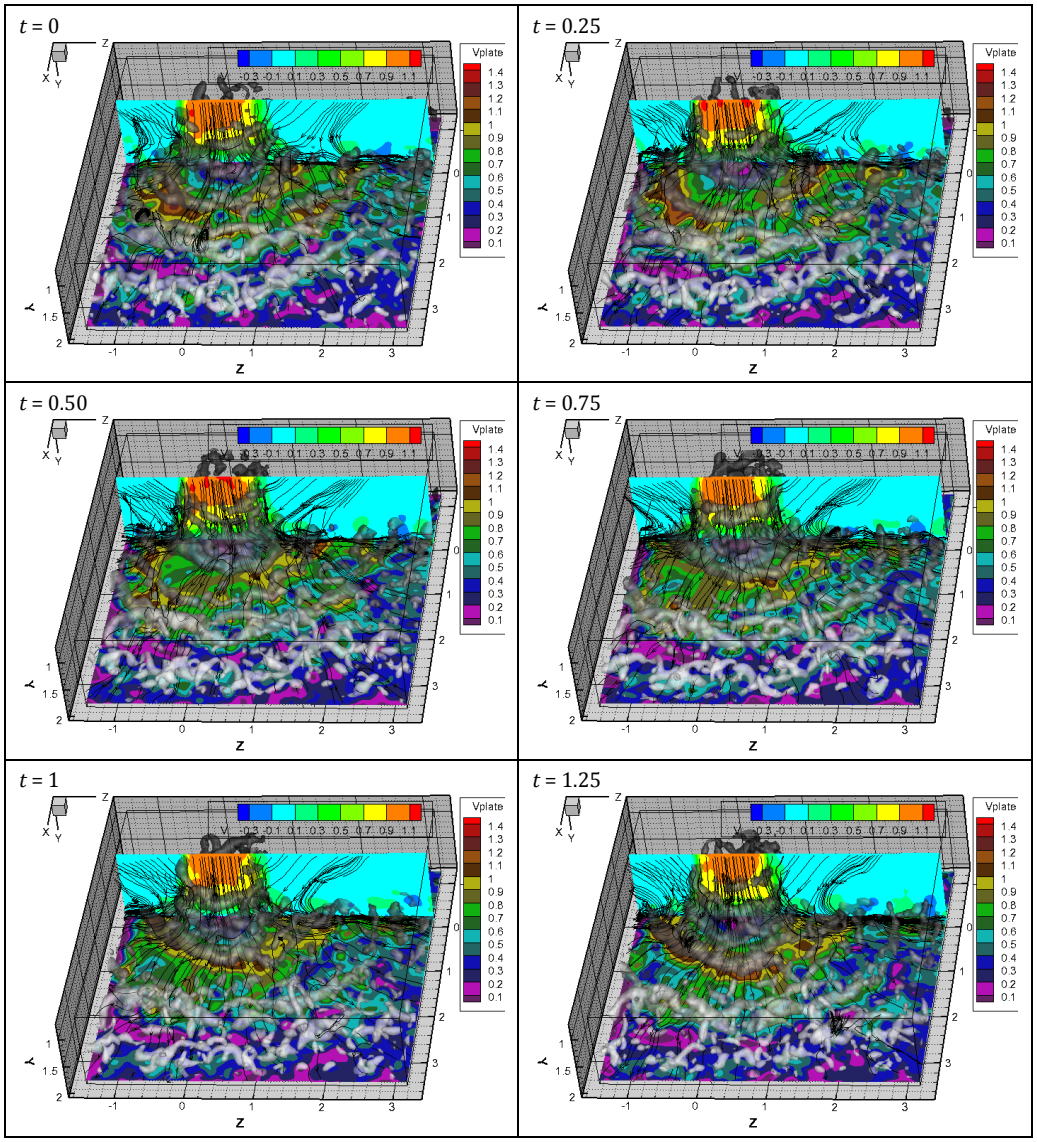

Fig. 4.15 Time sequence of flow field in a circular impinging jet with time interval equal to 0.25 : contour of axial velocity on the plane at *X*= 0, contour of velocity on the plate at 0.04 diameters from the plate, iso-sourface of *Q* = 1 in translucent and streamlines

This aspect is confirmed by the flow statistics(Fig. 4.16): it is evident the increase in turbulent kinetic energy in correspondence of the position where the harpin-like vortices are generated. This position coincides with the position where in literature is found the second maximum in the Nusselt number profile (see for comparison Fig. 5.2). The first maximum of Nusselt number profile is instead found in correspondence of the region of maximum velocity on the plate (in white in Fig. 4.16).

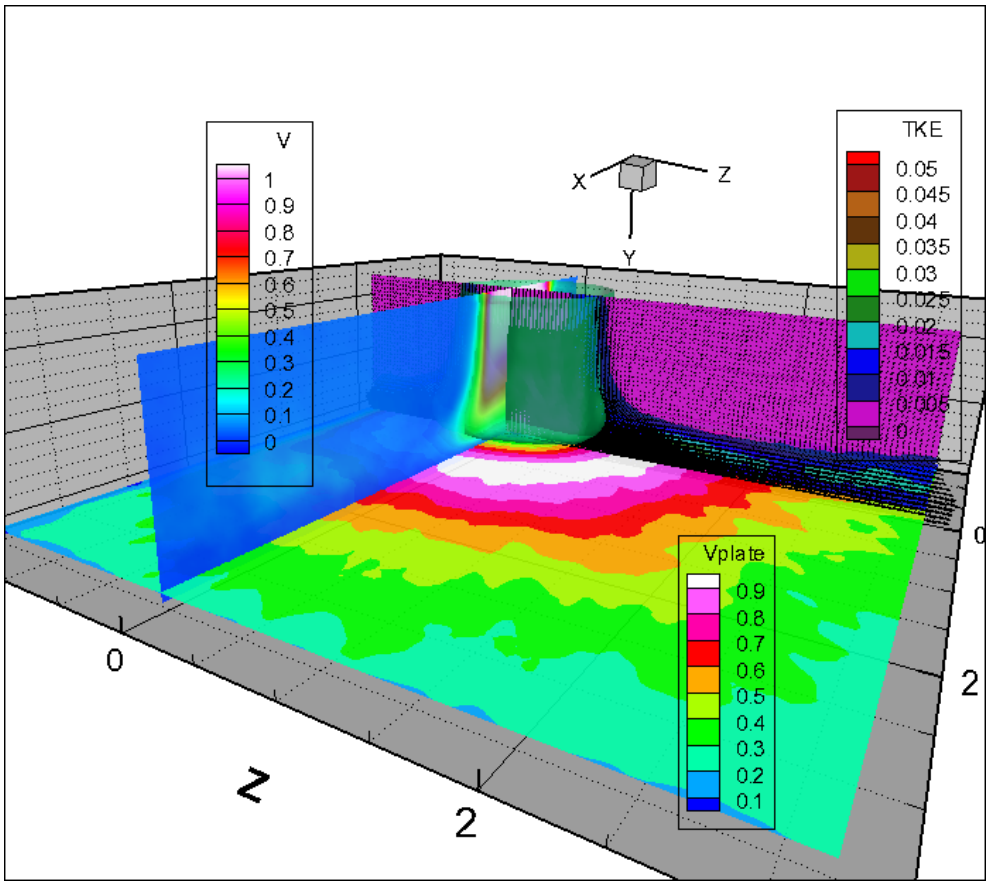

Fig. 4.16 Flow field statistics in a circular impinging jet

4.3.2 Swirling impinging jets

Instantaneous and averaged flow fields of swirling impinging jets are presented in Fig. 4.17 and Fig. 4.18, respectively.

The four jets issuing from the pipe do not merge before impinging the plate and produce four separate stagnation region for all the tested conditions.

The instantaneous flow fields are visualized by means of streamlines, iso-surfaces of $Q = 1$ in translucent, contour of V on the plane at $Z = 0$ and contour of V_{plate} on the olane at $0.04\ D$ from the impinged wall. Due to the introduction of the insert, the ring vortices are not visualized. Turbulence is organized in smaller coherent structures with respect to the case of the circular jet as shown in Fig. 4.15. The swirling jets are characterized both in their external and internal shear layer by small vortices that are the rib vortices visualized in the free swirling jets. Those small coherent structures cause a deeper penetration of turbulence in the core of the jet in agreement with what shown by Kataoka et al. (1987) and by Violato et al. (2011) after the break up of the vortex rings. Part of the rib-like vortices are elongated in the axial direction, thus producing high entrainment, especially at high swirl.

On the wall, the hairpin vortices develop already near the impingement and are convected in the wall jet. The turbulence level on the wall is quite homogeneous and outer maxima of heat transfer as in the case of the circular jet are not expected.

As expected from the free jet results, with the increase of swirl, the jet broadens in size, a recirculation region develops and arrival speed decreases. This is particularly evident from Fig. 4.18 where the dramatic reduction of the maximum V_{plate} with the increase of the swirl number is evident.

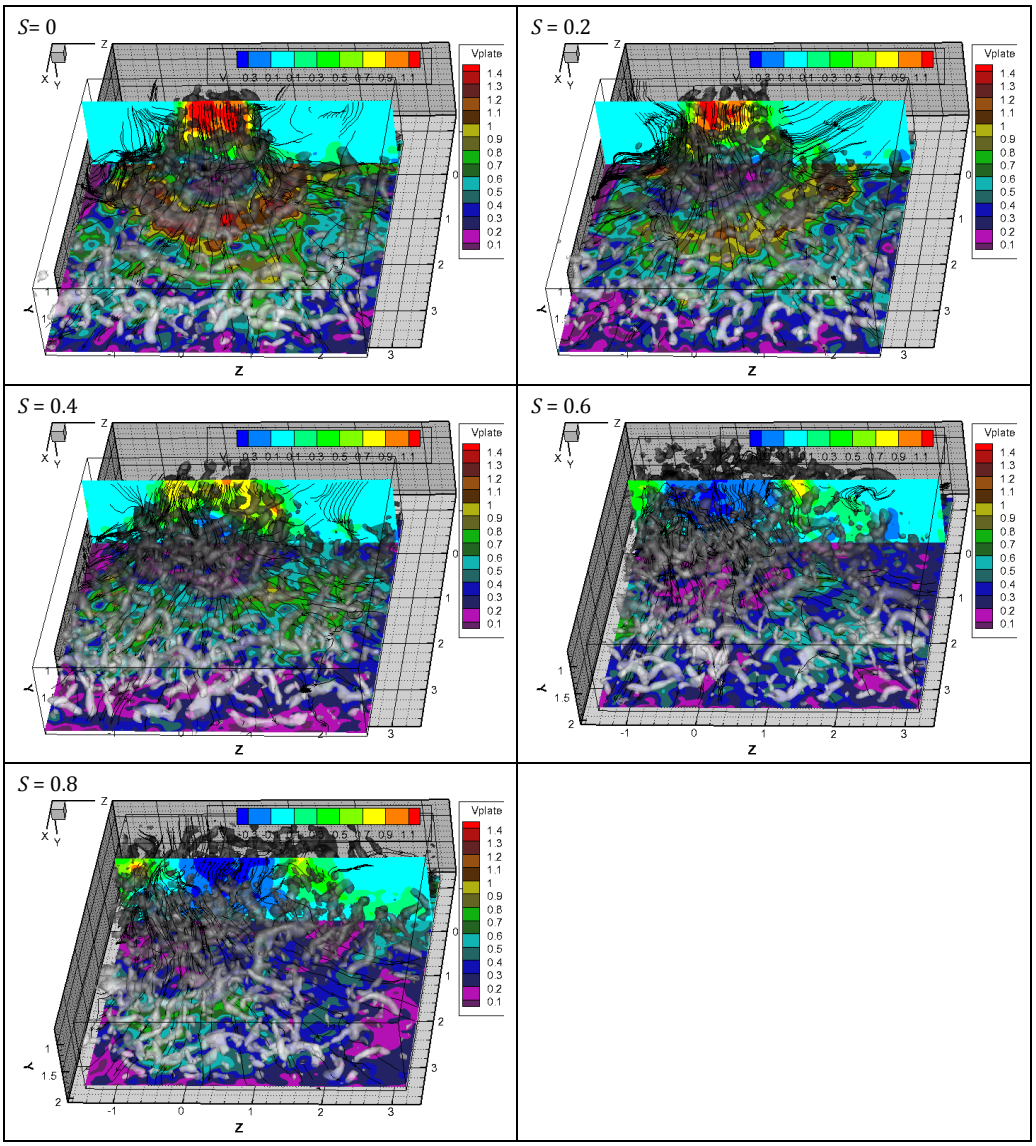

Fig. 4.17 Instantaneous flow fields in swirling impinging jets: contour of axial velocity on the plane at X= 0, contour of velocity on the plane at 0.04 diameters from the plate, iso-sourface of Q = 1 in translucent and streamlines

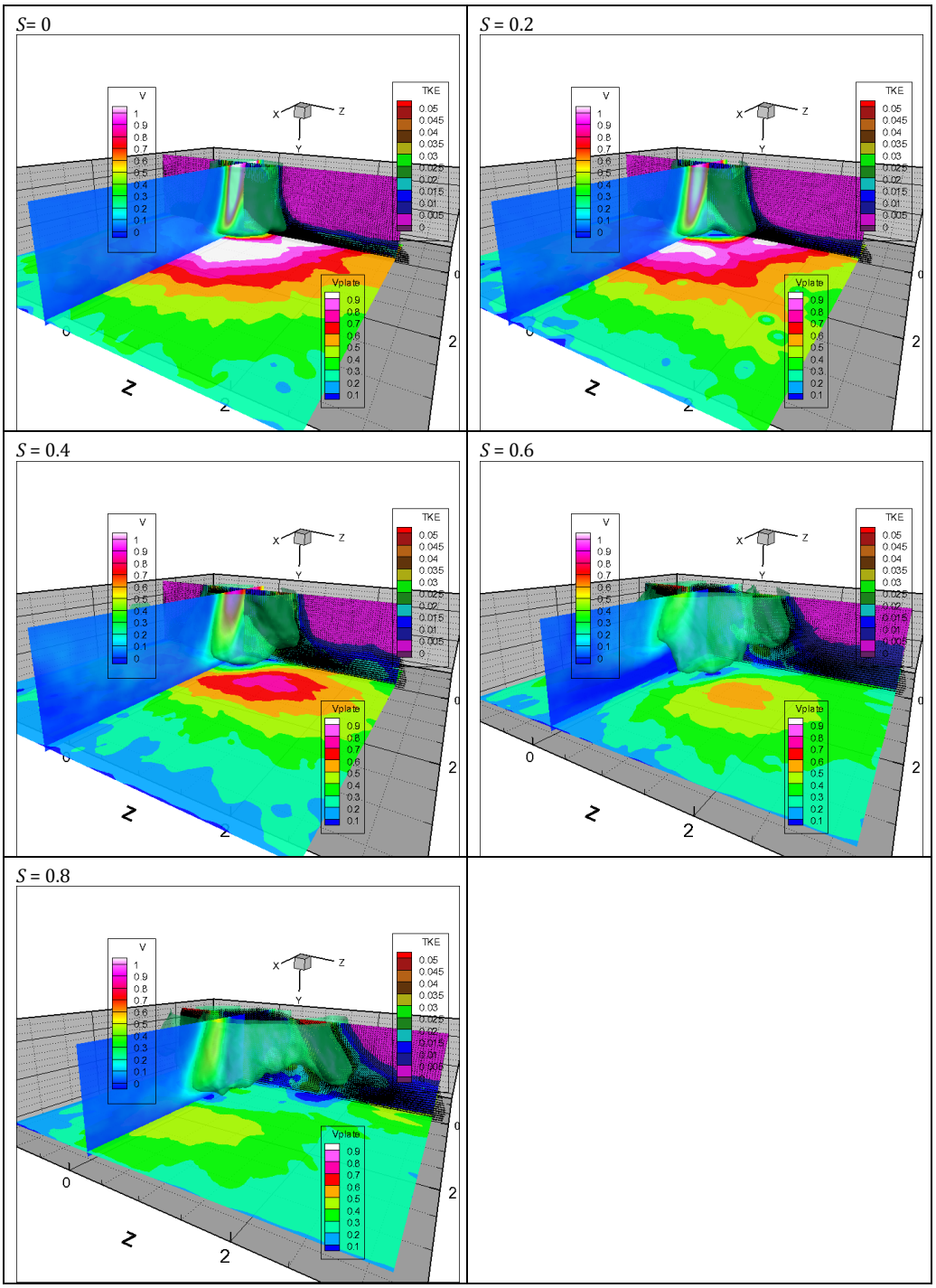

Fig. 4.18 Flow field statistics in swirling impinging jets

Chapter 5: Heat transfer in swirling impinging jets: experimental results

In the present chapter, experimental two dimensional measurements of convective heat transfer between a flat plate and a swirling air jet impinging on it are presented. This work is performed at a fixed Reynolds number (Re = 28,000) for different nozzle-to-plate distances (H = 2, 4, 6, 8 and 10)and for different swirl numbers (S = 0, 0.2, 0.4, 0.6 and 0.8). The heat transfer performances of swirling jets are also compared with those of a circular jet in order to account for both effects of the swirl and of the cross strips in the nozzle. Experimental measurements are carried out by means of IR thermography applied to the "heated thin foil" heat transfer sensor. Data are reported as Nusselt number surface maps, surface averaged Nusselt number and surface standard deviation percentage of the Nusselt number, in the attempt to quantify heat transfer rate and uniformity. In particular, this work represents the first effort to quantify non-uniformity in convective heat transfer coefficients in case of swirling, multichannel and circular jets. Moreover, the author propose the use of the standard deviation percentage of the Nusselt number as a quantitative estimator for the heat transfer uniformity.

5.1 Experimental apparatus and measurement technique

The experimental apparatus, sketched in Fig. 5.1, includes a thin constantan foil (200 *mm* wide, 470 *mm* long and 50 *μm* thick). This foil, constituting the target plate, is heated by an electric current passing through it and is cooled by an air jet impinging on it. The plate is positioned horizontally with the jet impinging vertically below, in order to minimize the recirculation of exhaust hot air. A suitable stiffening tool is employed to assure the foil surface flatness. The cooling air, supplied by a compressor, goes through a pressure regulating valve, a Venturi tube for flow rate metering and a heat exchanger that keeps the (total)

temperature of the jet close to that of the ambient room air, then to a plenum chamber where pressure and temperature are metered, and finally impinges on the target plate. The swirling flow is obtained by the nozzle described in Chapter 4. Five dimensionless nozzle-to-plate distances H are considered, namely 2, 4, 6, 8 and 10.

The mass flow rate $\dot{m}$ is kept constant in order to have always the same value of the Reynolds number, defined as $Re = 4\dot{m}/(\pi\mu D)$ (μ is the viscosity coefficient of air), equal to 28,000.

Experimental measurements are performed for five different values of the Swirl number S, namely 0, 0.2, 0.4, 0.6 and 0.8 by using five different swirl generators. Tests are also performed with a circular jet (*CJ*) by removing the helical insert from the nozzle.

An infrared camera working in the 8-9 μm infrared band (FLIR SC6000 LW), is employed to measure the foil surface temperature with a spatial resolution of 3.7 pixels/mm (73 pixels/D). The IR camera is accurately calibrated with a blackbody (according to the calibration procedure described in Chapter 3) for the whole measurement range, the noise equivalent temperature level of the camera is about $20mK$ and the rms error from the blackbody calibration is less than 0.15 K. The back side of the impinged surface is covered with high emissivity paint to increase accuracy of temperature measurements.

In the present case, the IR camera is used in conjunction with the "heated thin foil" steady state heat transfer sensor, which supplies the average (in time) local convective heat transfer coefficient h between the thin metallic foil, uniformly heated by Joule effect, and the air jet impinging on it (described in Chapter 3).

The images of T_w and T_{aw} are averaged over 300 measured fields acquired at a frame rate of 2 Hz with an integration time of 10 ms; the quantity T_w - T_{aw} is obtained by subtracting the two average thermal images (the *cold one* from the *hot one*). Furthermore, because of the thermal inertia of the foil and of the image time averaging process, present measurements have to be considered as time averaged, i.e. fluctuations due to turbulence are not being measured. The experimental data are reduced in dimensionless form in terms of Nusselt number Nu. Data are also presented as surface averaged Nusselt number $\overline{Nu}$ and surface standard deviation percentage of Nusselt number σ_{Nu}.

In particular $\overline{Nu}$ and σ_{Nu} are evaluated through Eqs. 5.1 and 5.2 on different circular areas A_r (changing the radius r) with a fixed centre identified as the intersection of the jet axis and the target plate:

$$\overline{Nu}(r) = \frac{1}{A_r} \int_{A_r} Nu \cdot dA_r \qquad 5.1$$

$$\sigma_{Nu}(r) = \frac{\sqrt{\frac{1}{A_r} \int_{A_r} (Nu - \overline{Nu}(r))^2 \cdot dA_r}}{\overline{Nu}(r)} \cdot 100 \qquad 5.2$$

Nu maps and radial distributions of $\overline{Nu}$ and σ_{Nu} are used to quantify the convective heat transfer rate and uniformity and to deduce the flow field structure. With uncertainty analysis, based on the method of Kline and McClintok (1953), taking into account measurements errors in flow rate, foil temperature, ambient temperature, voltage and current, measurements errors are mostly found to be less than +/-3.0% for *Nu* and +/-1.5% for $\overline{Nu}$ and σ_{Nu}.

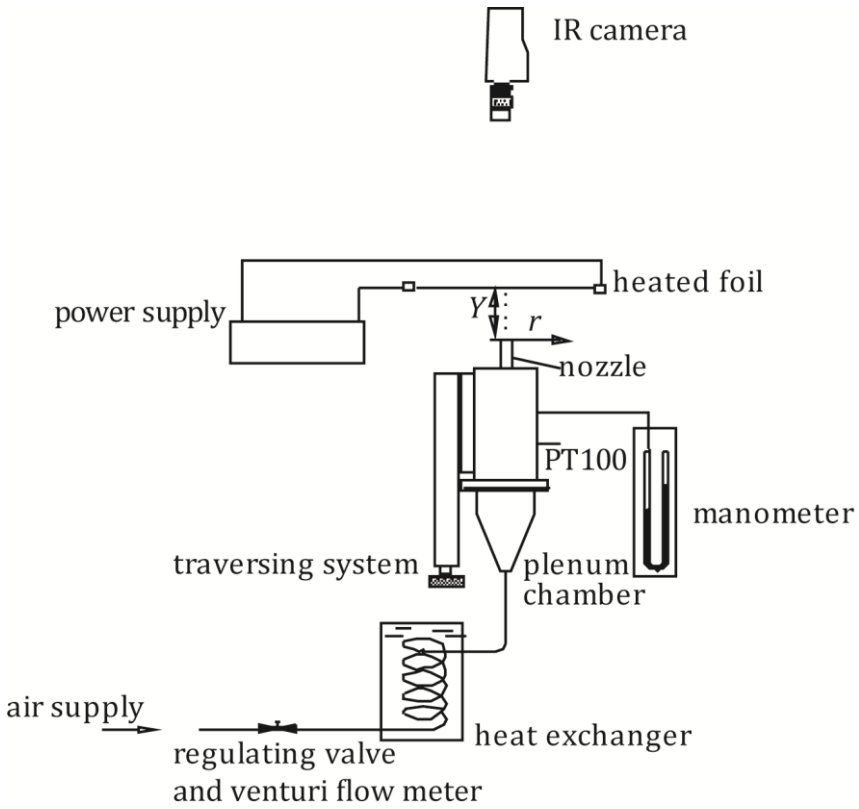

Fig. 5.1 Experimental setup (from Ianiro and Cardone, 2011)

5.2 Results

5.2.1 Heat transfer maps

In Fig. 5.2 are shown heat transfer results for a circular impinging jet (*CJ*) obtained with the same cylindrical nozzle used for the swirling jets (without the helical insert). Measurements show that *Nu* has little dependence on the nozzle-to-plate distance in regions for which *r* is higher than 3. At these large radii, *Nu* decreases as a result of the increase in the boundary layer thickness in the wall jet region. In the impinged area, *Nu* varies with *H*; for *H* = 2, and 4, a first ring-shaped region with a local *Nu* maximum appears at $r \approx 0.5$ and an outer region with a local *Nu* maximum appears at $r \approx 2$. For *H = 2,* these local maxima are higher than the values of *Nu* in the stagnation point (*r* = 0) as well assessed in literature (e.g., Goldstein et al. 1986 and Meola et al. 1996). In particular, the local maxima at *r* = 2 are attributed to the enhancement of heat transfer from entrainment caused by ring vortices that develop in the shear layer; vortex rings act as obstacle in the free stream and cause unsteady separation and turbulent reattachment downstream (Hadziabdic and Hanjalic, 2008) according with what seen also from flow field measurements.

As well assessed in literature (e.g., Martin, 1977), the stagnation *Nu* increases with *H* and reaches its maximum for *H = 8* (with a value of *Nu* = 148 in the present study), and then it decreases. This increase in stagnation *Nu* can be related to penetration of turbulent-induced mixing from the shear layer, in fact Schlunder and Gnielinski (1967) found both the maximum turbulence and the maximum stagnation point heat transfer occurring at *H* = 7.5; Gardon and Akfirat (1965) suggested that the increasing level of turbulence causes the heat transfer rate at the stagnation point to increase even if the jet centerline arrival velocity is falling. The increase in heat transfer rate ceases when the increase in turbulence does not compensate for the fall in the jet velocity.

As expected from flow field measurements, the heat transfer results obtained with the insert show a completely different behaviour. In Figs.Fig. 5.3-Fig. 5.6 are reported Nusselt number maps obtained for *S* = 0, 0.4, 0.6 and 0.8 and for *H* = 2, 6 and 10. For the sake of brevity, only these maps are shown also because they allow a good summary of the most relevant aspects.

In the case of the multichannel jet (*S* = 0), the 2D Nusselt number maps,

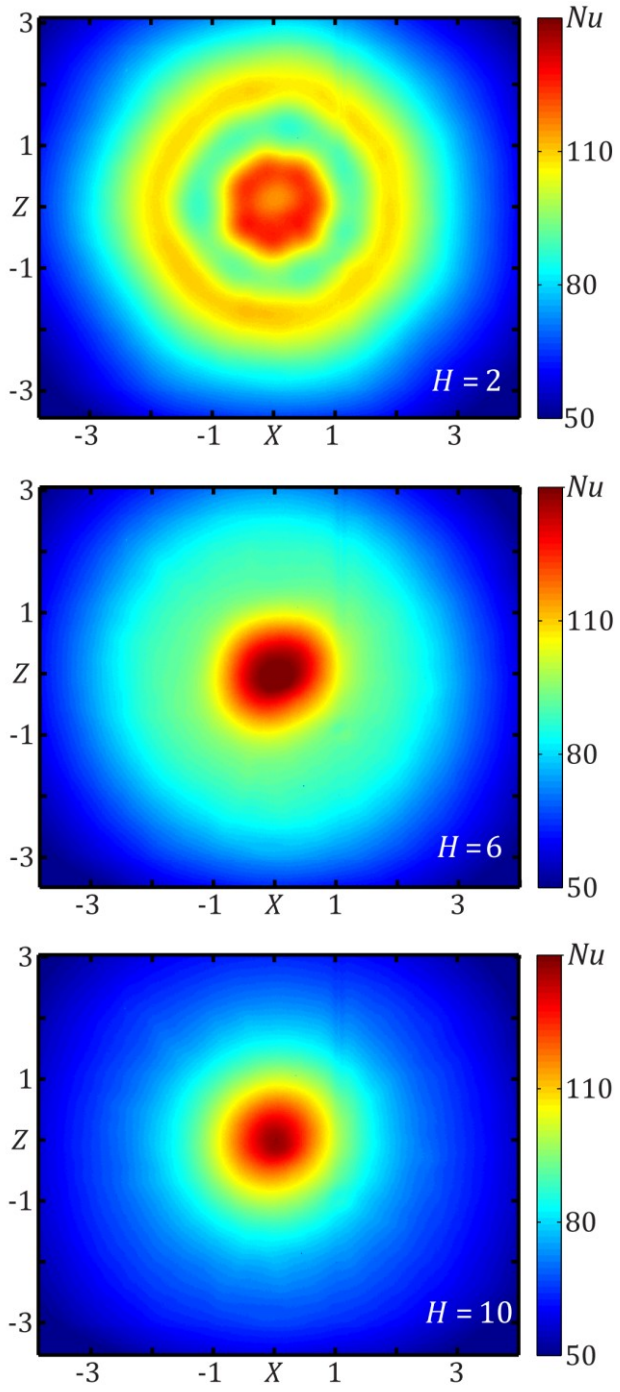

Fig. 5.2 *Nu* maps for *CJ* at *Re*=28,000 and *H* = 2, 6 and 10 (from Ianiro and Cardone, 2011)

reported in Fig. 5.3, show that four distinct stagnation regions are present for H = 2. Clearly, the flow leaving the nozzle is not characterized by coherence azimuthally, but it splits into four separate jets due to the presence of the four channels within the insert. For longer distances, however, the jets tend to merge into a single impingement area. Unlike the circular impinging jet, the maximum Nu values are obtained at the shorter considered distance, then, there is a monotonic decrease with increasing the nozzle-to-plate distance. At short distances, the multichannel impinging jet provides, in the impinged area, very high heat transfer values compared to the circular impinging jets. This is probably related to the interaction between the four jets at the nozzle exit and to a complex entrainment behaviour. As shown from flow field measurements, two shear layers exist in the flow field: one in the region between the four jets and the external environment and another one in the region in the centre of the jets. The small vortical structures visualized in Fig. 4.17 cause a deeper penetration of the turbulence in the centre of the jet; moreover no ring vortices effect is seen because the cross insert dramatically affects the development of the ring vortices as seen in Fig. 4.17 and in analogy with what found by Violato et al. (2011) for the chevron jet. Therefore, despite its simple geometrical configuration, the multichannel jet exhibits a complex flow field and requires further analysis.

The jets with swirl number equal to 0.2 and 0.4 (both considered as weak swirl jets in literature) show similar behaviours therefore only the Nu maps for S = 0.4 are reported in Fig. 5.4 and discussed. In all the considered cases, the heat transfer over the whole observed area is lower than the heat transfer obtained with the multichannel jet; this is clearly related to the axial flux weakening in the impinged area caused by the swirl.

At the shortest considered distance, the distribution of Nusselt number does not seem to be very different from that obtained with the multichannel jet and the effect of the swirl is not evident. If compared with the S = 0 case (Fig. 5.3), the heat transfer values are just slightly lower and the heat transfer topology still shows four high heat transfer peaked regions, which are clearly related to the presence of the insert; the impinged area looks broadened by the swirl, but the Nu distribution is still not uniform.

By increasing the nozzle-to-plate distance, it seems that the four jets merge at a shorter distance from the nozzle exit (compared to the multichannel jet) producing a more uniform heat transfer rate in the impinged area. The swirl flow induces broadening of the impinged area

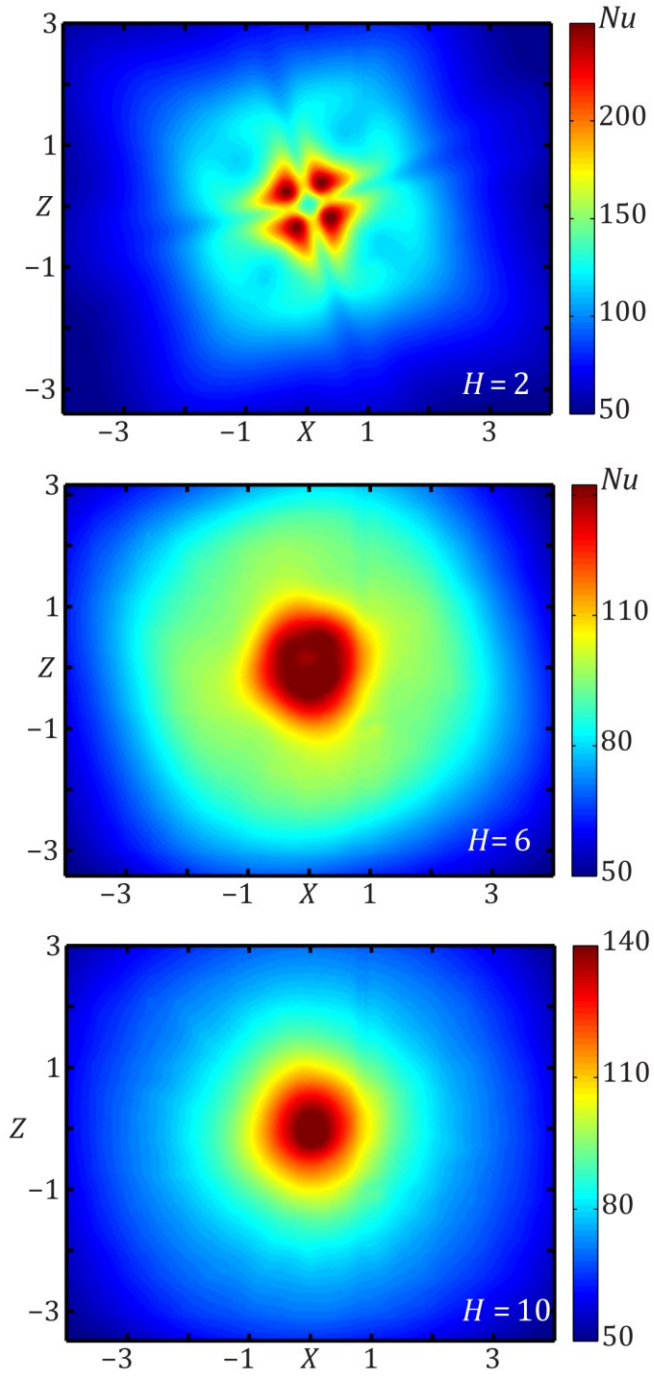

Fig. 5.3 *Nu* maps for multichannel jet (*S* = 0) at Re=28000 and *H* = 2, 6 and 10 (from Ianiro and Cardone, 2011)

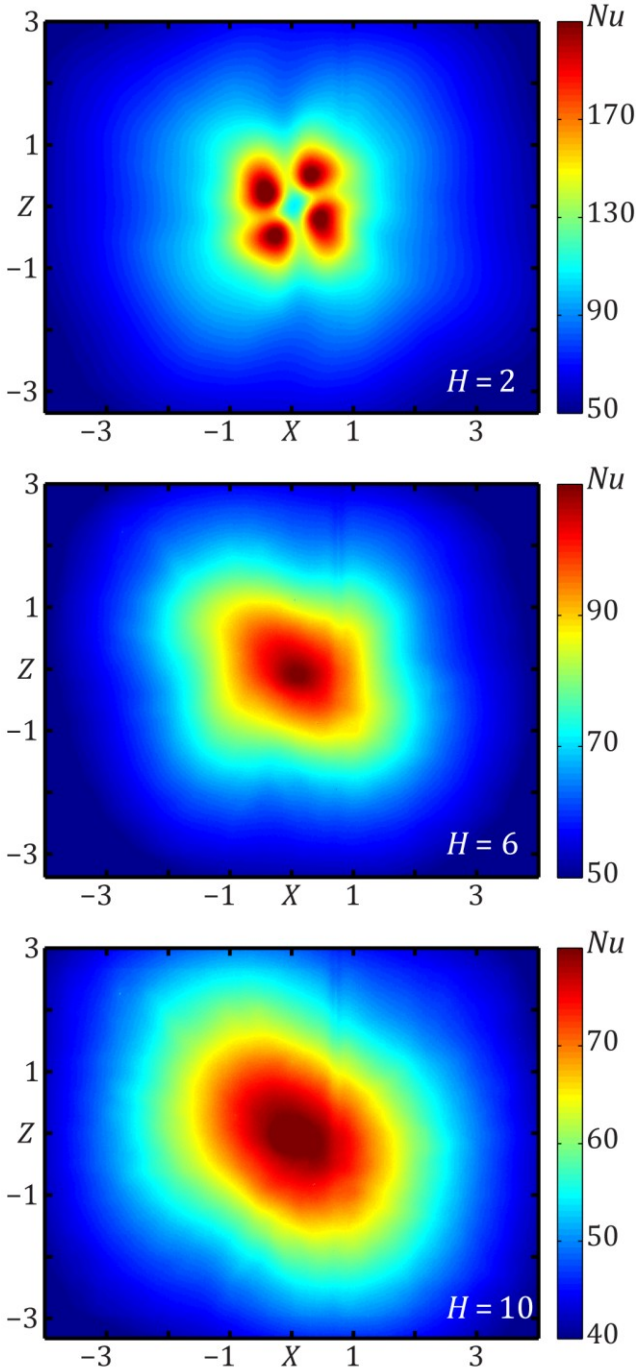

Fig. 5.4 *Nu* maps for the *S* = 0.4 jet at Re=28000 and *H* = 2, 6 and 10 (from Ianiro and Cardone, 2011)

and of the wall jet region. The impinged area does not show any coherence azimuthally, but it exhibits a lozenge shape with rounded edges for H = 6. This phenomenon is probably caused by the swirling device that, as seen previously, affects the development of the shear layer in correspondence of the cross edges; so, the jet is more broadened along two preferential directions and less along the other two. This effect is less evident when increasing the nozzle-to-plate distance and, obviously, the pattern appears rotated due to the swirl effect.

The jet with S = 0.6, as reported in literature, appears in a condition of transition between the cases of low and high degree of swirl. The Nu maps for S = 0.6 are reported in Fig. 5.5. For all the considered distances, the swirl is strong enough to produce great broadening of the stagnation region; this aspect is coupled with a decrease of the heat transfer values, compared to the jets at lower swirl number (Fig. 5.4and Fig. 5.3). The impingement regions related to the four channels merge, but not completely. In fact, in the Nu map for S = 0.6 and H = 6, two high heat transfer peaked regions are still evident while the other two are smaller and seem to be close to merging with the larger ones.

In the Nu map for S = 0.6 and H = 10, only two peaked regions are present, which are highly decentralized and broadened (probably due to the merging). Even if the two peaked regions are still present, the map shows a large region with low and almost constant heat transfer (Nu ranging between 45 and 50). As already mentioned, the presence of the peaked regions can be related to the type of swirling device used. There is some analogy between the maps shown in Fig. 5.4 and those in Fig. 5.5 for H =6 and 10. The aspect that adds great interest for the S = 0.6 jet, is the presence of a region with low Nu level in the centre of the impinged plate that can be related to a recirculation region in the centre of the jet caused by the vortex breakdown phenomenon. In fact, swirling flows produce axial pressure gradients that become stronger with increasing the swirl number and that can cause, as seen in the previous chapter, breakdown of the vortex core at the centre of the swirling jet producing a recirculation region.

The case of S = 0.8 fully falls in the definition of high swirl flow; in fact the effects of the vortex breakdown are evident in the Nusselt number maps reported in Fig. 9. In these maps, a very low heat transfer zone caused by the recirculation is always present in the centre of the impinged area. The distinction between the higher heat transfer peaked regions is clear for all the nozzle-to-plate distances analyzed. At a shorter distance the heat transfer peaks caused by the swirl appear weaker and more decentralized compared to the jets at lower swirl numbers; with

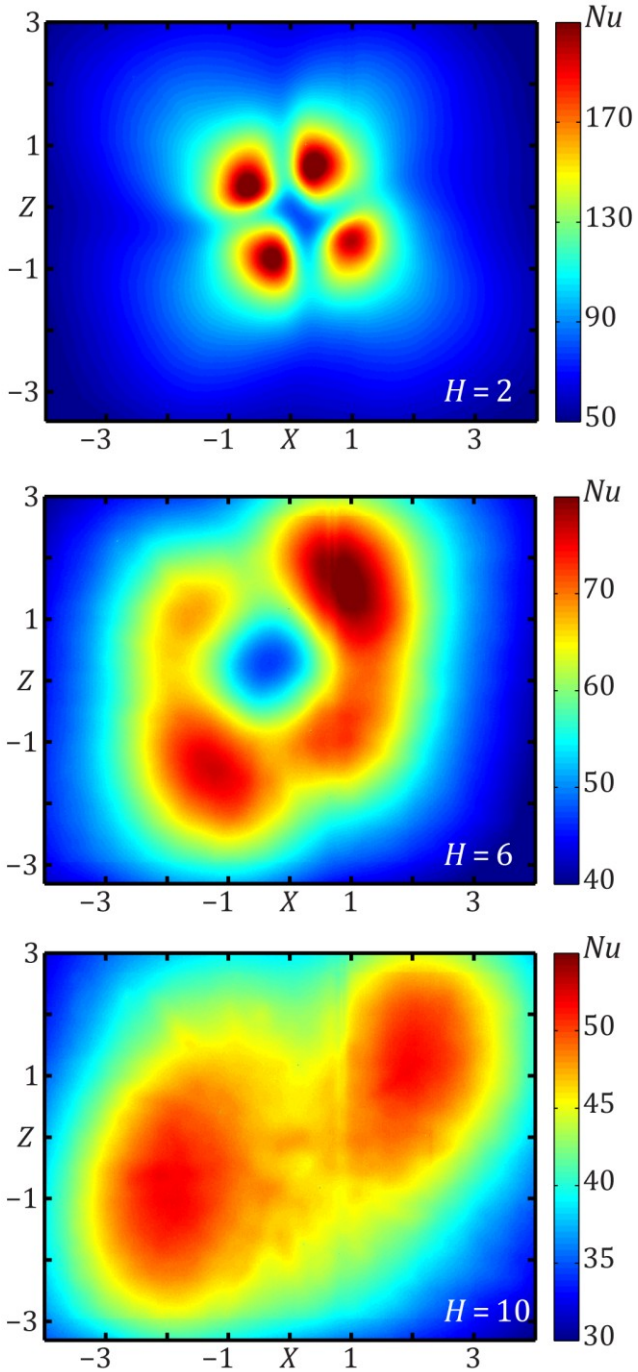

Fig. 5.5 *Nu* maps for the *S* = 0.6 jet at Re=28000 and *H* = 2, 6 and 10 (from Ianiro and Cardone, 2011)

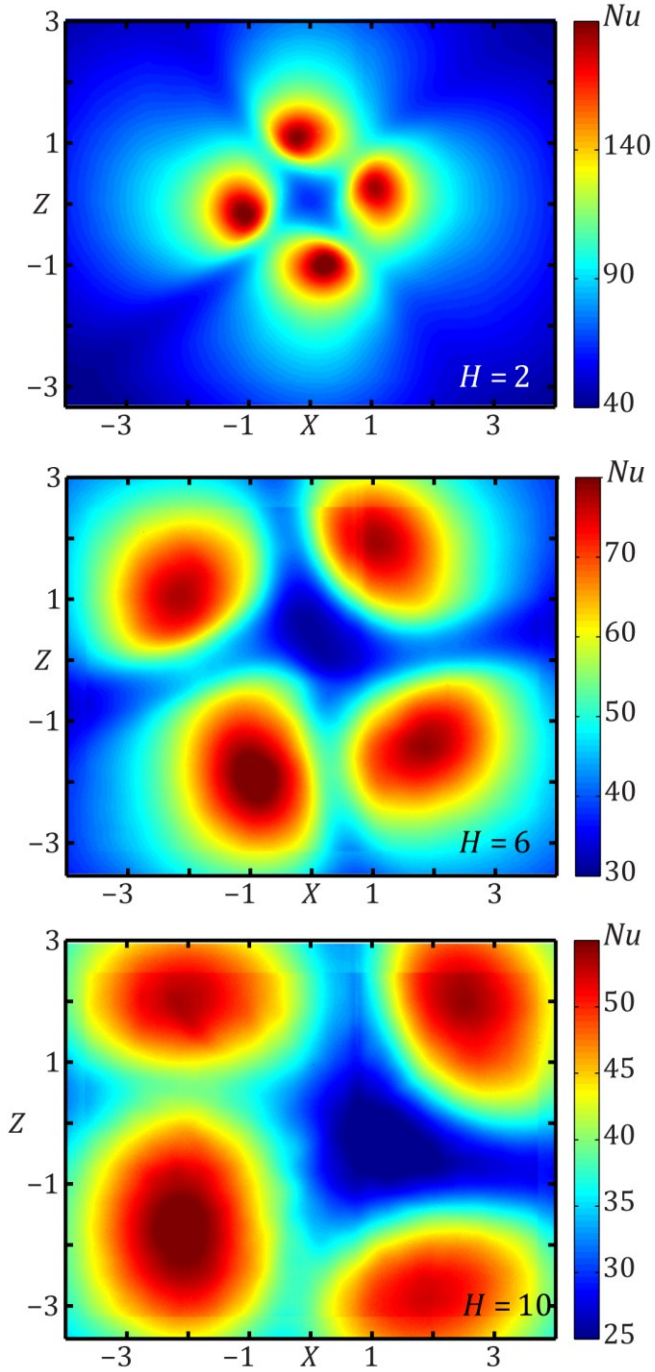

Fig. 5.6 *Nu* maps for the *S* = 0.8 jet at Re=28000 and *H* = 2, 6 and 10 (from Ianiro and Cardone, 2011)

increasing *H,* the four stagnation points, related to the four channels of the jet, gradually shift away, from the centre of the plate, in radial direction; this because the four jets, leaving the nozzle, encounter the recirculation region on the jet axis, which acts as an obstacle to their merging. The jets coming out from the four channels, for S=0.8, really behave as four separate jets.

5.2.2 Radial distribution of Nu average and standard deviation on circular areas

In order to understand the effect of the multichannel insert, a comparison between the values, of surface averaged (on circular areas) Nusselt number and of surface standard deviation percentage (on circular areas) of the Nusselt number obtained with the multichannel

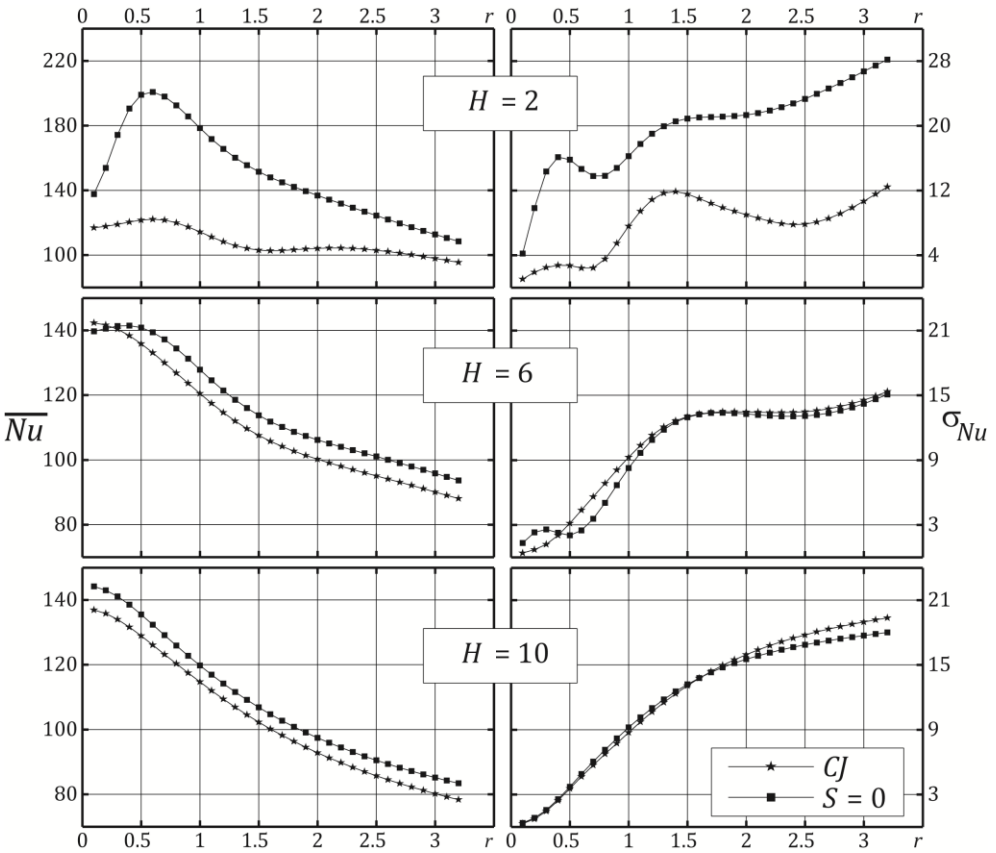

Fig.5.7 $\overline{Nu}$ and σ_{Nu} radial distributions at *H* = 2, 6 and 10 for the Circular Jet (*CJ*)and for the *S* = 0 Jet (from Ianiro and Cardone, 2011)

and with the circular impinging jet is presented (as function of r) in Fig.5.7 for H = 2, 6 and 10. The multichannel jet is characterized, in almost all conditions (r, H), by heat transfer rate higher than that for the *CJ*. At the shortest considered distance, the multichannel insert causes a high increase of heat transfer in the centre of the impingement region, which is coupled with a very bad uniformity compared to the circular jet. As stated before, this is probably due to the interaction between the four jets at the exit of the nozzle. Only at H =6 and 10 the performances in terms of uniformity are quite similar (the standard deviation percentage of heat transfer produced by the multichannel jet is slightly lower).

It should be pointed out that the increase of the Nusselt number for the multichannel jet (S=0) is partially related to an increase of the fluid speed at the nozzle exit, which is caused by the area reduction due to the presence of the insert. In fact, in the tested configuration, this area reduction is about 13%, entailing an equivalent nozzle diameter that is about 6% smaller and, consequently, the effective Reynolds number is about 6% higher. According to correlations reported by Viskanta [3], $\overline{Nu} \propto Re^{0.87}$ and therefore the increase of exit fluid speed should provide an increase of average heat transfer of about 5%.

For H = 2 the multichannel jet provides an increase of the average heat transfer higher than 13% for all r values with a maximum of 67% at r =0.6; this result comes from a combination of effects, which are the increased exit flow speed and the shear layer development mechanism discussed before.

For H = 6 and 10, except the case of r < 0.5 and H =6, the multichannel jet produces always a global heat transfer that is about 6-7% higher than that produced by the circular jet for all r values; this effect is clearly related to the higher exit speed due to the presence of the insert in the nozzle. Based on this consideration, the heat transfer enhancement found in literature is not related to the swirling motion but to the fact that the four narrow channels (Huang and El Genk, 1998) as well as the swirling strips (Lee et al. 2002, Wen and Yang 2003, Yuan et al 2006) reduce the exit area and cause an increase of the exit speed with respect to the circular jet.

The combined influence of swirl number (0, 0.2, 0.4, 0.6, 0.8) and of nozzle-to-plate distance (2, 4, 6, 8, 10) on the heat transfer can be understood by comparing the $\overline{Nu}(r)$ and $\sigma_{Nu}(r)$ profiles reported in Fig. 5.8.

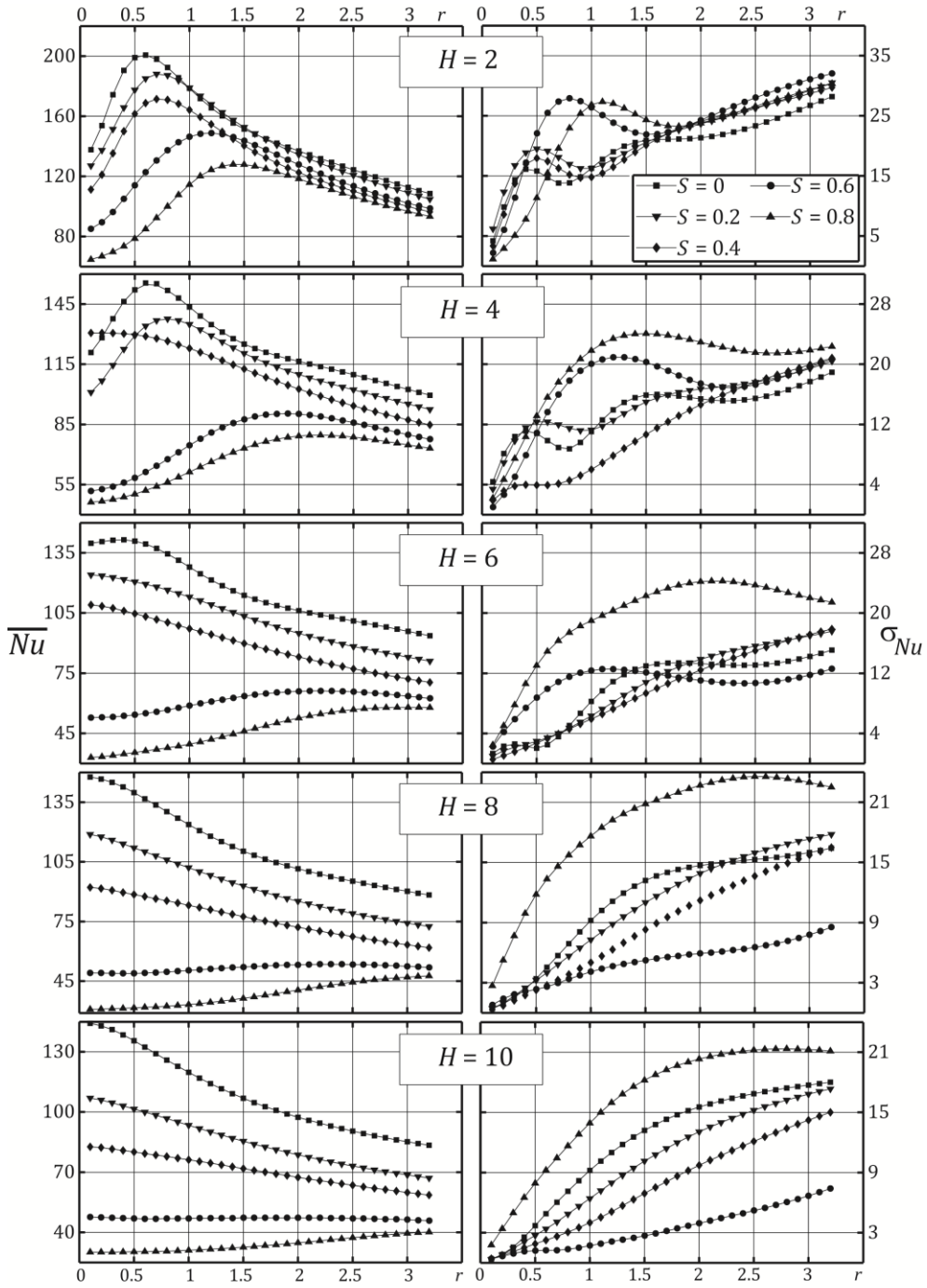

Fig. 5.8 : $\overline{Nu}$ and σ_{Nu} radial distributions for Swirl number 0, 0.2, 0.4. 0.6. 0.8 and for H = 2, 6 and 10 (from Ianiro and Cardone, 2011)

For H = 2 and 4, if a zone on the impinged plate of radius equal to about 3.2 nozzle diameters is considered as target plate, the so surface averaged Nusselt number exhibits a difference lower than 20% between the best case (S=0). and the worst case (S=0.8). Moreover, the swirler do not really improve the heat transfer uniformity, since, if the whole investigated area is considered, the surface standard deviation percentage of the Nusselt number obtained for S=0 is the lowest one.

Only for low r, the σ_{Nu} provided by swirling jets is lower because the swirl induces broadening of the impingement region and displacement of the heat transfer peaks.

By increasing the nozzle-to-plate distance the swirl effect becomes evident. For H = 6 an increase of 0.2 in the swirl number causes a decrease of about 10% in the global heat transfer over the whole observed area. Only the swirler with S = 0.6 produces a σ_{Nu} absolutely lower than the multichannel jet, but paying the price of a strong reduction in global heat transfer.

Also tests for H = 8 and H = 10 confirm the reduction of global heat transfer over the whole investigated area induced by swirling nozzles. The percent reduction of $\overline{Nu}$ is almost linear with increasing the swirl number. At the same time, all the swirlers, except the jet with S = 0.8, show very good performance in heat transfer uniformity, especially for H =10. The best performance in terms of low σ_{Nu} is obtained for H =10 by the swirling nozzles with swirl number equal to 0.4 and 0.6. Namely, the S = 0.6 jet shows an almost constant heat transfer over a zone of r up to 3.2 on the impinged plate, but with a reduction of about 50% in the global heat transfer if compared with the multichannel jet. On the opposite, at the highest swirl number, the presence of the four distinct highly decentralized stagnation zones (shown in Fig. 5.6) entails the highest standard deviation percentage.

5.2.3 Validation of results

A comparison between the heat transfer results obtained with swirling jets is not easy to do because the choice of type and shape of the swirling nozzle can crucially affect the magnitude of the measured heat transfer coefficients. In order to validate the heat transfer measurements presented in this work, the values of the local Nusselt number at r = 2 (scaled with $Re^{0.76}$ according to Goldstein et al.1986) obtained with the circular jet are compared in Fig. 5.9 with the results from earlier investigations (Goldstein et al.1986, Lee et al. 2002, Yuan et al 2006); as can be seen, there is a quite good agreement. This comparison is done

outside of the stagnation region to avoid , at least partly, the influence of differences in the jet-exit geometries (Colucci and Viskanta, 1996) of the different studies.

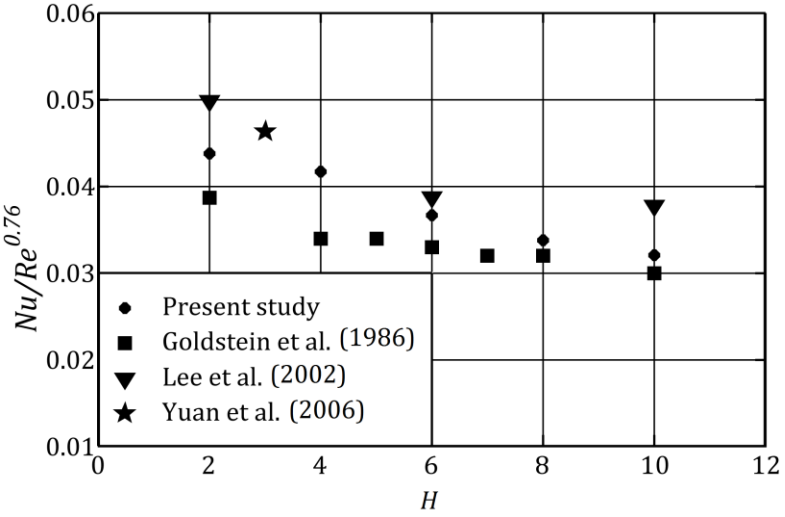

Fig. 5.9: Variation of $Nu/Re^{0.76}$ with nozzle-to-plate distance for the circular jet at r = 2 (from Ianiro and Cardone, 2011)

Conclusions

In this thesis, flow field and heat transfer in swirling impinging jets are experimentally investigated and compared with those of circular jets in similar conditions. Swirling impinging jets are obtained by using cross swirling strips inside the nozzle as swirl generators with swirl numbers equal to 0, 0.2, 0.4, 0.6 and 0.8, in order to study multichannel, low swirl and high swirl jets. Three-dimensional three-components measurements in free (at Re = 1,000) and impinging (at H = 2 and at Re = 10,000) swirling jets are carried out by means of time resolved tomographic PIV. Both averaged and instantaneous flow fields are presented and the dynamics of coherent structures are described.

Convective heat transfer measurements on the impinged plate (at H = 2, 4, 6, 8 and 10 and at Re = 28,000) are carried out with the heated thin foil technique along with temperature measurements from IR thermography. The measured heat transfer distribution for different values of the Swirl number are also compared with the heat transfer distribution of circular impinging jets. Through the analysis of the Nusselt number averaged on circular areas, it was possible to quantitatively assess the heat transfer rate, while with the analysis of the standard deviation percentage of Nu on the same circular areas was, for the first time, quantitatively analysed the heat transfer uniformity.

As expected, the flow field is not axis-symmetric because in all the cases actually four jets are issued from the nozzle due to the presence of the helical swirl generator. The four jests develop in stream-wise direction and two shear layers are present: one in the centre between the four jets and one in the external part of the jet. The development of these shear layers is influenced, of course, by the swirl number. The effect of swirl on the spreading angle of the jet is quite noticeable and the swirl has substantial influence on the entrainment rate.

Instantaneous flow field measurements show that at low swirl, the flow is dominated by helical vortices. By increasing the swirl number, the

presence of a central vortex core is shown; at high swirl, the breakdown of the vortex core causes the presence of a recirculation zone on the jet axis and the phenomenon of the precessing vortex core.

Circular impinging jets are characterized by toroidal vortices that are convected towards the plate then are stretched on the plate until they break up causing the formation of a turbulent boundary layer in the wall jet. The formation of the turbulent boundary layer on the wall is found to be in correspondence of the second outer maximum in the heat transfer distribution in circular impinging jets at $H = 2$.

Due the introduction of the cross insert, the ring vortices are not visualized. Turbulence is organized in smaller coherent structures compared to the case of the circular jet. From the vortex visualizations with Q criterion it is not easy to identify organized and coherent structures in the jets that are characterized by small vortices both in their external and internal shear layer. Those small coherent structures cause a deeper penetration of turbulence in the core of the jet. On the wall, the turbulent boundary layer develops already near the impingement. The turbulence level on the wall is quite homogeneous and, according to that, are not found outer maxima of heat transfer as in the case of the circular jet.

The comparative analysis with the circular impinging jet show that the multichannel nozzle (S=0) is characterized by a quite higher average heat transfer rate at all the considered nozzle-to-plate distances, with very high heat transfer peaks only at the shortest considered distance($H = 2$). This effect at short distances is due to the different entrainment mechanism along with a higher flow exit speed caused by the area reduction induced by the swirling insert. This advantage is less evident at higher nozzle-to-plate distances. In fact, in the circular impinging jet, the global heat transfer increases with the nozzle-to-plate distance of up to eight diameters, while in all the tested cases, the mean heat transfer, related to all the swirling jets, decreases with increasing the nozzle-to-plate distance. At high nozzle-to-plate distances, the multichannel jet produces an enhancement in heat transfer that seems to be due just to the higher exit speed, which is caused by the area reduction induced by the swirling insert.

At a fixed nozzle-to-plate distance, by increasing the swirl number, it is possible to see that the swirling jets are characterized by a broadening of the impingement region and by a decrease of the global heat transfer. The swirling jets show the best performance in heat transfer uniformity, at a nozzle-to-plate distance higher than six diameters; the jet with S=0.8

represents an exception because its higher degree of swirl causes the formation of four distinct stagnation zones, thus causing the highest standard deviation percentage of Nusselt number.

Ultimately, the results obtained highlight the peculiarity of the swirling nozzle with S = 0.6 showing, at high nozzle-to-plate distance, an almost constant heat transfer distribution over the whole investigated area, with a Nusselt number standard deviation percentage lower than 8%.

References

S. V. Alekseenko, A.V. Bilsky, V. M. Dulin and D. M. Markovich (2007), Experimental study of and impinging jets with different swirl rates, International Journal of Heat and Fluid Flow, 28, 1340-1359.

M. P. Arroyo and C. A. Greated (1991), Stereoscopic particle image velocimetry, Meas Sci Technol 2, 1181–1186.

T. Astarita and G. Cardone (2000), Thermofluidynamic analysis of the flow in a sharp 180° turn channel, Experimental Thermal and Fluid Science, 20, 188-200.

C. H. Atkinson and J. Soria (2007), Algebraic reconstruction techniques for tomographic particle image velocimetry. In: Proceedings of 16th Australasian fluid mechanics conference, Gold Coast

C. H. Atkinson, J. Soria (2009), An efficient simultaneous reconstruction technique for tomographic particle image velocimetry, Exp Fluids 47, 553–568.

P. Billant, J. M. Chomaz and P. Huerre (1998), Experimental study of vortex breakdown in swirling jets, J. Fluid Mech., 376, 183-219.

P. Bradshaw, D. H. Ferriss, R. F. Johnson (1963), Turbulence in the noise producing region of a circular jet, Journal of Fluid Mechanics 19, 591-624.

C. Brücker (1996), 3-D Scanning particle image velocimetry: technique and application to a spherical cap wake flow, Appl. Sci. Res 56, 157–179.

C. E. Cala, E. C. Fernandes, M. V. Heitor and S. I. Shtork (2006), Coherent structures in unsteady swirling jet flow, Experiments in Fluids 40, 267-276.

G. Cardone (2007), IR heat transfer measurements in hypersonic plasma flows, QIRT Journal 4, 233-251.

G. M Carlomagno and G. Cardone (2010), Infrared Thermography for Convective Heat Transfer Measurements. Exp Fluids 49, 1187–1218.

G. M. Carlomagno and L. de Luca (1989), Infrared thermography in heat transfer In: Yang WJ, editor. Handbook of flow visualization. London, Hemisphere Chapter 32: 531-553.

R. C. Chanaud (1965), Observations of oscillatory motion in certain swirling flows, Journal of Fluid Mechanics 21, 111-127.

R. H. Chen, J. F. Driscoll, J. Kelly, M. Namazian and R. W. Schefer (1990), A Comparison of Bluff-Body and Swirl-Stabilized Flames, Combust. Sci. and Tech. 71, 197-217.

N.A. Chigier and A. Chervinsky (1967), Aerodynamic study of turbulent burning free jets with swirl, Symposium (International) on Combustion 11, 489-499.

T. H. Chilton and A. P. Colburn (1934), Mass Transfer (Absorption) Coefficients Prediction from Data on Heat Transfer and Fluid Friction, Industrial & Engineering Chemistry 26, 1183–1187.

D. W. Colucci and R. Viskanta (1996), Effect of nozzle geometry on local convective heat transfer to a confined impinging air jet, Experimental Thermal and Fluid Science 13, 71-80.

D. L. Compton (1972), Use of an infrared-imaging camera to obtain convective heating distributions. AIAA Journal 10,1130-2.

D. Cooper, C. Jackson, B. E. Launder and G. X. Liao (1993), Impinging jet studies for turbulence model assessment – I. Flow-field experiments, International Journal of Heat and Mass Transfer 36, 2675–2684.

S. Crow and F. Champagne (1971), Orderly structure in jet turbulence, Journal of FluidMechanics 48, 547–591.

I Danaila, J. Dusek and F. Anselmet (1997), Coherent structures in a round, spatially evolving, unforced, homogeneous jet at low Reynolds numbers, Physics of Fluids 9, 3323-3342.

L. de Luca and G. Cardone (1991), Modulation transfer-function cascade model for a sampled ir imaging-system, Applied Optics 30, 1659-1664

S. Discetti and T. Astarita (2011a), A fast multi-resolution approach to tomographic PIV, Experiments in Fluids, DOI: 10.1007/s00348-011-1119-x

S. Discetti and T. Astarita (2011b), Fast multi-resolution 3D PIV, 9th International Symposium On Particle Image Velocimetry – PIV'11, Kobe, Japan, July 21-23.

S. Discetti and T. Astarita (2011c), Spatial Filtering Improved Tomographic PIV, 9th International Symposium On Particle Image Velocimetry – PIV'11, Kobe, Japan, July 21-23.

S. J. Downs and E. H. James (1987), Jet Impingement Heat Transfer --A Literature Survey, ASME Paper No. 87-H-35, ASME, New York.

E. R. G Eckert. and R. M. Drake (1972), Analysis of Heat and Mass Transfer, McGraw-Hill, New York.

G. E. Elsinga (2008), Tomographic particle image velocimetry and its application to turbulent boundary layers. PhD thesis, Delft University of Technology, Delft, The Netherlands (http://repository.tudelft.nl/file/1003861/379883)

G. E. Elsinga, F. Scarano, B. Wieneke and B. W. van Oudheusden (2006), Tomographic particle image velocimetry, Exp Fluids 41, 933–947.

G. E. Elsinga, J. Westerweel. F. Scarano and M. Novara (2011), On the velocity of ghost particles and the bias errors in Tomographic-PIV, Exp Fluids 50, 825-838.

M. Fabbri, S. Jiang, and V. K. Dhir (2005), A Comparative Study of Cooling of High Power Density Electronics Using Sprays and Microjets, Journal of. Heat Transfer 127-1, 38 (11 pages).

M. García-Villalba, J. Fröhlich and W. Rodi (2006), Identification and analysis of coherent structures in the near field of a turbulent unconfined annular swirling jet using large eddy simulation. Phys. Fluids 18, 055103.

R. Gardon and J. C. Akfirat (1965), The role of turbulence in determining the heat-transfer characteristics of impinging jets, Int. J, Heat Mass Transfer, 8, 1261-1272.

R. Gardon and J. Cobonpue (1962), Heat transfer between a flat plate and jets of air impinging on it, International Developments in Heat Transfer, A.S.M.E., New York.

Gartenberg E, Roberts AS. (1992) Twenty-five years of aerodynamic research with infrared imaging. J Aircraft 29, 161-171.

J. W Gautner, J. N. B. Livingwood and P. Hrycak (1970), Survey ofLiterature of Flow Characteristics of a Single Turbulent Jet Impinging on a Flat Surface, NASA TN D-5652.

M. B. Glauert (1956), The wall jet, Journal of Fluid Mechanics 1, 625-643.

R. J. Goldstein, A. I. Behbahani, a and K. Kieger Heppelmann (1986), Streamwise distribution of the recovery factor and the local heat transfer coefficient to an impinging circular air jet, International Journal of Heat and Mass Transfer, 29, 1227-1235.

A. K. Gupta, D. G. Lilley and N. Syred (1984), Swirl Flows, Abacus Press.

M. Hadziabdic and K. Hanjalic (2008), Vortical structures and heat transfer in a round impinging jet, Journal of Fluid Mechanics 596, 221-260.

R. Hain, C. J. Kahler and D. Michaelis (2008), Tomographic and time-resolved PIV measurements on a finite cylinder mounted on a flat plate, Exp Fluids 45, 715-724.

J. K. Harvey (1962), Some observations of the vortex breakdown phenomenon. Journal of Fluid Mechanics 14, 585-592.

G. T. Herrmann and A. Lent (1976), Iterative reconstruction algorithm, Computers in Biology and Medicine 6, 273-294.

K. D. Hinsch (2002), Holographic particle image velocimetry, Meas. Sci. Technol. 13, R61–R72.

C. J. Hoogendorn (1977), The effect of turbulence on heat transfer at a stagnation point, International Journal of Heat and Mass Transfer 20, 1333–1338.

G. H. Hu, D. J. Sun, and X. Y. Yin (2001), A numerical study of dynamics of a temporally evolving swirling jet. Phys. Fluids 13, 951-965.

L. Huang and M. S. El-Genk (1998), Heat transfer and flow visualization experiments of swirling, multi-channel, and conventional impinging jets, Int. J. Heat Mass Transfer, 41, 583-600.

Y. Huang, and V. Yang (2005), Effect of swirl on combustion dynamics in a lean-premixed swirl-stabilized combustor, Proceedings of the Combustion Institute 30, 1775-1782.

A. Ianiro and G. Cardone (2010), Measurement of surface temperature and emissivity with stereo dual-wavelength IR thermography, Journal Of Modern Optics 57, 1708-1715.

A. Ianiro and G. Cardone (2011), Heat transfer rate and uniformity in multichannel swirling impinging jets, Applied Thermal Engineering.

K Ichimiya and K Tsukamoto (2006), Heat Transfer from an Inflow-Type Swirling Turbulent Impinging Jet, JSME International Journal Series B, 49, 995-999.

K Ichimiya and K Tsukamoto (2010), Heat Transfer Characteristics of a Swirling Laminar Impinging Jet, Journal of Heat Transfer, 132, 012201 (5 pages).

S. Jakirlic, K. Hanjalic and C. Tropea (2002), Modeling Rotating and Swirling Turbulent Flows: A Perpetual Challenge, AIAA Journal, 40,1984-1996.

K. Jambunathan, E. Lai, M. A. Moss and B. L. Button (1992), A review of heat transfer data for single circular jet impingement, International Journal of Heat and Fluid Flow, 13, 106-115.

C. J. Kähler and J. Kompenhans (2000), Fundamentals of multiple plane stereo particle image velocimetry, Exp Fluids 29, S70–S77.

K. Kataoka, M. Suguro, H. Degawa, K. Maruo and I. Mihata (1987), The effect of surface renewal on jet impingement heat transfer, International Journal of. Heat and Mass Transfer 30, 559–567.

R. D. Keane and R. J. Adrian (1992), Theory of cross-correlation analysis of PIV images, Appl Sci Res 49, 191–215.

H. Klammer and W. Schupe (1983), Practical Layout and Economy of Pre-heating Chambers in Industrial Furnaces, Stahl Eisen 103, 531-537.

S. J Kline, and F. A. McClintock (1953), Describing Uncertainties in Single-Sample Experiments, Mechanical Engineering, 75, 3-8.

F. Lamarche and C. Leroy (1990), Evaluation of the volume of intersection of a sphere with a cylinder by elliptic integrals, Comput Phys Commun 59, 359–369.

N. C. Lambourne and D. W. Bryer (1961), The bursting of leading-edge vortices: some observation and discussion of the phenomenon, Aero. Res. Counc. R&M 36, 3282.

V. I. Lebedev, and V. A. Sokolov (1976), Study of Convection Component of Complex Heat Exchange of a Direct-Heating Furnace, Glass Ceram. 33, 352-354.

D. H. Lee, S. J. Won, Y. T. Kim and Y. S. Chung (2002), Turbulent Heat Transfer from a flat surface to a swirling round impinging jet , Int. J. Heat Mass Transfer, 45, 223-227.

J. Lepicovsky (1989), The role of nozzle-exit boundary layer velocity gradient in mixing enhancement of free jets. Proc, 3rd Joint ASCE/ASME Mechanics Conf., San Diego, CA, USA, July 9-12.

H. Liang and T. Maxworthy (2005), An experimental investigation of swirling jets, Journal of Fluid Mechanics 525, 115-159.

D. Liepmann and M. Gharib (1992), The role of streamwise vorticityin the near field entrainment of round jets, Journal of Fluid Mechanics 245, 643–668.

D. G. Lilley (1977), Swirl flows in combustion: a review, AIAA Journal 15, 1063-1078.

J. N. B. Livingood and P. Hrycak (1973), Impingement Heat Transfer from Turbulent Air Stream Jets to Flat Plates--A Literature Survey, NASA TM X-2778.

T. Loiseleux, J. M. Chomaz and P. Huerre (1998), The effect of swirl on jets and wakes: Linear instability of the Rankine vortex with axial flow, Physics of Fluids 10-5, 1120-1134.

M. V. Lowson (1964), Some experiments with vortex breakdown, Journal of the Royal Aeronautical Society 68, 343.

O. Lucca-Negro and T. O'Doherty (2001), Vortex breakdown: a review, Progress in Energy and Combustion Science 27, 431-481.

H. G. Maas, A. Gruen and D. Papantoniou (1993), Particle tracking velocimetry in three-dimensional flows, Exp Fluids 15, 133–146

H. Martin (1977), Heat and Mass Transfer between Impinging Gas Jets and Solid Surfaces, Advances in Heat Transfer, 13, 1–60.

J. E. Martin and E. Meiburg (1996), Nonlinear axisymmetric and three-dimensional vorticity dynamics in a swirling jet model, Phys. Fluids 8, 1917.

F. Martinelli, A. Olivani, and A. Coghe (2007), Experimental analysis of the precessing vortex core in a free swirling jet, Exp Fluids 42, 827-839.

S. McIlwain and A. Pollard (2002), Large eddy simulation of the effects of mild swirl on the near field of a round free jet, Phys. Fluids 14, 653.

C. D. Meinhart, S.T. Wereley and J. G. Santiago (2000), A PIV Algorithm for Estimating Time-Averaged Velocity Fields, Journal of Fluids Engineering 122, 285.

C. Meola (2009), A New Correlation of Nusselt Number for Impinging Jets, Heat Transfer Engineering, 30, 221–228.

C. Meola, L. de Luca and G. M. Carlomagno (1996), Influence of shear layer dynamics on impingement heat transfer, Experimental Thermal and Fluid Science 13, 29-37.

C. Meola, L. de Luca and G. M. Carlomagno (1995), Azimuthal instability in an impinging jet: adiabatic wall temperature distribution, Experiments in Fluids 18, 303-310.

D. Mishra, K. Muralidhar and P. Munshi (1999), A robust MART algorithm for tomographic applications, Num Heat Transfer Part B 35, 485–506.

V. Narayanan, J. Seyed-Yagoobi, and R. H. Page (2004), An experimental study of fluid mechanics and heat transfer in and impinging slot jet flow. International Journal of Heat and Mass Transfer 47,1827–1845.

M. Novara, K. J. Batenburg and F. Scarano (2010), Motion tracking-enhanced MART for tomographic PIV, Meas Sci Tech 21, 035401.

M. Novara, A. Ianiro and F. Scarano (2011), Adaptive interrogation for 3D-PIV, Proceedings 9TH International Symposium On Particle Image Velocimetry – PIV'11, Kobe, Japan, July 21-23.

T. S. O'Donovan and D. B. Murray (2007a), Jet impingement heat transfer e Part I: Mean and root-mean-square heat transfer and velocity distributions, International Journal of Heat and Mass Transfer 50, 3291-3301.

T. S. O'Donovan and D. B. Murray (2007b), Jet impingement heat transfer e Part II: A temporal investigation of heat transfer and local fluid velocities, International Journal of Heat and Mass Transfer 50, 3302-3314.

J. Ortega-Casanova, N. Campos and R. Fernandez-Feria (2010), Swirling jet models based on experimental measurements at the exit of swirl vane nozze. The 5th International Conference of Vortex Flows and Vortex Models, 7-10 November, Caserta-Italy

J. Panda and D. K. McLaughlin (1994), Experiments on the instabilities of a swirling jet, Phys. Fluids 6, 263.

S. H. Park and H. D. Shin (1993), Measurements of entrainment characteristics of swirling jets, International Journal of Heat and Mass Transfer 36, 4009-4018.

D. J. Peake, A. J. Bowker, S. J. Lockyear et al. (1977) Non intrusive detection of transition region using an infrared camera. AGARD-CP-224.

S. Polat, B. Huang, A. S. Mujumdar and W. J. M. Douglas (1989), Numerical Flow And Heat Transfer Under Impinging Jets: A Review, Annual Reviews of Heat Transfer 2, 157-197.

C. O Popiel and O. Trass (1991), Visualization of a free and impinging round jet, Experimental Thermal and Fluid Science 4, 253-264.

L. Prandtl (1904), On fluid motions with very small friction (in German). Third International Mathematical Congress, Heidelberg, 484–491.

M. Raffel, C. E. Willert and J. Kompenhans (1998), Particle image velocimetry: a practical guide. Springer, Berlin Heidelberg New York.

N. Rajaratnam (1976), Turbulent Jets, Elsevier, New York.

K. K. J. Ranga Dinesh and M. P. Kirkpatrick (2009), Study of jet precession, recirculation and vortex breakdown in turbulent swirling jets using LES, Computers & Fluids 38, 1232-1342.

H. Reichardt (1942), Gesetzmiissigkeiten der freien Turbulenz, VDI Forschungsheft, 414.

W.G. Rose (1962), A swirling round turbulent jet, Journal of Appllied Mechanics 29, 615.

S. R. Sargent, C. R. Hedlund and P. M. Ligrani (1998), An infrared thermography imaging system for convective heat transfer measurements in complex flows. Measurement Science & Technology 9, 1974-1981.

F. Scarano (2002), Iterative image deformation methods in PIV, Meas Sci Technol 13, R1–R19.

F. Scarano and M. L. Riethmuller (1999), Iterative multigrid approach in PIV image processing with discrete window offset, Exp Fluids 26, 513–523.

F. Scarano and M. L. Riethmuller (2000), Advances in iterative multigrid PIV image processing, Exp Fluids 29, S51–S60.

J. A. Schetz and A. E. Fuhs (1999), Fundamentals of Fluid Mechanics, Wiley.

E. U. Schlunder and V. Gnielinski (1967), Heat and mass transfer between surfaces and impinging jets, Chem. Eng. Tech., 39, 578-584.

H. Schrader (1961), Trocknung feuchter Oberfiachen mittels Warmluft- stralen, VDI Forschungsheft Ausgabe B 27, 484.

A. H. Shapiro (1954), The dynamics and thermodynamics of compressible fluid flow, Vols. I and II. New York: Ronald Press.

M. Sibulkin (1952), Heat transfer near the forward stagnation point of a body of revolution, Journal of the Aeronautical Sciences 19, 570.

R. Siegel and J. R. Howell (1992), Thermal Radiation Heat Transfer, 3rd edn. Hemisphere, Washington.

J. Soria (1996), An investigation of the near wake of a circular cylinder using a video-based digital cross-correlation particle image velocimetry technique, Exp Therm Fluid Sci 12, 221–233.

N. Syred (2006), A review of oscillation mechanisms and the role of the precessing vortex core (PVC) in swirl combustion systems, Progress in Energy and Combustion Science 32, 93-161.

N. Syred and J. M. Beér (1974), Combustion in swirling flows: A review, Combustion And Flame 23, 143-201.

V. Tangirala, R. H. Chen and J. F. Driscoll (1987), Effect of Heat Release and Swirl on the Recirculation within Swirl-Stabilized Flames, Combust. Sci. and Tech. 51, 75-95.

H. Thomann and B. Frisk (1968), Measurement of heat transfer with an infrared camera, Int. J Heat Mass Transfer 11, 819–826.

I. K. Toh, D. Honnery and J. Soria (2010), Axial plus tangential entry swirling jet. Exp Fluids, 48, 309-325.

M. Vanierschot and E. Van den Bulck (2008), Influence of swirl on the initial merging zone of a turbulent annular jet, Physics Of Fluids 20, 105104 (18 pages).

D. Verhoeven (1993), Limited-data computed tomography algorithms for the physical sciences, Appl Opt 32,3736–3754.

D. Violato, A. Ianiro, G. Cardone and F. Scarano (2011), Investigation on Circular and Chevron Impinging Jets by IR Thermography and Time-Resolved Tomographic PIV, Proceedings ASME-JSME-KSME Joint Fluids Engineering Conference 2011 (AJK2011-FED), July 24 - 29. Hamamatsu, Japan. 12 pp.

D. Violato and F. Scarano (2011), Three-dimensional evolution of flow structures in transitional circular and chevron jets, Physics of Fluids, doi: 10.1063/1.3665141

R. Viskanta (1991), Enhancement of Heat Transfer in Industrial Combustion Sysems: Problems and Future Challenges, Proceedings of the ASME /JSME Thermal Engineering Joint Conference, Vol. 5, 161-173.

R. Viskanta (1993), Heat Transfer to Impinging Isothermal Gas and Flames Jets, Experimental Thermal and Fluid Science 6, 111–134.

J. Ward and M. Mahmood (1982), Heat transfer from a turbulent, swirling impinging jet, Proceedings of the 7th International Heat Transfer Conference 3, 401-407.

M. Y. Wen and K. J. Jang (2003), An impingement cooling on a flat surface by using circular jet with longitudinal swirling strips, International Journal of Heat and Mass Transfer 46, 4657-4667.

J. Westerweel, D. Dabiri and M. Gharib (1997), The effect of a discrete window offset on the accuracy of cross-correlation analysis of digital PIV recordings, Exp Fluids 23, 20-28.

S. E. Widnall, D. B. Bliss and Tsai (1974), The instability of short waves on a vortex ring, J Fluid Mech 66, 35-47.

B. Wieneke (2008), Volume self-calibration for 3D particle image velocimetry, Exp Fluids 45, 549-556.

C. Willert (2006), Assessment of camera models for use in planar velocimetry calibration, Exp Fluids 41, 135–143.

C. Willert and M. Gharib (1991), Digital particle image velocimetry, Exp Fluids 10, 181-193.

C. D. Winant and F. K. Browand (1974), Vortex pairing: the mechanism of turbulent mixing layer growth at moderate Reynolds number, Journal of Fluid mechanics 63, 237-255.

N. A. Worth and T. B. Nickels (2008), Acceleration of tomo-piv by estimating the initial volume intensity distribution, Exp fluids 45, 847-856.

H. Q. Yang, T. Kim, , T. J. Lu and K. Ichimiya (2010), Flow structure, wall pressure and heat transfer characteristics of impinging annular jet with/without steady swirling, International Journal of Heat and Mass Transfer 53, 4092-4100.

P. A. Yazdabadi, A.J. Griffiths, and N. Syred (1994), Characterization of the PVC phenomena in the exhaust of a cyclone dust separator, Experiments in Fluids 17, 84-95.

References

S. Yokobori, N. Kasagi, M. Hirata, M. Nakamaru and Y. Haramura (1979), Characteristic behavior of turbulence and transport phenomena at the stagnation region of an axi-symmetrical impinging jet, Proc. 2nd Symp. Turb. Shear Flows, London, UK, 4, 4.12-4.17.

Z. X. Yuan, Y. Y. Chen, J. G. Jiang, C. F. Ma (2006), Swirling effect of jet impingement on heat transfer from a flat surface to CO2 stream, Experimental Thermal and Fluid Science, 31, 55–60.

A. J. Yule (1978), Large structure in the mixing layer of a round jet, Journal Fluid Mechanics 89, 413-432.

J. Zhang, B. Tao, and J. Katz (1997), Turbulent flow measurement in a square duct with hybrid holographic PIV, Exp. Fluids 23, 373-381.

N. Zuckerman and N. Lior (2006), Jet Impingement Heat Transfer: Physics, Correlations, and Numerical Modeling, Advances in Heat Transfer 39, 565-631.

List of Publications

Journal Papers

G. Cardone, A. Ianiro, G. dello Ioio, A. Passaro (2011), Temperature Maps Measurements on 3D Surfaces with Infrared Thermography, Experiments in Fluids, DOI: 10.1007/s00348-011-1225-9.

R. Giordano, A. Ianiro, T. Astarita, G. M. Carlomagno (2011), Flow field and heat transfer on the base surface of a finite circular cylinder in crossflow, Applied Thermal Engineering, DOI: 10.1016/j.applthermaleng.2011.10.029.

A. Ianiro, G. Cardone (2011), Heat transfer rate and uniformity in multichannel swirling impinging jets, Applied Thermal Engineering, DOI: 10.1016/j.applthermaleng.2011.10.018, pp. 10.

A. Ianiro, G. Cardone (2010), Measurement of surface temperature and emissivity with stereo dual-wavelength IR thermography, Journal Of Modern Optics 57, 1708-1715.

Conference Proceedings

M. Novara, A. Ianiro, F. Scarano (2011), Adaptive interrogation for 3D-PIV, Proceedings 9TH International Symposium On Particle Image Velocimetry – PIV'11, Kobe, Japan, July 21-23, 2011.

D. Violato, A. Ianiro, G. Cardone, F. Scarano (2011), Investigation on Circular and Chevron Impinging Jets by IR Thermography and Time-Resolved Tomographic PIV, Proceedings ASME-JSME-KSME Joint Fluids Engineering Conference 2011 (AJK2011-FED), . Hamamatsu, Japan, July 24 - 29, 2011.

A. Ianiro, G. Cardone, G. M. Carlomagno (2010), Convective heat transfer in swirling impinging jets, Proceedings Fifth International Conference on Vortex Flow and Vortex Methods, San Leucio - (CE) Italy, 8-10 November 2010.

A. Ianiro, G. Cardone, G. M. Carlomagno (2010), IR wall heat transfer in swirling impinging jets, Proceedings 10th Quantitative Infrared Thermography Conference, Québec City, Canada, July 27-30th, 2010.

A. Ianiro, G. Cardone, M. Di Clemente, G. Rufolo (2010), Comparison between experimental IR measurements and numerical prediction in hypersonic flows,

Proceedings 10th Quantitative Infrared Thermography Conference, Québec City, Canada, July 27-30th, 2010.

A. Ianiro, G. Cardone (2010), Heat transfer measurements in swirling impinging jets, Proceedings ASME-ATI-UIT Conference on Thermal and Environmental Issues in Energy Systems, Sorrento Italy,May 16-19 2010.

A. Ianiro, T. Astarita, G. M. Carlomagno (2010), Heat transfer on the base surface of a finite circular cylinder in crossflow, Proceedings ASME-ATI-UIT Conference on Thermal and Environmental Issues in Energy Systems, Sorrento Italy, May 16-19 2010.

A. Ianiro, G. Cardone (2009), Measurement of Surface Temperature and Emissivity with Dual-Colour Stereo Thermography, Proceedings 10th International Workshop on Advanced Infrared Technology and Applications, Florence – Italy, September 8 - 11, 2009.

M. Di Clemente, G. Rufolo, A. Ianiro, G. Cardone (2009), Aerothermal Coupling Methodology for the Rebuilding of a Plasma Wind Tunnel Test and Comparison with an Advanced Infrared Measurement Technique, Proceeding 16th AIAA/DLR/DGLR International Space Planes and Hypersonic Systems and Technologies Conference, Bremen-Germany, October 19-22, 2009, Paper AIAA-2009-7236.

Acknowledgements

Ringrazio i miei tutor, il Prof. Carlomagno ed il Prof. Cardone, per avermi guidato e per avermi insegnato così tante cose. Mi sentirò sempre debitore verso il Prof. Cardone che mi ha insegnato a fare ricerca e il Prof. Carlomagno che ogni tanto ha provato a trasmettermi un po' della sua esperienza.

Mi ritengo molto fortunato perché, oltre che con i miei tutor, ho lavorato con altre due persone eccezionali, sempre disposte ad ascoltarmi e consigliarmi, il Prof. Astarita e il Prof. Scarano. Tommaso ha sempre sopportato, quasi tutti i giorni, (*credo con piacere*) la mia presenza invadente, le mie domande e le mie obiezioni; invece il Prof. Scarano mi ha ospitato nel suo laboratorio presso l'Università di Delft per due estati (e, a dire la verità, anche un autunno) di fila e lo ricorderò sempre con gratitudine.

L'esperienza in laboratorio non sarebbe stata la stessa senza le persone con cui ho condiviso la stanza e il lavoro ma anche le pause, i caffè e i pranzi. Un ringraziamento affettuoso va a Mario, Michele, Peppe, Sisina e Stefano, che sono stati miei vicini di scrivania o colleghi di laboratorio per periodi più o meno lunghi. I ragazzi che hanno fatto la tesi e sono passati per il laboratorio non sono stati meno importanti e alcuni di essi sono diventati dei cari amici; è stato bello lavorare insieme e li ricordo tutti con affetto.

Anche l'esperienza a Delft non sarebbe stata la stessa senza le persone che ho incontrato. Con Daniele e Matteo, il mio compagno di esperimenti e il mio compagno di scrivania, ho trascorso intere giornate, con le mani nell'acqua e con allegri sottofondi musicali, e poi anche tante belle serate. Poi c'erano gli altri ragazzi e i tecnici che pur non avendo lavorato con me direttamente sono sempre stati pronti a parlare, scambiare idee e consigli: Andrea, Artur, Eric, Frits, Kyle, Nico, *Peppino*, Peter, Sina, Vahid, Vanessa e Zhengzhong.

Acknowledgements

Un ringraziamento va a LaVision GmbH e al Prof. Piero Colonna per avermi prestato le telecamere CMOS usate negli esperimenti di PIV tomografica; il loro contributo è stato, evidentemente, essenziale.

Last but not least, ringrazio la mia famiglia e i miei amici. Tutto ciò non sarebbe stato possibile senza di loro e a loro è dedicata questa tesi.